Cover Page

Universiteit Leiden

Author: Wang, Ancong
Title: Automatic quantification of intravascular optical coherence tomography
Issue Date: 2014-11-13

Automatic Quantification of Intravascular Optical Coherence Tomography

Ancong Wang

2014

Automatic Quantification of Intravascular Optical Coherence Tomography

Proefschrift

ter verkrijging van

de graad van Doctor aan de Universiteit Leiden,

op gezag van Rector Magnificus prof. mr. C.J.J.M. Stolker,

volgens besluit van het College van Promoties

ter verdediging op donderdag 13 november 2014

klokke 11:15 uur

door

Ancong Wang

geboren te Shandong, China
in 1982

Contents

CHAPTER

1

Introduction and outline

1.1 Cardiovascular system

The cardiovascular system is a blood distribution network which consists of the heart, blood vessels, and blood. The heart is about the size of a closed fist and functions as the body's circulatory pump which takes in deoxygenated blood returned from the body and delivers it to the lungs to release carbon dioxide and absorb oxygen before pumping it into the artery network. On average, the heart beats 70 times per minute and even at rest, the heart can easily pump over 7 ton of blood throughout the body every day. Blood vessels transport blood from the heart to all body tissue and back again quickly and efficiently. There are three major types of blood vessels: the arteries, which carry blood away from the heart; the capillaries, where the actual exchange of gases, nutrients, and waste products between the blood and the tissues takes place; and the veins, which carry blood back to the heart. All vessels contain a hollow area called the lumen through which blood can flow and the lumen size corresponds with the amount of blood that can pass through it. Blood is composed of blood cells suspended in plasma. On average, an adult has about 5 liters of blood. The main function of blood is to deliver substances like nutrients, wastes, hormones and gases which not only help to maintain the body's homeostasis, but also play major roles in the body's defense against infection [1, 2].

1.2 Coronary circulation

The heart powers the whole cardiovascular system [3] while the blood transported to the myocardium is delivered by the coronary circulation in which the left and right coronary arteries branch off from the aorta and deliver oxygen-rich blood to the left and right sides of the heart. The deoxygenated blood from the heart muscle is returned to the vena cava by the coronary sinus. Figure 1 shows part of the cardiovascular system near the heart including the coronary circulation system. Only when healthy, these arteries are capable of autoregulation to maintain coronary blood flow at levels that appropriate to the heart muscle demands. Since the coronary circulation is the only source of blood supply to the myocardium and it contains little redundant blood supply, the ischemia caused by coronary vessel narrowing or blockage could be fatal [4].

1.3 Coronary artery disease

Coronary artery disease (CAD), which causes coronary heart disease (CHD), is the number one cause of death in the developed countries and a major cardiovascular disease in the rest of the world. Healthy arteries are elastic and smooth, but when CAD occurs, mixtures of cholesterol, inflammatory cells, lipoprotein and calcium, called plaques, start to deposit under the intima. The artery walls become thick and rigid while plaques release chemicals to promote the healing. In addition, plaques slowly build up and narrow the coronary arteries so that the blood flow to the myocardium becomes insufficient as Figure 2 presented. On the other hand, the ischemia can occur acutely as a sudden rupture of vulnerable plaques or thrombi can immediately reduce or even totally block the blood supply to heart or other organs. The traditional risk factors for CAD are high level of low-density lipoprotein (LDL) cholesterol, low level of high-density lipoprotein (HDL) cholesterol, high blood pressure, family history, diabetes, smoking, being older than 55 for women and being older than 45 for men.

High stress, lack of physical activity and obesity are also suspicious risk factors [5]. Without proper treatment, CAD will weaken the heart muscle and lead to arrhythmias, heart attack, heart failure and stroke.
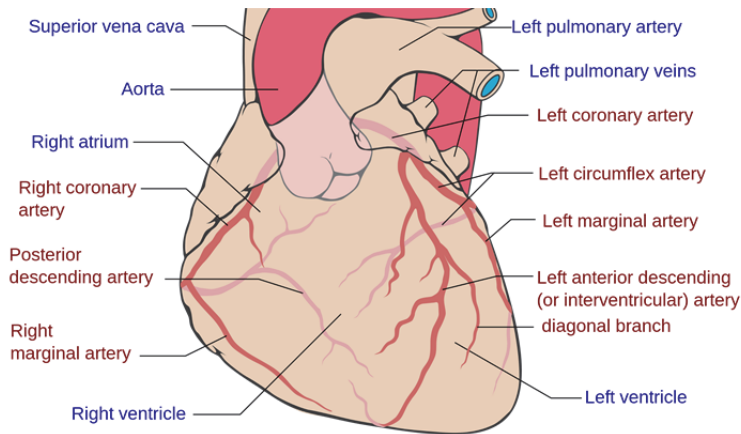
Figure 1-1. Part of the cardiovascular system near the heart including four heart chambers, main arteries and veins are labelled in blue text. On the heart, the coronary vessels are labelled in red text. (Source: http://en.Wikipedia.org/wiki/ File:Coronary_ arteries.png)
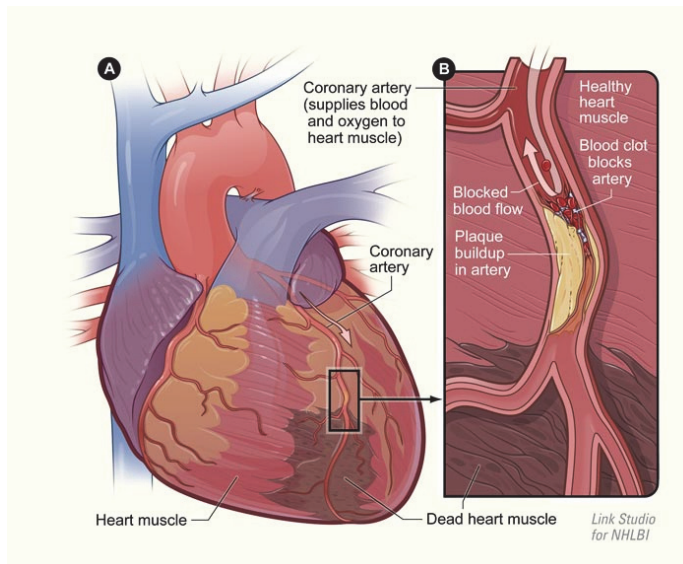
Figure 1-2. Coronary artery disease is caused by plaques build up in the coronary artery. Plaques can rupture and cause blood clots which block the supply of blood and oxygen to the heart. A blockage that is not treated properly will cause the affected heart muscle to die. (Source: http://www.nlm.nih.gov/medlineplus/ magazine/issues/ winter09/articles/winter09pg25-27.html)

1.4 CAD treatment

CAD cannot be fully cured, but in most of the cases, proper treatments are able to relieve the symptoms like chest pain and lower the risk of death. There are three main strategies of treatment: lifestyle changes, medications and medical interventions.

A healthy lifestyle including weight control, smoking cessation, physical exercise and healthy diet can be a preventive measure to delay or even prevent the atherosclerosis development which usually takes many years and could have no sign at all in the beginning. Patients with CAD can also benefit from the healthy lifestyle as it reduces the risk of further episodes and there is hope that CAD can be regressed before it causes serious CHD.

When lifestyle changes are insufficient, many different types of medications can be used to treat CAD. Antiplatelet drugs, such as aspirin, can keep platelets in the blood from sticking together. Anticoagulants are another class of drugs that prevent blood from clotting. Cholesterol-modifying drugs, like statins, decrease the level of LDL cholesterol which is one of the primary materials of plaques. Calcium channel blockers are used to decrease blood pressure, alter heart rate and alleviate chest pain. Beta blockers can reduce the oxygen request of myocardium by lowering the heart rate and blood pressure. On the other hand, Nitroglycerin can relax coronary arteries to increase the blood supply. Medications may help patients to delay or even avoid the demands of medical surgery. However, medications usually have side effects and are limited when facing severe CAD situations.

Medical interventions are required when lifestyle changes and medications do not work sufficiently. Coronary surgery and percutaneous coronary intervention (PCI) are the two primary means of revascularization. Coronary artery bypass graft (CABG) surgery was first introduced in 1960 and the idea is grafting healthy arteries or veins from other parts of the body to the narrowed coronary arteries. The grafted vessel bypasses atherosclerotic narrowing and creates a new path for blood flow to the heart muscle. CABG is particularly suitable for situations like the left main coronary artery blockage, multiple artery narrowings and poor heart function, but also has risks as any type of surgery.

PCI is a class of nonsurgical procedures that utilize coronary catheterization to open narrowed or even blocked coronary arteries, which serves as a chance for non-surgical candidates [6]. Coronary catheterization accesses the coronary circulation and blood filled chambers of the heart using a catheter for both diagnostic and interventional (treatment) purposes. During the catheterization, a guide wire is inserted into a big vessel in the arm or groin through a needle, and threaded to the heart under the guidance of a special x-ray imaging system. It helps doctor position catheters correctly. Next, the needle is replaced by a tapered tube called sheath. Through the sheath, a hollow guiding catheter is slid over the guide wire to the target region and then the guide wire can be removed. After the catheter reaches the right spot, diagnostic tests or treatments on the heart can be applied through it. For PCI treatment, a second guide wire is threaded through the guide catheter and passes the vessel blockage. It assists another catheter with a balloon on the end (balloon catheter) through the guide catheter to the narrowed region. Once in place, the balloon is inflated with a high pressure to push the plaque against the artery wall, relieving the blockage and restoring blood flow. Next, the balloon is deflated and withdrawn together with the catheter, guide wire and sheath. Unless the artery is too small, a

medical device called stent can be implanted during the PCI. A coronary stent is a tiny tube-like mesh that is used to support the narrowed vessel wall and keep the lumen open during the follow up. When implanting, a stent is constrained on a deflated balloon and delivered to the narrowed region during or after the balloon angioplasty. While the balloon is expanding, the stent is opened to support the vessel wall (Figure 3). In addition, there are also self-expanding stents. An introduction of stent is given in the next section. The advantages of PCI relative to CABG include less procedure time, ease of use, no general anesthesia, faster patient recovery and decreased systemic complications. Commonly, PCI is the first choice for stable as well as unstable CAD patients and it may delay or eliminate the future need for coronary artery bypass surgery [7-9].
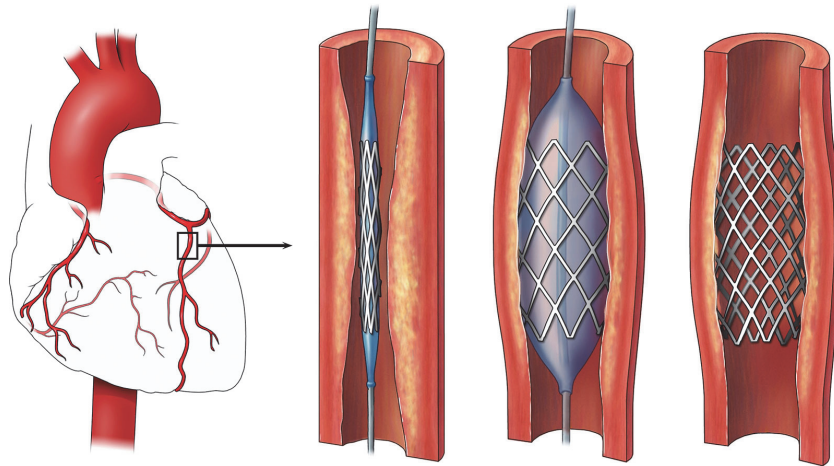
Figure 1-3. Stenting for coronary artery disease. First, the stent restricted on a deflated balloon is threaded to the narrowing of the vessel. The balloon is inflated to press plaques against the vessel wall and open the stent at the same time. The balloon is deflated and removed, leaving the stent to keep the lumen open. (Source: http://www.themedschoolproject.com/2012/02/valentines-day-special-way-to-mans. html)

1.5 Coronary stent

1.5.1 Bare metal stents

The PCI procedure, which was pioneered by Grüntzig in 1977, has become the most frequently performed therapeutic procedure in medicine [10]. The coronary balloon angioplasty was a breakthrough in treating CAD and quickly accepted worldwide. However, unpredictable risks of acute vessel closure caused by occlusive coronary dissection became evident. Sometimes, an emergency CABG surgery is required to save the patient. Besides, in up to one third of cases, too much tissue grows within the treated portion of the artery which re-narrows or even blocks the artery during the follow-up [11]. It is called late restenosis and mainly caused by constrictive remodeling [12, 13], elastic recoil [14] or the neointimal hyperplastic healing response [14, 15]. Although the luminal enlargement could be performed many times, it costs

more and does not eliminate the risks. These problems diminished the value of balloon angioplasty.

After a series of trial tests [16, 17], bare metal stents (BMS) were heralded as the second revolution in interventional cardiology to overcome the disadvantages of balloon angioplasty [11]. It provides a solution to acute vessel closure by moving intimal and medial flaps away from the lumen and maintaining radial support to prevent elastic recoil. The rate of sub-acute occlusion was successfully reduced to 1.5% so that emergency bypass surgery becomes a rare occurrence during the PCI. Furthermore, the late restenosis rate was significantly decreased by more than 10% [17]. By 1999, angioplasty paired with coronary stent implantation comprised 84.2% of all PCI procedures [18].

1.5.2 Drug-eluting stent

Despite the tremendous success in preventing the acute recoil and post-injury arterial shrinkage associated with balloon angioplasty, BMS still has a high restenosis rate of 22% during the follow up. As the implanted stents are foreign objects, they increase the risk of sub-acute thrombosis and late in-stent neointimal hyperplasia. The neointimal hyperplasia inside the stent was even more prominent than with balloon angioplasty, necessitating repeat treatment in numerous patients [19].

To reduce the in-stent neointimal hyperplasia, drug-eluting stents (DES) were invented. A drug-eluting stent consists of three components: a metallic stent as the platform, a polymer layer covering the stent as the carrier and some antiproliferative medicines as the agent. The medicines are slowly and continuously released into the artery to prevent it from becoming blocked again. Large trials have proved that the in-stent restenosis rate dropped greatly, but the increased risk of late stent malapposition and late stent thrombosis became evident [10].

1.5.3 Bioresorbable vascular scaffold

Metallic stents, including BMS and DES, are both permanent devices. As they caged the vessel, late luminal enlargement and advanced vascular remodeling could no longer occur. To solve their problems, the principle of temporary vascular scaffold, called bioresorbable vascular scaffold (BVS) was put forward (Figure 4). A BVS should provide a solid support to the vessel wall after the implantation to prevent acute vessel closure and recoil and persistently release antiproliferative medicines to prevent the restenosis. After restoring the artery, the scaffold will be fully degraded or resorbed during the follow-up. In the end, a BVS leaves no foreign object in the vessel but all future options open for the patient. Current trials showed that BVS has a better outcome in many fields than metallic stents [20, 21]. This nascent technology is evolving rapidly and more research and trials are ongoing for validation and improvement.
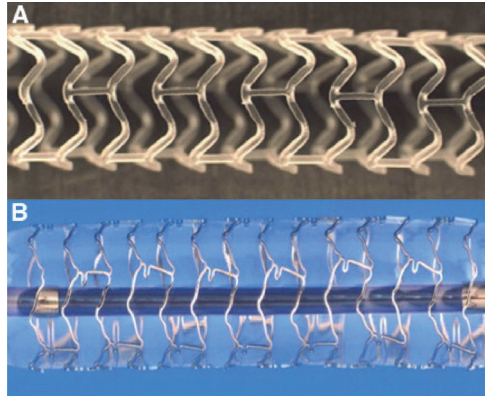
Figure 1-4. A comparison of a bioresorbable vascular scaffold (A) and a drug-eluting stent (B) (Source: http://interventions.onlinejacc.org/article.aspx?articleid= 1112042)

1.5.4 Stent design

Over the years, stent designs including pattern, material, coating and tissue-metal interface have been developed in addition to accompanying drug treatments. Although none of the current designs of coronary stents are ideal, constant research and improvement are being made especially with respect to homogeneous distribution of force, ease of placement, stability and conformability [22]. For example, the stent cell pattern affects the ability of vessel wall support. Small cells usually have better support but they can lower the side branch access through them.

1.6 Invasive imaging techniques

Symptoms of CAD, like chest pain, shortness of breath, palpitations and even fatigue, can be used for diagnosis. However, to diagnose and evaluate the CAD accurately, medical imaging techniques are necessary. For the past fifty years, sophisticated research of imaging the heart and vascular vessels has been studied enormously. Two main strategies of imaging techniques have been investigated: invasive imaging, such as coronary angiography, intravascular ultrasound (IVUS) and intravascular optical coherence tomography (IVOCT) and noninvasive imaging, such as computed tomography (CT), magnetic resonance imaging (MRI), x-ray and echocardiography. In the beginning, noninvasive methods were most preferred as they are safe and cheap. After the increased understanding of coronary artery diseases, the limitation of noninvasive methods became evident as they do not have sufficient resolution and penetration to give a detailed description of small structures, for example atherosclerosis, specifically vulnerable plaque with thin cap, the neointimal thickness and tissue coverage of struts. Nowadays, invasive imaging methods have become dominant for CAD diagnosis and treatment guidance.

1.6.1 Coronary angiography

Coronary angiography, since the 1960s, has been one of the most matured invasive imaging techniques for artery blockage diagnosis, evaluation and treatment. It is a modality that utilizes special x-ray and harmless dye (contrast) to show the insides of arteries. Similar as the PCI procedures, it is applied using the cardiac catheterization

procedure. Once the catheter is properly placed, the contrast will be injected through the catheter and released into the bloodstream. The mixture flows through the coronary arteries, making the lumen visible in the x-ray images. Due to the volume of the mixture, the vessel lumen size can be appreciated so that when a plaque has built-up inside an artery, a narrowed or restricted blood flow can be visualized. If the angiography reveals a blocked artery, a PCI procedure could be applied to restore blood flow instantly and the contrast will be injected again to assess the treatment outcome.

Coronary angiography is the traditional way of imaging during diagnostic and interventional coronary procedures as it can easily provide an accurate real-time illustration. The images can support accurate and highly reproducible measurements for clinical decision-making and research to estimate the regression and progression of coronary obstructions, particularly the lumen size, for the PCI outcome assessment [23]. However, coronary angiography loses accuracy in the presence of vessel superposition or foreshortening. Furthermore, only the lumen of the vessel is visualized by x-ray angiography, while the information about the vessel wall and plaque is absent. Therefore, it only has limited ability to characterize tissue and plaques beyond the detection of dissections and very advanced plaques with extensive calcification in the vessel wall. Thus, there are some scenarios in which complementary information is required besides the coronary angiography.

1.6.2 IVUS

IVUS imaging is a sound-based technique for visualizing arterial structure. A catheter with a high frequency ultrasound transducer mounted on the tip is threaded to the target vessel region by using cardiac catheterization. Because circulating blood is an excellent medium for transmission of ultrasound waves, the ultrasound transducer can emit a beam of ultrasound to the vessel tissue and receive the echo signal to acquire two-dimensional (2D) cross-sectional images of coronary arteries. The catheter is pulled back through the target region to generate real-time three-dimensional (3D) images and the images are recorded on the fast external storage for future analysis.

The frequency of ultrasound used in IVUS has a typical range of 20 - 40 MHz. The higher frequency of the signal results in the higher resolution of the images, but the lower penetration depth of tissue. Current IVUS imaging systems have a resolution of 100 – 250 µm. IVUS not only has the advantage of accurate determination of luminal dimensions of vessels, but also has the potential to assess the presence and extent of the atherosclerotic plaque and the characterization of arterial wall components. Compared with coronary angiography, IVUS does not cause radiation damage or require contrast injection. However, its common pullback speed is only 0.5 - 1 mm/sec, therefore, the IVUS imaging can be influenced by cardiac motion. Furthermore, the IVUS resolution still has limitations when measuring tiny structures like the vulnerable cap of a plaque.

1.6.3 IVOCT

IVOCT has emerged as an attractive new imaging modality, which offers superior resolution (approximately 10 µm) for in-vivo coronary plaque morphology. Figure 5(A) illustrates a commercial IVOCT system. Like IVUS, IVOCT uses an imaging catheter to acquire cross-sectional images of the target vessel, but instead of ultrasound, the

IVOCT imaging catheter emits near-infrared light beam to the vessel tissue. Due to the speed of light, interferometry techniques are necessary to measure the backscattered light since a direct quantification is not available. The reflected light from a point of the sample and the reference light generate an interference pattern so that a detector can create a pixel for this specific site based on the produced light and dark pattern. The imaging catheter is being rotated and pulled back by a motor when acquiring images and a fluid-filled semitransparent polymer tube, named protective sheath, is used to cover the imaging catheter. After scanning cross-sections successively at different transverse positions, a full 3D image of the vessel is generated. This procedure is usually assisted by a standard guide wire. Therefore, a typical IVOCT image always contains the imaging catheter, protective sheath, guide wire and vessel lumen. Besides these common components, there also could be stent struts, side branches, thrombi, plaques and other lesions. The major limitation of IVOCT is blood attenuation due to the backscattering properties of red blood cells, thus the blood is temporarily displaced from the field of view during imaging acquisition by infusing saline or contrast through the vessel. An example of a typical IVOCT image is given in Figure 5(B).

There are two IVOCT imaging systems: the time-domain IVOCT and the frequency-domain IVOCT [24]. The frequency-domain IVOCT imaging system facilitates high-speed pullbacks (20 mm/sec) during image acquisition without necessitating transient balloon occlusion of the coronary artery. The high pullback speed also greatly alleviates the impact of cardiac motion. However, some errors and artifacts still can be found in IVOCT images which may induce imprecise assessment and measurements. For example, the optic path length of the imaging catheter could be slightly different during the whole pullback run which results in different image scale as Figure 5(C) presented. Hence, an image calibration, called Z-offset correction, should be applied throughout the entire pullback to adjust the image scale. If the blood is not completely displaced, there will be residual blood in the lumen which blurs the boundary of the protective sheath and lumen like Figure 5(D). Residual blood artifacts also could be mistakenly labelled as thrombi. The small air bubbles inside the protective sheath can cause bright noise which will significantly attenuate the signal from behind and make poor definition of the protective sheath and imaging catheter. The seaming artifact is the result of rapid artery or imaging catheter shifting in a single frame, leading to misalignment of the lumen border. Figure 5(E) illustrated these two artifacts. In addition, when the imaging catheter passes a vessel tortuosity or simply sweeps during the pullback, its rotational speed could be nonuniform which conduces to nonuniform rotational distortion. It would lead to shape distortion or focal image loss [24-27]. There are also artifacts owing to the eccentric catheter position, such as sunflower artifact of metallic stent struts which appears as a bending of stent struts toward the imaging catheter. It means that a metallic strut parallel to the lumen wall could appear obliquely oriented to the lumen wall because when the light beam from the imaging catheter rotates over the strut, only the portion that is perpendicular to the light beam reflects light back. Thus, the strut orientation and apposition could be mistakenly assessed [28, 29]. An example is given in Figure 5(D). All these artifacts should be reduced in the next-generation IVOCT systems.
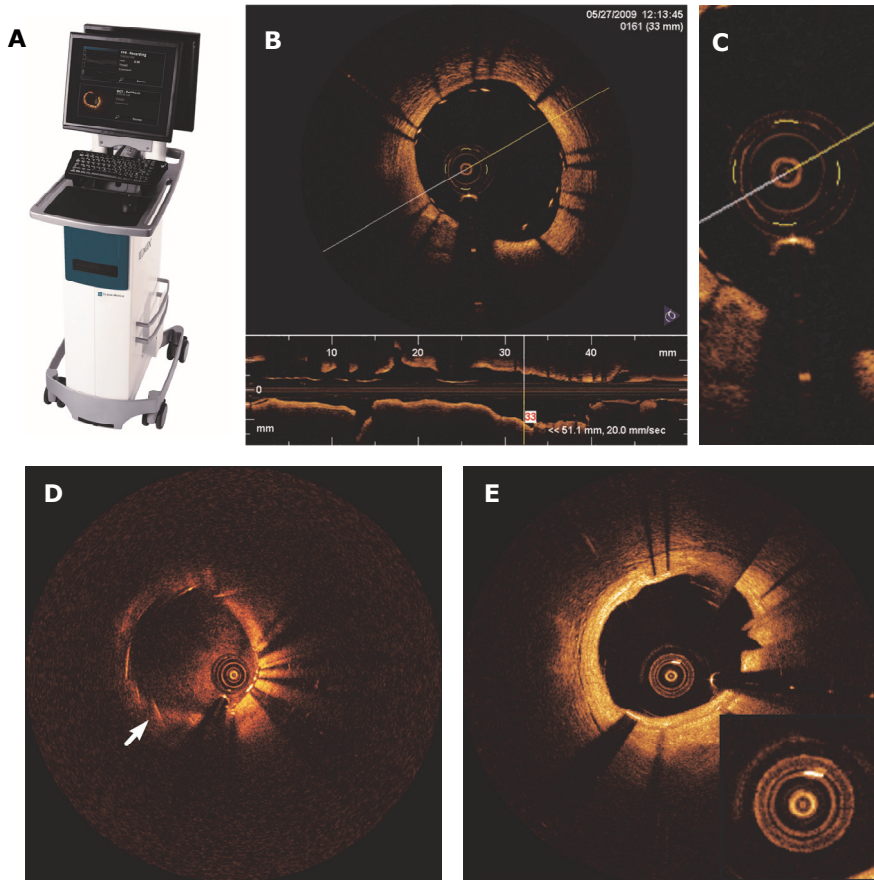
Figure 1-5. An IVOCT imaging system (St. Jude Medical, Westford, MA, USA) and an IVOCT image are presented in the figures (A) and (B). The top part of (B) is the cross-sectional image of vessel lumen which including the imaging catheter, protective sheath, guide wire, vessel lumen and metallic stent struts. The bottom section illustrates the longitudinal cut-up view of the whole scanned vessel region. The image center region is zoomed in in figure (C) which indicates the Z-offset correction failure as the 4 fiduciaries should align to fit the outer surface of the protective sheath. In figure (D), the residual blood results in bright noise inside the lumen and the eccentric imaging catheter causes the sunflower artifact of metallic stent struts (Arrow). An example of bubble noise in the protective sheath is given in figure (E) at 1 o'clock and the image behind it is blurred relative to other regions. At 2 o'clock, there is also a seaming artifact. (Source: http://professional-intl.sjm.com/products/vas/ intravascular-diagnostics-imaging/ffr-oct/c7-xr-oct-intravascular-imaging-system# overview)

Although not perfect, IVOCT is currently the only intravascular imaging technique having sufficient resolution to delineate the microscopic characteristics of fine structures, such as the thin fibrous cap thickness, thin neointimal hyperplasia and plaque type. Moreover, IVOCT can detect subtle structural changes after PCI procedures, such as plaque disruption including tissue prolapse and protrusion with

high sensitivity [30]. Due to the high frequency light source, IVOCT has a limited penetration ability of about 3 mm. However, within the limitation, IVOCT has better sensitivity and specificity for detecting calcification, lipid pool, fibrous cap, fibrosis, neointimal hyperplasia, intracoronary thrombus and thin cap plaque than IVUS [31]. IVOCT has been increasingly used for PCI guiding and evaluation [32].

1.7 Image processing challenges in IVOCT images

In recent years, IVOCT with both original 2D cross-sectional images and 3D reconstructions has been a powerful tool in the diagnosis and treatment of complex CAD. The demand for IVOCT-based applications is increasing, such as IVOCT-guided PCI, stent analysis and diagnostic assessment of coronary atherosclerosis including lipid necrotic core, thin fibrous cap, and inflammation region. Although enormous progress has been made since the invention of IVOCT, there are still increasing challenges in IVOCT image processing. The imaging catheter, guide wire, protective sheath and lumen are the common components in all typical IVOCT pullback runs and need to be segmented in many situations. For example, because the high intensity of imaging catheter affects the lumen segmentation, S. Tsantis, et al. detected the imaging catheter using Hough transform [33]. However, this method could be influenced by imaging catheter mirror artifacts [34] which appear as several concentric circles around the real imaging catheter. In order to measure in-stent neointimal hyperplasia, S. Gurmeric, et al. removed the imaging catheter by using a Gaussian filter and a morphological opening operation [35], which erases many details from the image and does not result in the position of imaging catheter. We also found that the imaging catheter can also mislead stent strut detection which is based on intensity analysis and it can be segmented by applying a min-filter over the whole pullback run in the z-direction [36]. However, this method is only applicable to Z-offset corrected pullback runs in which the imaging catheter is located in the same position. Appearing like a metallic stent strut, a guide wire could be mistakenly detected as a strut by many methods [36-39] and should be filtered out. Moreover, the guide wire and its shadow can obstruct the protective sheath and lumen contour detection, vessel wall analysis and 3D reconstructions [40, 41]. In the current commercial IVOCT systems, the protective sheath acts as a reference for optimal Z-offset determination within a pullback run because it has a fixed diameter [26]. This calibration of Z-offset is critical for accurate measures as 1% change in the magnitude of the ideal Z-offset can result in about 13% error in area measurements. Besides, small Z-offset errors can also amplify contour distortion, which may result in misinterpretation of the image [25]. However, the current calibration can fail due to the air bubble noise in the protective sheath, wrong manual adjustment and proximity of protective sheath to vessel wall. According to statistics, only 38% of the IVOCT images illustrated in peer-reviewed papers were calibrated correctly [34]. Lumen contour detection is one of most common image segmentation steps for such as region of interest definition, in-stent restenosis and lumen area measurement. The existing methods include Markov random field and wavelet transform analysis [33], fuzzy c-means clustering and wavelet transform [42] or deformable spline model [35]. However, in many cases, a light-weight and fast lumen contour estimation is more suitable for real-time applications.

IVOCT images have already been extensively used to guide, analyze and evaluate the stent implantation, which leads to optimized stent size, inflation pressure, deployment position and post-processing which thereby reduces the risk of restenosis

and thrombosis and increases the post-intervention minimal stent area. For example, an under-expanded stent cannot provide sufficient support to the vessel wall and thereby can result in late neointimal hyperplasia. Before covered by healing tissue, malapposed struts are also a main predisposing factor of acute in-stent thrombosis. Accurate strut position detection in the post-stenting IVOCT images can verify stent apposition to the vessel wall and provide additional information related to the presence of edge dissections, stent fracture, plaque protrusion, and the need for post-dilation or additional stenting. Detected struts also assist the 2D strut distribution analysis because nonuniform struts can influence the stenting treatment outcome. Fewer struts and a big maximum inter-strut angle contribute to in-stent restenosis, plaque rupture and thrombus [43-45]. The demands of 3D stent reconstruction have been rising as it is a more effective way to present the deployed stents and offers the possibilities for precise stent measurements, such as stent cell size and maximum circular unsupported area. Furthermore, 3D stent cell pattern can affect the spatial support to the vessel wall, bending flexibility and the dosing of antiproliferative medicines released from DES. Hence, both 2D and 3D information are necessary for stent design evaluation and optimization [46-49]. In addition, the strut area is of interest for the analysis of the bioresorption process of neoteric bioresorbable vascular scaffolds [50, 51].

Side branch detection is another important application as they are one of the most reliable landmarks for image registration and labeling. In both research and clinical practice, features in IVOCT pullback runs at different time-points may need to be compared, for instance, the valid lumen size or BVS strut area. IVOCT is also popular in image fusion with many other modalities like IVUS and near-infrared spectroscopy images, which would offer more tissue characterization information to increase our understanding of vessel morphology and aid the management of complex vascular pathology. Besides, the position and size of side branches in the lesion region should be taken into account for stenting and blood volume analysis as a stent in front of a side branch can cause thrombus formation and obstruct the blood flow to the side branch. With both 3D reconstructed stents and side branches, cardiologists can assess the side branch access through stent cells, which may help them to decide if the stent ostium in front of a side branch needs to be expanded [52-55].

1.8 Motivation and objectives

As mentioned above, IVOCT, as a novel imaging modality, has played an active role in a wide range of CAD applications, including research and clinical routine. Due to its unparalleled high resolution and the ability to delineate complex vascular structures [56], IVOCT technology makes many precise measurement and novel applications possible. However, currently, a lot of analyses in IVOCT images are still relying on the manual work which decreases their value. The goal of this thesis is to develop robust and accurate (semi)automated methods that can detect and segment the interesting components in IVOCT pullback runs, such as implanted stent struts and side branches in 3D for accurate measurement, so that the results could contribute to medical research as well as for clinical decision-making. As such, the specific objectives of this thesis are threefold:

1. To develop fast and reproducible approaches for the metallic stent strut and BVS strut detection in IVOCT pullback runs for quantitative analysis, 3D reconstruction and PCI improvement.

2. To precisely measure the stent cell size and side branch access through stent cells in 3D space by reconstruct stent cell contours and stent surfaces based on the detected struts, so that the stent influence to the vessel wall and side branches could be assessed.

3. To detect side branches in IVOCT pullback runs fully automatically based on precise segmentation of all the common components in typical IVOCT images for stenting optimization and image registration. The segmentation methods also can be used for other advanced image processing.

1.9 Thesis outline

The remainder of this thesis is organized as follows:

Chapter 2 presents a novel automated algorithm to detect metallic stent struts in IVOCT pullback runs [57]. This method detects the pixels that belong to a strut by analyzing the intensity profile of every scan line and clusters these pixels using the constraint of stent strut shadow regions. Guide wires are automatically removed. The detected struts can later be used for 3D stent reconstruction, coverage measurement, implantation validation and follow-up analysis.

Chapter 3 introduces an automatic method to detect the new BVS struts in IVOCT pullback runs [58]. The translucency BVS struts appear as black cores with bright boundaries which are very different from the metallic stent strut. Two different strategies were used for BVS strut detection in baseline and follow-up datasets, separately. In both situations, the black core areas are segmented and their centers are computed. The validation results suggest that this method can be a useful tool for BVS analysis and 3D visualization.

Chapter 4 studies the impact of an implanted stent to the vessel wall and side branches in the deployment region [52]. Stent cells are reconstructed in 3D space through simple user interactions in 2D space. Stent cell size is measured based on a precisely reconstructed 3D stent surface from detected struts. Moreover, a 2D approximation of the 3D stent cell surface is generated for maximum circular unsupported surface area measurement. In the end, stent covered side branches are segmented to combine with stent cells for side branch access measurement. The accuracy and robustness of this method were validated in both phantom and in-vivo IVOCT datasets.

Chapter 5 describes a fully automated side branch detection method which utilizes a precise segmentation pipeline for all the common components in typical IVOCT pullback runs including imaging catheter, guide wire, protective sheath and lumen [59]. The algorithmic results from segmentation pipeline and side branch detection method contain only a little error compared with the ground truth and, thereby suggest the new segmentation and detection methods could be used to improve our previous presented methods, guide stenting operation and register images.

Chapter 6 summarizes the main work described in different chapters of this thesis. This chapter also includes the future perspectives on the IVOCT imaging modality with respect to CAD diagnosis, treatment and research.

Chapter

1

1.10 References

1. "Cardiovascular system" (MedlinePlus, 21-01-2013, 2013), retrieved 03-03-2014, 2014, http://www.nlm.nih.gov/medlineplus/ency/anatomyvideos/000023.htm.

2. M. H. Ross and W. Pawlina, "Cardiovascular System," in Histology, 5 ed. (Lippincott Williams & Wilkins, 2006), p. 364.

3. W. Schaper, "Pathophysiology of coronary circulation," Prog Cardiovasc Dis 14, 275-296 (1971).

4. V. Fuster, R. Walsh, and R. Harrington, Hurst's the Heart, 13th Edition: Two Volume Set (McGraw-Hill Education, 2010).

5. S. M. Grundy, "Cholesterol and coronary heart disease. A new era," JAMA 256, 2849-2858 (1986).

6. I. M. Singh and D. R. Holmes, Jr., "Myocardial revascularization by percutaneous coronary intervention: past, present, and the future," Curr Probl Cardiol 36, 375-401 (2011).

7. W. S. Weintraub, J. A. Spertus, P. Kolm, D. J. Maron, Z. Zhang, C. Jurkovitz, W. Zhang, P. M. Hartigan, C. Lewis, E. Veledar, J. Bowen, S. B. Dunbar, C. Deaton, S. Kaufman, R. A. O'Rourke, R. Goeree, P. G. Barnett, K. K. Teo, W. E. Boden, C. T. R. Group, and G. B. Mancini, "Effect of PCI on quality of life in patients with stable coronary disease," N Engl J Med 359, 677-687 (2008).

8. G. N. Levine, E. R. Bates, J. C. Blankenship, S. R. Bailey, J. A. Bittl, B. Cercek, C. E. Chambers, S. G. Ellis, R. A. Guyton, S. M. Hollenberg, U. N. Khot, R. A. Lange, L. Mauri, R. Mehran, I. D. Moussa, D. Mukherjee, B. K. Nallamothu, H. H. Ting, F. American College of Cardiology, G. American Heart Association Task Force on Practice, A. Society for Cardiovascular, and Interventions, "2011 ACCF/AHA/SCAI Guideline for Percutaneous Coronary Intervention. A report of the American College of Cardiology Foundation/American Heart Association Task Force on Practice Guidelines and the Society for Cardiovascular Angiography and Interventions," J Am Coll Cardiol 58, e44-122 (2011).

9. M. R. Summers and M. R. Patel, "Appropriateness of percutaneous coronary intervention: a review," Curr Cardiol Rep 15, 379 (2013).

10. G. G. Stefanini and D. R. Holmes, Jr., "Drug-eluting coronary-artery stents," N Engl J Med 368, 254-265 (2013).

11. U. Sigwart, J. Puel, V. Mirkovitch, F. Joffre, and L. Kappenberger, "Intravascular stents to prevent occlusion and restenosis after transluminal angioplasty," N Engl J Med 316, 701-706 (1987).

12. T. Kimura, S. Kaburagi, T. Tamura, H. Yokoi, Y. Nakagawa, H. Yokoi, N. Hamasaki, H. Nosaka, M. Nobuyoshi, G. S. Mintz, J. J. Popma, and M. B. Leon, "Remodeling of human coronary arteries undergoing coronary angioplasty or atherectomy," Circulation 96, 475-483 (1997).

13. C. Di Mario, R. Gil, E. Camenzind, Y. Ozaki, C. von Birgelen, V. Umans, P. de Jaegere, P. J. de Feyter, J. R. Roelandt, and P. W. Serruys, "Quantitative assessment with intracoronary ultrasound of the mechanisms of restenosis after percutaneous transluminal coronary angioplasty and directional coronary atherectomy," Am J Cardiol 75, 772-777 (1995).

14. A. E. Rodriguez, O. Santaera, M. Larribau, M. Fernandez, R. Sarmiento, B. Perez, J. B. Newell, G. S. Roubin, and I. F. Palacios, "Coronary stenting decreases restenosis in lesions with early loss in luminal diameter 24 hours after successful PTCA," Circulation 91, 1397-1402 (1995).

15. K. N. Garratt, W. D. Edwards, U. P. Kaufmann, R. E. Vlietstra, and D. R. Holmes, Jr., "Differential histopathology of primary atherosclerotic and restenotic lesions in coronary arteries and saphenous vein bypass grafts: analysis of tissue obtained from 73 patients by directional atherectomy," J Am Coll Cardiol 17, 442-448 (1991).

16. D. L. Fischman, M. B. Leon, D. S. Baim, R. A. Schatz, M. P. Savage, I. Penn, K. Detre, L. Veltri, D. Ricci, M. Nobuyoshi, and et al., "A randomized comparison of coronary-stent placement and balloon angioplasty in the treatment of coronary artery disease. Stent Restenosis Study Investigators," N Engl J Med 331, 496-501 (1994).

17. P. W. Serruys, P. de Jaegere, F. Kiemeneij, C. Macaya, W. Rutsch, G. Heyndrickx, H. Emanuelsson, J. Marco, V. Legrand, P. Materne, and et al., "A comparison of balloon-expandable-stent implantation with balloon angioplasty in patients with coronary artery disease. Benestent Study Group," N Engl J Med 331, 489-495 (1994).

18. D. R. Holmes, Jr., M. Savage, J. M. LaBlanche, L. Grip, P. W. Serruys, P. Fitzgerald, D. Fischman, S. Goldberg, J. A. Brinker, A. M. Zeiher, L. M. Shapiro, J. Willerson, B. R. Davis, J. J. Ferguson, J. Popma, S. B. King, 3rd, A. M. Lincoff, J. E. Tcheng, R. Chan, J. R. Granett, and M. Poland, "Results of Prevention of REStenosis with Tranilast and its Outcomes (PRESTO) trial," Circulation 106, 1243-1250 (2002).

19. P. W. Serruys, M. J. Kutryk, and A. T. Ong, "Coronary-artery stents," N Engl J Med 354, 483-495 (2006).

20. Y. Onuma and P. W. Serruys, "Bioresorbable scaffold: the advent of a new era in percutaneous coronary and peripheral revascularization?," Circulation 123, 779-797 (2011).

21. 2D. Dudek, Y. Onuma, J. A. Ormiston, L. Thuesen, K. Miquel-Hebert, and P. W. Serruys, "Four-year clinical follow-up of the ABSORB everolimus-eluting bioresorbable vascular scaffold in patients with de novo coronary artery disease: the ABSORB trial," EuroIntervention 7, 1060-1061 (2012).

22. J. Tanigawa, P. Barlis, K. Dimopoulos, M. Dalby, P. Moore, and C. Di Mario, "The influence of strut thickness and cell design on immediate apposition of drug-eluting stents assessed by optical coherence tomography," Int J Cardiol 134, 180-188 (2009).

23. J. H. Reiber, "Introduction to QCA, IVUS and OCT in interventional cardiology," Int J Cardiovasc Imaging 27, 153-154 (2011).

Chapter

1

24. R. Hamdan, R. G. Gonzalez, S. Ghostine, and C. Caussin, "Optical coherence tomography: from physical principles to clinical applications," Arch Cardiovasc Dis 105, 529-534 (2012).

25. H. G. Bezerra, M. A. Costa, G. Guagliumi, A. M. Rollins, and D. I. Simon, "Intracoronary optical coherence tomography: a comprehensive review clinical and research applications," JACC Cardiovasc Interv 2, 1035-1046 (2009).

26. S. Tahara, H. G. Bezerra, M. Baibars, H. Kyono, W. Wang, S. Pokras, E. Mehanna, C. L. Petersen, and M. A. Costa, "In vitro validation of new Fourier-domain optical coherence tomography," EuroIntervention 6, 875-882 (2011).

27. F. Abtahian and I. K. Jang, "Optical coherence tomography: basics, current application and future potential," Curr Opin Pharmacol 12, 583-591 (2012).

28. S. Elahi, M. D. Feldman, J. Dijkstra, and T. E. Milner, "Intravascular optical coherence tomography measurement of size and apposition of metallic stents," Biomed Opt Express 4, 1876-1882 (2013).

29. S. Elahi, J. J. Mancuso, T. E. Milner, and M. D. Feldman, "Sunflower artifact in OCT," JACC Cardiovasc Imaging 4, 1220-1221 (2011).

30. K. Levitt, L. Vivas, B. Courtney, and K. A. Connelly, "Vascular imaging in diabetes," Curr Atheroscler Rep 16, 399 (2014).

31. A. V. Finn, Y. Chandrashekhar, and J. Narula, "IVUS and OCT: either or survivor," JACC Cardiovasc Imaging 4, 1047-1049 (2011).

32. T. Kubo, A. Tanaka, H. Kitabata, Y. Ino, T. Tanimoto, and T. Akasaka, "Application of optical coherence tomography in percutaneous coronary intervention," Circ J 76, 2076-2083 (2012).

33. S. Tsantis, G. C. Kagadis, K. Katsanos, D. Karnabatidis, G. Bourantas, and G. C. Nikiforidis, "Automatic vessel lumen segmentation and stent strut detection in intravascular optical coherence tomography," Med Phys 39, 503-513 (2012).

34. L. Hebsgaard, E. H. Christiansen, and N. R. Holm, "Calibration of intravascular optical coherence tomography as presented in peer reviewed publications," Int J Cardiol 171, 92-93 (2014).

35. S. Gurmeric, G. G. Isguder, S. Carlier, and G. Unal, "A new 3-D automated computational method to evaluate in-stent neointimal hyperplasia in in-vivo intravascular optical coherence tomography pullbacks," Med Image Comput Comput Assist Interv 12, 776-785 (2009).

36. A. Wang, J. Eggermont, N. Dekker, H. M. Garcia-Garcia, R. Pawar, J. H. C. Reiber, and J. Dijkstra, "A robust automated method to detect stent struts in 3D intravascular optical coherence tomographic image sequences," in Medical Imaging, 2012), 83150L-83150L-83159.

37. G. Unal, S. Gurmeric, and S. G. Carlier, "Stent implant follow-up in intravascular optical coherence tomography images," Int J Cardiovasc Imaging 26, 809-816 (2010).

38. G. J. Ughi, T. Adriaenssens, W. Desmet, and J. D'Hooge, "Fully automatic three-dimensional visualization of intravascular optical coherence tomography images: methods and feasibility in vivo," Biomed Opt Express 3, 3291-3303 (2012).

39. G. J. Ughi, T. Adriaenssens, K. Onsea, P. Kayaert, C. Dubois, P. Sinnaeve, M. Coosemans, W. Desmet, and J. D'Hooge, "Automatic segmentation of in-vivo intra-coronary optical coherence tomography images to assess stent strut apposition and coverage," Int J Cardiovasc Imaging 28, 229-241 (2012).

40. F. Nakao, T. Ueda, S. Nishimura, H. Uchinoumi, M. Kanemoto, N. Tanaka, and T. Fujii, "Guide wire shadow assessed by shading index is reduced in sparse spring coil wire in optical coherence tomography," Cardiovasc Interv Ther 28, 362-367 (2013).

41. A. Wang, J. Eggermont, J. H. C. Reiber, N. Dekker, P. J. H. de Koning, and J. Dijkstra, "Assessment of implanted stent coverage of side-branches in intravascular optical coherence tomographic images," in Medical Imaging, 2013), 86703J-86703J-86708.

42. K. Mandelias, S. Tsantis, D. Karnabatidis, P. Katsakiori, D. Mihailidis, G. Nikiforidis, and G. C. Kagadis, "Fast and Robust Algorithm Towards Vessel Lumen and Stent Strut Detection in Optical Coherence Tomography," Med.Phys. 39, 3645-3646 (2012).

43. H. Takebayashi, G. S. Mintz, S. G. Carlier, Y. Kobayashi, K. Fujii, T. Yasuda, R. A. Costa, I. Moussa, G. D. Dangas, R. Mehran, A. J. Lansky, E. Kreps, M. B. Collins, A. Colombo, G. W. Stone, M. B. Leon, and J. W. Moses, "Nonuniform strut distribution correlates with more neointimal hyperplasia after sirolimus-eluting stent implantation," Circulation 110, 3430-3434 (2004).

44. Y. Suzuki, F. Ikeno, and A. Yeung, "Drug-Eluting Stents strut distribution; A comparison of 3 stent designs by optical coherence tomography," Am J Cardiol 96, 182H-182H (2005).

45. M. P. Opolski, R. Pracon, G. S. Mintz, T. Okabe, J. Pregowski, S. Y. Lee, E. C. van der Waal, L. Kalinczuk, P. Roy, K. A. Smith, R. Torguson, Z. Xue, L. F. Satler, K. M. Kent, A. D. Pichard, R. Waksman, and N. J. Weissman, "Relation of drug-eluting stent strut distribution to stent thrombosis in coronary arteries," Am J Cardiol 104, 343-348 (2009).

46. Y. Suzuki, F. Ikeno, and A. C. Yeung, "Drug-eluting stent strut distribution: a comparison between Cypher and Taxus by optical coherence tomography," J Invasive Cardiol 18, 111-114 (2006).

47. S. Tanimoto, N. Bruining, D. Rotger, P. Radeva, J. M. Ligthart, R. T. van Domburg, and P. W. Serruys, "Late stent recoil of the bioabsorbable everolimus fluting coronary stent and its relationship with stent strut distribution and plaque morphology," Am J Cardiol 100, 145L-145L (2007).

48. M. P. Opolski, R. Pracon, G. S. Mintz, N. J. Weissman, L. Mandinov, J. Pregowski, M. Kruk, A. Witkowski, H. Wang, S. G. Ellis, E. Grube, K. D. Dawkins, and G. W. Stone, "Stent Strut Distribution at Implantation and 9-Month Follow-up in TAXUS and Bare Metal Stents and Its Effect on Neointimal Hyperplasia. An Intravascular Ultrasound Integrated Analysis of the Randomized TAXUS IV, V and VI Trials," Journal of the American College of Cardiology 53, A9-A9 (2009).

Chapter

1

49. A. Wang, J. Eggermont, N. Dekker, J. H. Reiber, and J. Dijkstra, "Semi-automatic Measurement of Vessel Wall Support from I mplanted Stents in I VOCT I mage Sequences," in MICCAI 2013 STENT, 2013),

50. J. L. Gutierrez-Chico, M. D. Radu, R. Diletti, A. Sheehy, M. B. Kossuth, J. P. Oberhauser, T. Glauser, J. Harrington, R. J. Rapoza, Y. Onuma, and P. W. Serruys, "Spatial distribution and temporal evolution of scattering centers by optical coherence tomography in the poly(L-lactide) backbone of a bioresorbable vascular scaffold," Circ J 76, 342-350 (2012).

51. A. Sheehy, J. L. Gutierrez-Chico, R. Diletti, J. P. Oberhauser, T. Glauser, J. Harrington, M. B. Kossuth, R. J. Rapoza, Y. Onuma, and P. W. Serruys, "In vivo characterisation of bioresorbable vascular scaffold strut interfaces using optical coherence tomography with Gaussian line spread function analysis," Eurointervention 7, 1227-1235 (2012).

52. A. Wang, J. Eggermont, N. Dekker, P. J. de Koning, J. H. Reiber, and J. Dijkstra, "3D assessment of stent cell size and side branch access in intravascular optical coherence tomographic pullback runs," Comput Med Imaging Graph 38, 113-122 (2014).

53. P. Mortier, M. De Beule, D. Van Loo, B. Verhegghe, and P. Verdonck, "Finite element analysis of side branch access during bifurcation stenting," Med Eng Phys 31, 434-440 (2009).

54. B. Hong, K. Z. Wang, Q. H. Huang, Y. Xu, X. G. Fang, Z. Li, and J. M. Liu, "Effects of metal coverage rate of flow diversion device on neointimal growth at side branch ostium and stented artery: an animal experiment in rabbit abdominal aorta," Neuroradiology 54, 849-855 (2012).

55. 55. F. Burzotta, M. De Vita, G. Sgueglia, D. Todaro, and C. Trani, "How to solve difficult side branch access?," Eurointervention 6, J72-J80 (2010).

56. 56. I. K. Jang, "Optical coherence tomography or intravascular ultrasound?," JACC Cardiovasc Interv 4, 492-494 (2011).

57. A. Wang, J. Eggermont, N. Dekker, H. M. Garcia-Garcia, R. Pawar, J. H. Reiber, and J. Dijkstra, "Automatic stent strut detection in intravascular optical coherence tomographic pullback runs," Int J Cardiovasc Imaging 29, 29-38 (2013).

58. A. Wang, S. Nakatani, J. Eggermont, Y. Onuma, H. M. Garcia-Garcia, P. W. Serruys, J. H. C. Reiber, and J. Dijkstra, "Automatic detection of bioresorbable vascular scaffold struts in intravascular optical coherence tomography pullback runs," Biomed Opt Express 5, 3589-3602 (2014).

59. A. Wang, J. Eggermont, J. H. C. Reiber, and J. Dijkstra, "Fully automated side branch detection in intravascular optical coherence tomography pullback runs," Biomed Opt Express 5, 3160-3173 (2014).

CHAPTER

2

Automatic metallic stent strut detection in intravascular optical coherence tomographic pullback runs

ABSTRACT

We developed and evaluated an automatic stent strut detection method in intravascular optical coherence tomography (IVOCT) pullback runs. Providing very high resolution images, IVOCT has been rapidly accepted as a coronary imaging modality for the optimization of the stenting procedure and its follow-up evaluation based on stent strut analysis. However, given the large number of struts visible in a pullback run, quantitative three-dimensional analysis is only feasible when the strut detection is performed automatically. The presented method first detects the candidate pixels using both a global intensity histogram and the intensity profile of each A-line. Gaussian smoothing is applied followed by specified Prewitt compass filters to detect the trailing shadow of each strut. Next, the candidate pixels are clustered using the shadow information. In the final step, several filters are applied to remove the false positives such as the guide wire. Our new method requires neither a-priori knowledge of the strut status nor the lumen/vessel contours. In total, 10 IVOCT pullback runs from a one-year follow-up study were used for validation purposes. 18311 struts were divided into three strut status categories (malapposition, apposition or covered) and classified based on the image quality (high, medium or low). The inter-observer agreement is 95%. The sensitivity was defined as the ratio of the number of true positives and the total number of struts in the expert defined result. The proposed approach demonstrated an average sensitivity of 94%. For malapposed, apposed and covered stent struts, the sensitivity of the method is respectively 91%, 93% and 94%, which shows the robustness towards different situations. The presented method can detect struts automatically regardless of the strut status or the image quality, and thus can be used for quantitative measurement, 3D reconstruction and visualization of the stents in IVOCT pullback runs.

2.1 Introduction

Heart disease is a leading cause of death in the developed countries and coronary artery disease (CAD) is the most common form [1]. In the treatment of CAD, stents are placed in the coronary arteries by means of the percutaneous coronary intervention (PCI) procedure. A stent is a tiny tube-like structure that is usually made of a wire mesh which is designed to be inserted into a vessel and functions as a scaffold device to keep the vessel open. The first generation of stents were bare metal stents, which have proven to be associated with an increased risk of coronary restenosis during the vessel wall healing process based on long term follow up studies [2, 3]. The second generation—drug eluting stents (DES) significantly decreased the occurrence of restenosis, but they are associated with late acquired stent malapposition which may lead to in-stent thrombosis [4]. Although newly implanted stents usually are located at the lumen boundary without tissue coverage (apposition) and later on nicely covered with a thin layer of tissue, still acute malapposition may occur or they may obstruct the blood flow to side-branches [5]. Therefore, detecting the stent strut position is highly important for stent placement evaluation and its follow-up analysis.

Intravascular ultrasound (IVUS) has been used for automatic stent strut detection, but its limited spatial resolution and low signal-to-noise ratio makes the detection difficult. To the best of our knowledge, no paper has been published for precise strut segmentation in IVUS pullback runs. As a relatively new optical signal acquisition technique, IVOCT imaging has a very high resolution (10-20 μm) which is about ten times higher than IVUS. IVOCT has been used as the exclusive technology for the precise in-vivo evaluation of strut coverage and vessel wall healing [6-8]. The acquisition is performed similar to IVUS; the imaging catheter acquires cross-sectional images of the coronary artery by emitting near infrared light instead of ultrasound towards the vessel wall in a radial manner while the transducer is rotating and the catheter is pulled back with a high and constant pullback speed. The superior sensitivity of the newly developed frequency-domain OCT systems is not only a key factor in achieving high image resolution, but also an important prerequisite for high speed imaging. It allows an acquisition speed of 100 – 160 frames per second and a very fast pull back speed (15–25 mm/second) which highly decreases the imaging time; on the other hand, it results into a large amount of images for each single procedure [9, 10]. Two IVOCT images in different coordinate systems are shown in Fig. 1.

Research is being carried out worldwide on IVOCT images, but an automated strut detection method that works robustly on routinely acquired clinical datasets remains a challenge. Many studies still depend on the manual strut detection. Two approaches [11-12] require the lumen and vessel wall contour to define the region of interest (ROI), and subsequently detect the newly implanted and covered struts in two different modes. For severely malapposed struts, they may be located outside the ROI and therefore cannot be detected. Another approach [13] detects the strut luminal surface in each A-line (scan-lines in the polar image) using flexible intensity thresholds. A-priori knowledge of the strut status (apposed or covered) is needed for stent strut detection. The type of the implanted device is also required for apposition assessment. The catheter artifacts and guide wire are masked with a fixed region and the guide wires beyond the mask region are manually detected and removed, which may be time-consuming.

Chapter

2

Separating modes for different strut status: "malapposition", "apposition" and "covered" usually can improve the detection accuracy, but a pullback run or even a single image may contain struts with different status. In this paper, we present a robust algorithm to process an entire IVOCT pullback run, which requires neither a-priori status information, nor lumen or vessel wall contours.
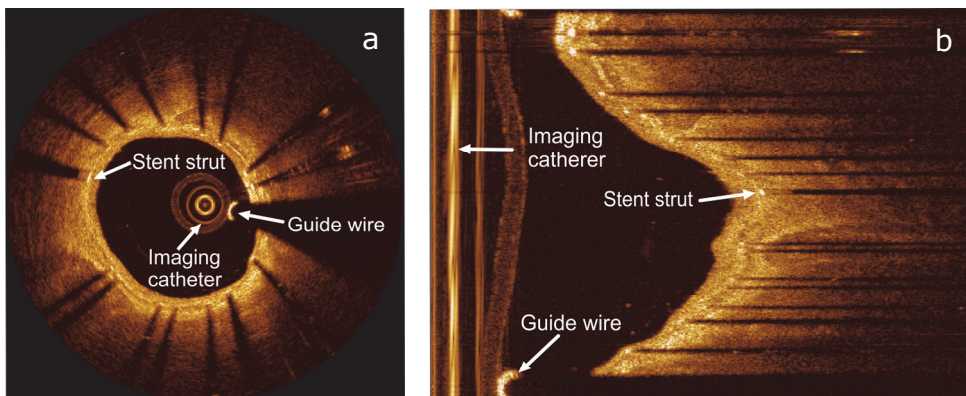
Figure 2-1. Examples of IVOCT images in (a) Cartesian coordinate system and in (b) polar coordinate system respectively. In both images, a stent strut, the guide wire and the imaging catheter are annotated.

2.2 Materials

The During this research, all of our IVOCT pullback runs were acquired using a C7-XR FD-OCT intravascular imaging system with a C7 Dragonfly™ Intravascular Imaging catheter (LightLab Imaging, Inc., Westford, MA, USA). The intravascular imaging catheter works together with a 6F guiding catheter. The automated pullback speed is 20 mm/s with a data frame rate of 100 frames per second. During the acquisition, a standard 0.014 inch steerable guide wire may be used. Temporary blood flushing was performed with a contrast infusion.

We use the 16-bit raw image data in polar coordinate system instead of the commonly used 8-bit Cartesian image representation [12], because it contains all of the original information and some details might get lost during the conversion from polar to Cartesian. Each polar frame has the same size of 960×504 pixels.

Although all the pullback runs were acquired with the same IVOCT system, they differ significantly in image quality. There are multiple reasons for that: for example, the noise can be caused by the residual blood after the infusion or by tiny air bubbles [7]. Moreover, the limited penetration depth, imaging catheter position, cardiac motion, redundant echo and many other factors can also affect the image quality.

2.3 Method

2.3.1 General approach for stent strut detection

The automatic strut detection method was developed using the MeVisLab toolbox (MeVis Medical Solutions AG, Bremen, Germany) together with in-house developed

C++ modules. As the flow chart in Fig. 2 shows, our detection method consists of five steps: first, the pullback runs are preprocessed to de-noise and define the proper ROI. Next, the strut candidate pixels are detected by locating the front edges of the struts in IVOCT images. In order to remove false candidate pixels and to cluster the remaining pixels into discrete struts, the shadow edges are detected. Finally after clustering, the guide wire and some false positives are removed using 3D information of the whole pullback run. In the following sections, each of the subsequent steps for the strut detection in IVOCT is described in further detail.
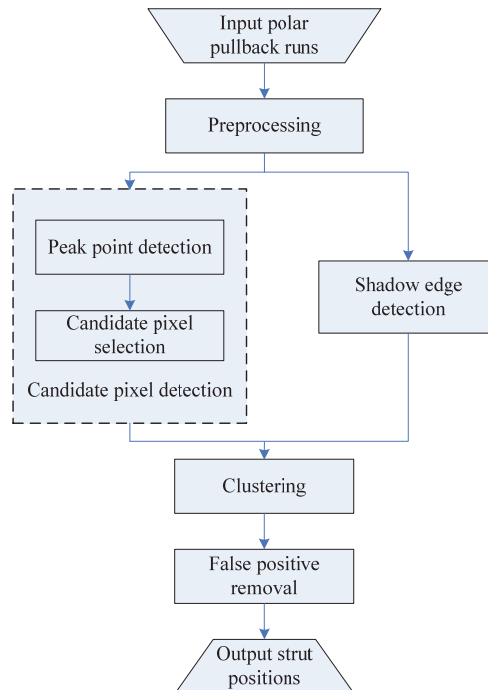
Figure 2-2. Flow chart of the strut detection algorithm processing steps.

2.3.2 Preprocessing

The preprocessing starts with noise reduction in the IVOCT pullback run since it hampers the strut detection. The main part of the noise has a relatively low intensity value. According to Ughi et al. [13], the lowest 5% intensity values of the histogram can be considered as noise. In a similar fashion, we determine the histogram of the whole pullback run and set all pixels below this threshold value to 0.

The preprocessing continues with the definition of the Region of Interest (ROI). In order to detect also the malapposed struts, we need to select a bigger ROI than the region between lumen contour and vessel wall contour. However in the lumen area, the imaging catheter may generate very bright artifacts which have similar intensity values as stent struts. The ROI should exclude these artifacts.

The catheter artifact appears like rings in the center of the image as Fig.1 (a) shows. After a proper z-offset correction, they are constant in all frames of a single pullback

run [14]. In the polar data, these artifacts are shown as parallel vertical lines at the left side of the images and they may affect the strut detection. To exclude these artifacts, a minimum filter in z-direction and a vertical line detection method [15] are applied to each IVOCT pullback run. The region to the right of these continuous straight vertical lines determines the ROI for our detection method.
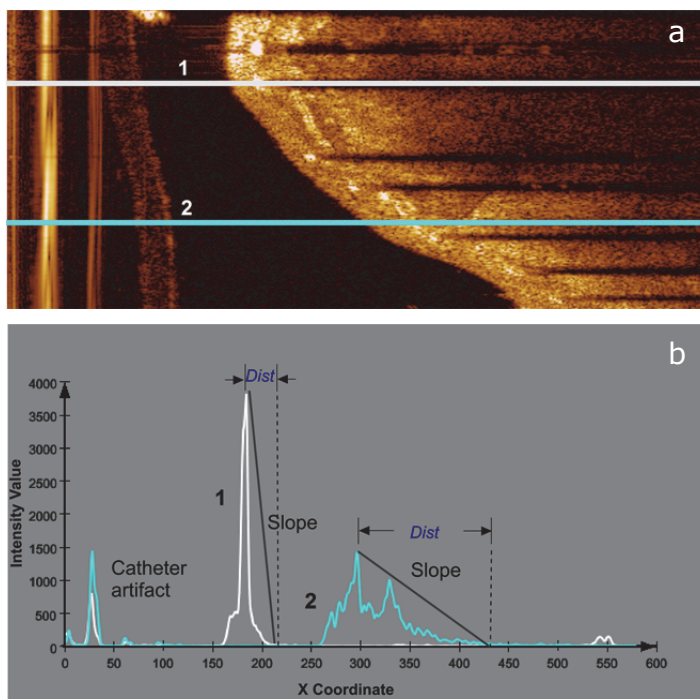
Figure 2-3. Examples of intensity profiles in polar images. The A-line (1) in Fig 3a crosses a stent strut and its corresponding intensity profile in Fig 3b has a higher peak point and a sharp fall to the shadow area, compared to the A-line (2) in Fig3a, which passes purely through tissue and its corresponding intensity profile in Fig 3b has a longer distance between the peak point and the shadow area. "*Dist*" indicates the distance between the peak point and the start point of the trailing shadow.

2.3.3 Candidate pixel detection

In IVOCT images, a metal stent strut appears normally as a bright spot with a trailing shadow behind it, since the strut reflects most of the light, while normal vessel tissue scatters and attenuates the light. Therefore, a strut has higher intensity values than the surrounding tissue. The pixels having the maximum intensity value in each A-line are candidates, under the assumption that there is only one strut per A-line. This also means that currently we exclude overlapping stents. Fig. 3 shows two examples of the intensity profile.

In general, one cannot state that the struts always have the highest intensity values in an entire pullback run. For that reason, a global intensity threshold is not applicable, and we have decided to use the slope of the intensity profile. By detecting the maximum intensity and the distance between this peak point and the first pixel of

the potential shadow area, the slope is calculated. The potential shadow area is defined by a window of 30 continuous low intensity pixels. The maximum intensity value of the potential shadow region was set as the 89th percentile of the intensity histogram of the ROI in the entire pullback run. The slope reflects the local intensity change, and strut pixels usually are associated with a steeper slope than tissue pixels. An example of the candidate pixel results is shown in Fig. 4 (b). Because the distance from struts to their trailing shadows are similar, we determine the slope threshold based on the histogram as well.

Chapter

2
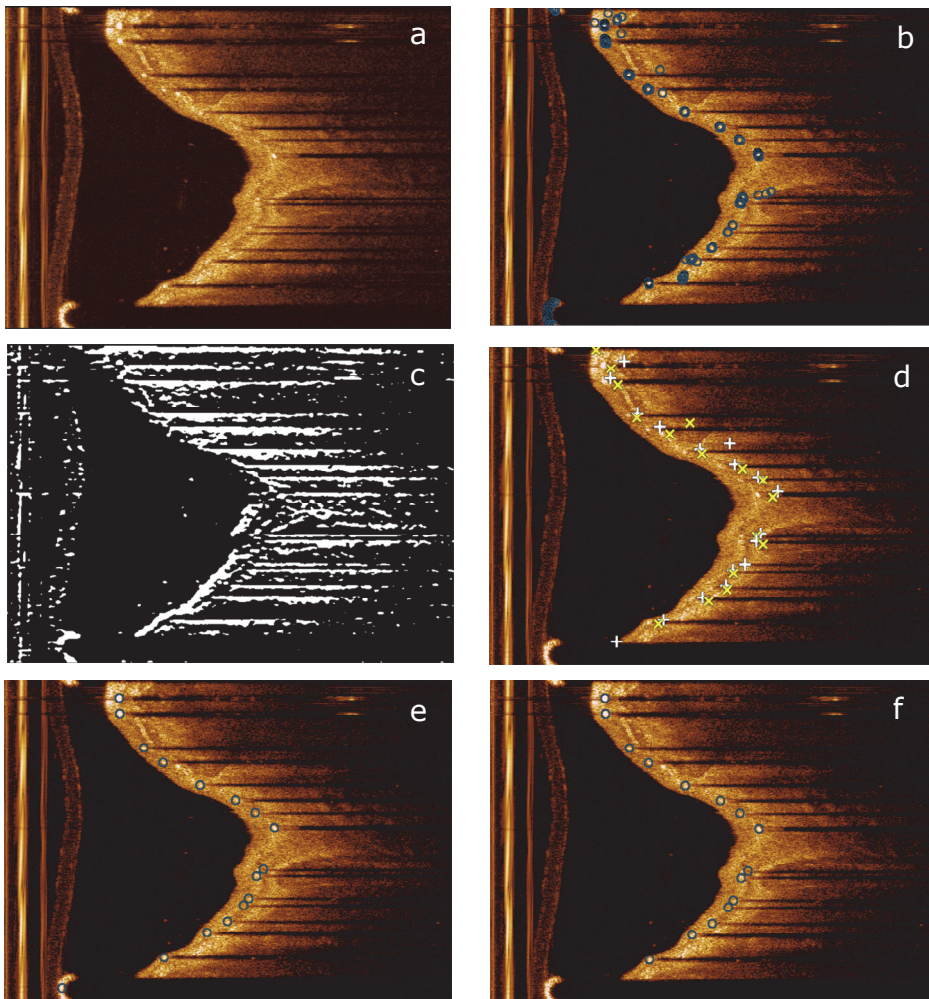
Figure 2-4. Results of each step in the shadow edge detection. (a) shows the original image. (b) shows the results of the candidate pixel detection including false positives. Peak points are indicated as 'o'. (c) shows the result after Prewitt compass edge detection for only bottom edges. In (d), the top edges are indicated by '+' and the bottom edges by '×'. (e) shows the clustering results which are indicated by 'o'. In (f) the final results after guide wire removal are presented with the struts indicated by 'o'.

2.3.4 Shadow edge detection

To cope with artifacts such as the sunflower artifact [14], the position of a stent strut is defined by the middle point of its front edge. It reflects the start position of a strut, which can be used for the quantitative analysis of strut and the 3D stent reconstruction.

The middle point is calculated by the average position of a group of candidate pixels. However, it is difficult to cluster the candidate pixels into individual struts directly, because both the width of the struts and the gap between two neighboring struts can vary significantly. We also need to remove the false candidate pixels most of which are located in the tissue area outside the struts regions as Fig. 4(b) shows. In order to solve these issues, the width and the location of each strut are needed. Additional information is gathered by using the trailing shadows behind the struts. As the trailing shadows align with the imaging catheter, they are almost horizontal in the polar image, and their width and location are approximations of the corresponding strut width and location. The top and the bottom edge of a shadow define the clustering region for the strut.

A Gaussian filter is applied to smooth the images before the shadow edge detection. Next, a Prewitt compass operator with two special kernels is applied to detect the top and bottom edges separately [16]: one kernel is only sensitive to the horizontal bright to dark edges (top edges); while the other kernel is only sensitive to the horizontal dark to bright edges (bottom edges). An example of the bottom edges is shown in Fig. 4(c). Only edges above a certain length were accepted, to avoid the short false shadow edges such as those associated with an eccentric lumen boundary.

2.3.5 Clustering

The detected edges divide the polar images into consecutive intervals, which define the location and width of the struts. We cluster the candidate pixels in each interval. Special attention is paid to edges at the top and bottom of the polar images, since they actually could belong to each other, but have been split into two halves due to the nature of the polar image. At the start of the clustering, each candidate pixel is a cluster [17]. Clusters merge if the minimal distance between them is shorter than a threshold, in our case determined experimentally at a 4 pixel distance. This procedure continues until no more clusters can merge.

In some cases, only one edge of the shadow can be detected, because the other edge is too short or too blurred, especially when a strut is located far away from the imaging catheter. At the same time, false edges may be included if there is e.g. a seaming artifact [12] or highly eccentric lumen boundary. An example of the seaming artifact is shown in Fig. 6(c). To avoid the false clusters caused by these influences, we need to select the correct candidate struts from the clusters. Because the strut is right below its top edge and above its bottom edge, for each top edge, the first cluster below it will be selected. Similarly, for each detected bottom edge, the first cluster above it will be selected. All the other clusters are removed. The average position of the candidate pixels of the same cluster determines the corresponding strut position.

In cases where the struts are located far away from the imaging catheter or covered with a thick layer of hyperplasia, a strut may have a low intensity value comparable to the surrounding tissue, and the described candidate pixel detection may fail. If there is no candidate strut between a pair of top and bottom edges, we check if there is a non-

bright strut. We first assign a search range based on the start points of the shadow edges. In this search range, the pixel with the highest intensity value of each A-line in the shadow region is detected. All the pixels with an intensity value higher than the maximum shadow intensity threshold will be clustered as a non-bright strut.
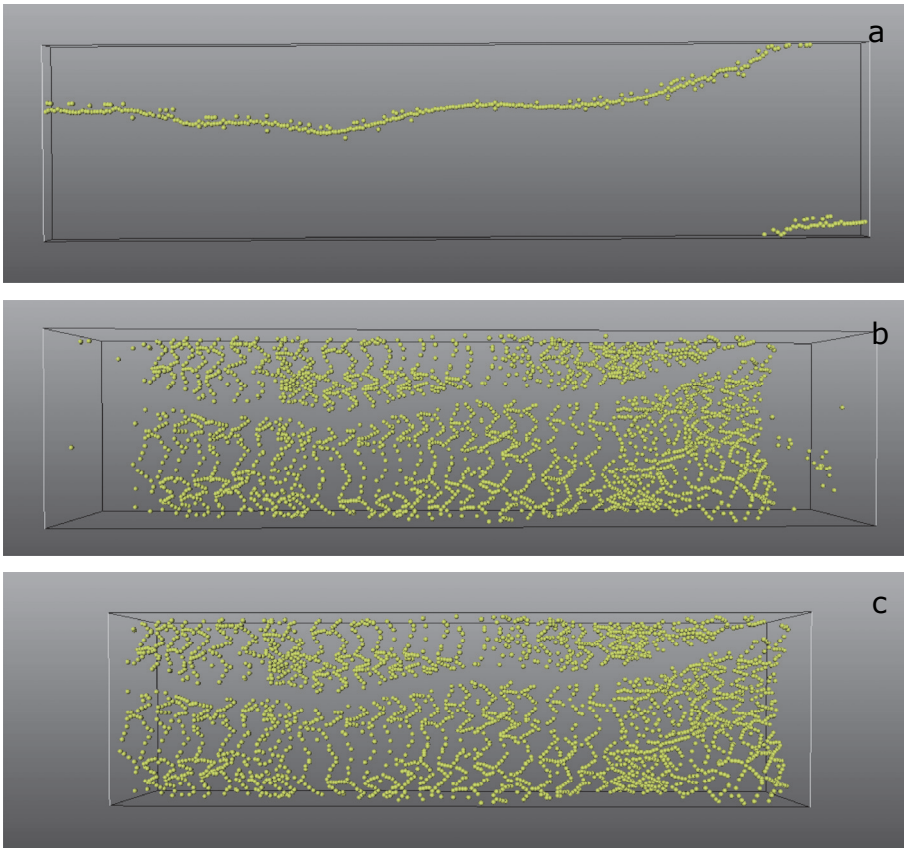
Figure 2-5. (a) shows the detected guide wire from the whole pullback run. In some frames, there is more than one guide wire because of the artifacts; (b) shows the strut results after the guide wire removal. In the beginning and the ending segments of this pullback run, no real stent exists; (c) shows the result after stented segment detection.

2.3.6 False positive removal

If a guide wire is present during the image acquisition, it also reflects most of the energy and causes a trailing shadow behind it. It will be improperly recognized as a strut by our method. Compared with the real struts, a guide wire is usually located closer to the imaging catheter and its coordinates are continuous throughout the whole pullback run. Therefore, we have defined a guide wire distance threshold to measure the guide wire continuity. By using this spatial feature, a guide wire filter was developed, which searches a series of continuous candidate struts which are located closer to the imaging catheter than any other. Fig. 4(f) shows the strut detection result

after the guide wire removal. If no guide wire is used, the filter will not remove any candidate struts. Fig. 5 shows the result for the guide wire removal.

In Fig. 5(b), it is clearly demonstrated that there are only a few strut candidates in the proximal and distal part of the pullback run. The reason is that the pullback usually is much longer than the stent length. By analyzing the amount of struts detected in each frame of the pullback run, we can identify the stented segment automatically and remove all the strut candidates outside this segment. An example result is shown in Fig. 5(c).

2.4 Validation

To evaluate our automatic detection algorithm, we used 10 pullback runs of stented coronary segments of 7 retrospectively selected patients from a one-year follow-up study. Eight of our polar IVOCT pullback runs have 271 frames each, and the other two pullback runs both have 541 frames.

We applied our approach to all 10 pullback runs which in total contain 3250 frames. One observer (*A)* indicated the start point of the struts in all the images to compare them to the automated results for validation. In three pullback runs, there are a total of 19 frames that were not marked because of the very low image quality. We did not take these frames into account for our validation. In a total of 3231 frames, 18311 struts were marked manually.
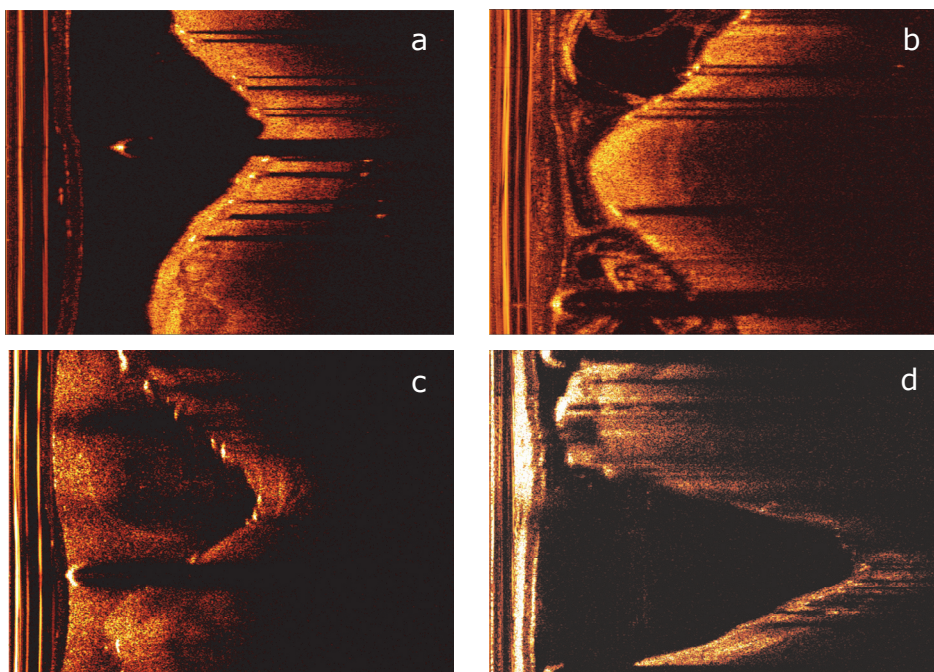
Figure 2-6. Examples of the three image quality groups. (a) and (b) show a good quality image and a medium quality image respectively. (c) and (d) are two low quality images; (c) has blurred shadows and a seaming artifact, while (d) shows some struts having only clear shadow without bright spot.

To determine how accurate a human observer can find and indicate exactly the same location for the same strut, a second independent observer (*B*) analyzed a subset of 179 images from 8 of the 10 pullbacks. On this subset observer *A* indicated 2033 struts, while observer *B* indicated 1864 struts, resulting in 1841 corresponding struts. Expert observer *A* also categorized all the IVOCT pullback runs into three groups based on the image quality: high, medium and low. This selection was based on the amount of noise in the images, and the experienced difficulty during the manual definition of the strut positions. In this paper, 4 pullback runs were assigned to the high quality group, 3 pullback runs to the medium quality group and the remaining 3 pullback runs to the low quality group. Each strut was also assigned to one of three categories based on the strut status: malapposition, apposition and covered. The malapposition group contains all the malapposed struts and the struts over the side-branches. The apposition group includes uncovered struts and the struts with minimum neointimal hyperplasia. There are 681 struts in the malapposition group, 5382 for the apposition group and 12248 for the covered group, respectively.

To examine the robustness of our method, we compared the results from our method with the manual results from observer A for different combinations of image quality and strut status. We also tested each main parameter for three values, the recommended value and +/- 20% of the recommended value to investigate the sensitivity of the algorithm. In Table 3, the performance and the distance error are presented to quantify the effect of these parameter variations.

2.5 Results

The inter-observer agreement is defined as the number of agreements divided by the average number from two observers and the agreement was found to be 95%. The mean and standard deviation of the distance between these corresponding struts were found to be 2.9 ± 3.3 pixels. According to our experts, a 10-pixels distance (about 0.05 mm) is an acceptable distance when comparing the algorithmic results to the expert results of observer A. Within this acceptable distance, the mean and standard deviation of the distance error is 1.7 ± 1.1 pixels. Table 3 shows the distance error between two manual results and the distance error between the manual results of expert A and the automated results.

The sensitivity of the detection method is defined as the ratio between the number of struts correctly detected by our algorithm and the number of struts found by expert observer A. In Table 1, the average sensitivity of our automated approach for the different categories is given in percentages. The false positives (FPs) show the ratio of the number of false positives in the automatic results compared to the number of struts as defined by observer A. Next, the subtotals of the algorithm performance for different image qualities or different strut status categories are also given in Table 1.

In all groups, our method shows a good agreement with the expert results. For high, medium and low quality IVOCT images, the new method found 96%, 92% and 89% of the stent struts, respectively. For apposition, malapposition and covered status, 91%, 93% and 94% of the struts were found, respectively. The average sensitivity is 94%. All combinations contain only a few false positives (4%).

Table 1. The sensitivity of the new algorithm for all combinations of the image quality and strut status. The numbers indicate the sensitivity of the algorithm in percentages. FPs means the percentage of false positive detected struts compared to the manual results

Image status quality \ Strut	Malapposed (%)	Apposed (%)	Covered (%)	Subtotal (%)	FPs (%)
High	92	98	96	96	4
Medium	87	93	92	92	4
Low	92	88	89	89	6
Subtotal	91	93	94	94	4

According to our validation, the algorithm works best for apposed struts in high quality images, since they usually appear as very clear bright spots and have nice trailing shadows. Malapposed struts may have short or blurred shadows which cause difficulties in the detection. Generally, in our low quality data set, malapposed struts are brighter than other struts. The most difficult situations are the apposed and covered struts in low quality images. Compared to the other struts, they usually have a less bright appearance and blurred shadows because of the noise or the thick coverage which causes more absorption and scattering of light. Their trailing shadows appear fuzzier and shorter compared to the other situations. Our algorithm is relatively robust in case of different image quality, but low image quality is still the main reason for false positives and false negatives. In case of severe restenosis, a strut is not visible anymore except for a weak trailing shadow. Even experts have difficulty to mark these correctly. It is also not always clear how to separate a cluster due to the structure of the stent. All these factors may affect the result of the proposed algorithm.

Eight of the pullback runs were acquired with a guide wire, while the remaining two had no guide wire. Our guide wire filter successfully detected the pullback runs that contain guide wires, and filtered all the guide wires from them. For the other two pullback runs that contain not guide wire, the filter did not remove any strut candidates.

For processing, we used a Windows XP Professional x64 Edition Version 2003 with SP2 computer with 2.0 GHz CPU and 4 GB memory. Generally, it takes less than 5 minutes to process a pullback run containing 271 frames with MeVisLab 2.1. We also implemented a pure C++ version of this method, which decreases the computing time to less than 2 minutes.

2.6 Discussion

Automatic stent strut detection is important as it can simplify and speed up quantitative stent strut analysis and 3D stent reconstruction. We present a 3D detection method for stent struts in IVOCT pullback runs, which is based on the intensity features and shadow edge detection. It is also important to note that spatial information is used to remove the guide wire and the false struts in the empty frames. Because only in an IVOCT pullback run which contains a guide wire, a continuous list of strut candidates through the whole pullback run can be found. With a good

performance in all situations, our method can detect stent struts robustly and independent of strut status or image quality. The validation study showed that the new method successfully detected 94% of the 18311 struts from 10 pullback runs. Compared to former research, our method requires no lumen contour or vessel wall segmentation and it is relatively insensitive to the image quality. Moreover, the new method does not require different modes for different strut status, so that no a-priori information or user input is needed. Additionally, we presented a novel guide wire filter to classify and remove guide wire automatically.

2.6.1 Parameter selection and sensitivity analysis

The whole method contains more than 10 parameters. Some parameters are related to the size of the input image, while some other parameters are fixed based on the histogram of the input image, for example, the maximal intensity threshold for trailing shadow and the slope threshold for candidate pixels detection. The most important parameters for our method are presented in Table 2. We used the same parameter rule for all the pullback runs.

Table 2. The major parameters used in this method

Parameter	Value
Max shadow intensity threshold	89th percentile of the histogram
Sliding shadow size	30 pixels
Slope threshold	-48
Shadow edge length threshold	100 pixels
Clustering distance threshold	4 pixels
Guide wire distance threshold	40 pixels

To evaluate our method when the parameters are changed, we varied the main parameters by ±20%. We also computed the mean distance error between the algorithmic results and the manual results from observer A and its standard deviation. The distance error is calculated only between the successfully detected struts. The performance and the distance error are shown in Table 3 and demonstrate that even if the parameters are changed by 40% (±20%); the position of the struts that are detected by our algorithm does not change much.

Table 3. The correlation and the distance between the manual result from observer *A* and the algorithmic results with standard parameters and after the parameters are changed by ±20%. The distance error and its standard deviation are measured in pixel size

Parameter	Performance TP [FP]* (%)			Distance Error (pixel)		
Change	0%	-20%	+20%	0%	-20%	+20%
Max shadow intensity threshold	94 [4]	91 [5]	94 [7]	1.7 ±1.1	1.8±1.3	1.8±1.3
Sliding shadow size	94 [4]	92 [5]	93 [5]	1.7 ±1.1	1.7±1.2	1.7±1.2
Slope threshold	94 [4]	93 [7]	92 [5]	1.7 ±1.1	1.8±1.3	1.8±1.2
Shadow edge length threshold	94 [4]	85 [12]	88 [5]	1.7 ±1.1	1.8±1.3	1.8±1.3
Clustering distance threshold	94 [4]	94 [6]	93 [4]	1.7 ±1.1	1.8±1.2	1.7±1.2

* Performance TP value means the sensitivity our method. FP value in [ ] shows the percentage of false positive detected struts compared to the manual results

2.6.2 Limitations

The presented method can cluster the strut even if only one shadow edge was detected. However, for severe in-stent restenosis, some struts are covered by such a thick layer of new tissue that only bright spots exist without any trailing shadow. The trailing edge is blurred away due to scattering in the thick layer of tissue.

In another situation, some struts have only a trailing shadow without a bright spot. These situations are very common in bad quality pullback runs as Fig. 6 (c) and (d) show. Both the expert and our detection method have difficulty to deal with these cases. The edge detection has difficulties to eliminate sew-up stitches as showed in Fig. 4 (f). Although the shadow edge based clustering can largely eliminate this problem, false edge may introduce false struts.

Unlike the guide wire which consists of a single wire cable, the stent patterns are much more complex. Without knowing the pattern of the implanted stent, it is difficult to remove or recover stent struts within the stented segment using the spatial information. Taking into account that there are hundreds of different stent designs, using the 3D stent structure information for stent strut detection is a very challenging task. In addition, the described method is not suitable for new bioabsorbable stent struts which appear as small dark boxes instead of bright spots in IVOCT images.

2.7 Conclusion and future research

With the high resolution of in-vivo microstructure in coronary arteries, IVOCT allows a better understanding of the pathophysiology of coronary disease. We presented an automatic stent strut detection method in IVOCT image sequences regardless of strut status and image quality. The new method uses the local image intensities to detect the candidate pixels of the stent struts in preprocessed IVOCT image sequences. The edges of the trailing shadows are detected to assist the candidate pixels clustering for each strut, to reduce the false positives and to find the dark struts with clear shadows. After clustering, the guide wire is filtered out using 3D restriction. The method is independent of pre-selection the strut status or lumen/vessel wall segmentation.

A clinical data analysis was carried out to evaluate the performance of our method. Automatic results were compared with the results that were manually detected by expert observers. For IVOCT images with different quality levels, it turned out to be a robust and reliable automatic method. In conclusion, with ongoing development of IVOCT technology, our method could be helpful for stent implanting treatment evaluation, patient follow up and vascular response of different types of stent. As a next step, the result will be used as input for 3D visualization and quantification.

2.8 References

1. Gebel, E (2008) Heart Disease a Leading Cause of Death Worldwide - Global research projects seek to end preventable heart attacks, strokes. American gov. http://www.america.gov/st/health-english/2008/July/20080724175631 abretnuh0.9819757.html

2. Raffel OC, Akasaka T, Jang I-K (2008) Cardiac optical coherence tomography. Heart 94:1200–10.

3. Feyter PJ, Nieman K (2002) New coronary imaging techniques: what to expect? Heart 87:195–7.

4. Hassan AK, Bergheanu SC, Stijnen T, van der Hoeven BL, Snoep JD, Plevier JW, Schalij MJ, Jukema JW (2010) Late stent malapposition risk is higher after drug-eluting stent compared with bare-metal stent implantation and associates with late stent thrombosis. European Heart Journal 1(10):1172-80.

5. van der Hoeven BL, Liem SS, Dijkstra J, Bergheanu SC, Putter H, Antoni ML, Atsma DE, Bootsma M, Zeppenfeld K, Jukema JW, Schalij MJ (2008) Stent malapposition after sirolimus-eluting and bare-metal stent implantation in patients with ST-segment elevation myocardial infarction. JACC Cardiovasc Interv. 1(2):192-201.

6. Guagliumi G, Sirbu V (2008) Optical coherence tomography: high resolution intravascular imaging to evaluate vascular healing after coronary stenting. Catheter Cardiovasc Interv. 72(2):237-47.

7. Prati F, Zimarino M, Stabile E, Pizzicannella G, Fouad T, Rabozzi R, Filippini A, Pizzicannella J, Cera M, De Caterina R (2008) Does optical coherence tomography identify arterial healing after stenting? An in vivo comparison with histology, in a rabbit carotid model. Heart 94(2):217-21.

Chapter

2

8.   Hoang KC, Edris A, Su J, Mukai DS, Mahon S, Petrov AD, Kern M, Ashan C, Chen Z, Tromberg BJ, Narula J, Brenner M (2009) Use of an oxygen-carrying blood substitute to improve intravascular optical coherence tomography imaging. Journal of Biomedical Optics 14(3):034028.

9.   Yun S, Tearney G, de Boer J, Iftimia N, Bouma B (2003) High-speed optical frequency-domain imaging. Opt. Express 11(22):2953-63.

10. Fercher AF (2010) Optical coherence tomography – development, principles, applications, Z. Med. Phys. 20(4):251-76.

11. Gurmeric S, Unal G, Carlier S, Yang Y, Slabaugh G (2008) Automatic stent implant follow-up in intravascular optical coherence tomography images. MICCAI-CVII: the international workshop on computer vision for intravascular imaging.

12. Unal G, Gurmeric S, Carlier SG (2010) Stent implant follow-up in intravascular optical coherence tomography images. Int J Cardiovasc Imaging 26(7):809-16.

13. Ughi GJ, Adriaenssens T, Onsea K, Kayaert P, Dubois C, Sinnaeve P, Coosemans M, Desmet W, D'hooge J (2011) Automatic segmentation of in-vivo intra-coronary optical coherence tomography images to assess stent strut apposition and coverage. Int. J Cardiovasc Imaging. 2012 Feb;28(2):229-4.

14. Suzuki N, Guagliumi G, Bezerra HG, Sirbu V, Rosenthal N, Musumeci G, Aprile A, Wang H, Kyono H, Tahara S, Simon DI, Rollins A, Costa MA (2011) The impact of an eccentric intravascular ImageWire during coronary optical coherence tomography imaging. Euro Intervention 6(8):963-9.

15. Unal G, Bucher S, Carlier S, Slabaugh G, Fang T, Tanaka K (2008) Shape-driven Segmentation of Intravascular Ultrasound Images. IEEE Trans Inf. Technol Biomed 12(3):335-47.

16. Gao WS, Yang L, Zhang XG, Zhou B, Ma CX (2010). Based on soft-threshold wavelet de-noising combining with Prewitt operator edge detection algorithm. Education Technology and Computer (ICETC), 2nd International Conference, Shanghai, China.

17. Jain AK, Murty MN, Flynn PJ (1999) Data clustering: a review. ACM Computing Surveys 31(3): 264-323.

CHAPTER

3

Automatic detection of bioresorbable vascular scaffold struts in intravascular optical coherence tomography pullback runs

Abstract

Bioresorbable vascular scaffolds (BVS) have gained significant interest in both the technical and clinical communities as a possible alternative to metallic stents. For accurate BVS analysis, intravascular optical coherence tomography (IVOCT) is currently the most suitable imaging technique due to its high resolution and the translucency of polymeric BVS struts for near infrared light. However, given the large number of struts in an IVOCT pullback run, quantitative analysis is only feasible when struts are detected automatically. In this paper, we present an automated method to detect and measure BVS struts based on their black cores in IVOCT images. Validated using 3 baseline and 3 follow-up data sets, the method detected 93.7% of 4691 BVS struts correctly with 1.8% false positives. In total, the Dice's coefficient for BVS strut areas was 0.84. It concludes that this method can detect BVS struts accurately and robustly for tissue coverage measurement, malapposition detection, strut distribution analysis or 3D scaffold reconstruction.

3.1 Introduction

In coronary artery disease (CAD), plaques build up in the vessels and obstruct the oxygen-rich blood supply to the heart muscle, which can cause angina or eventually a heart attack. Nowadays, stenting after angioplasty is one of the main treatment options for CAD. Stents are tiny tube-like devices that are usually made of metal meshes, designed to support the vessel wall to prevent the acute vessel recoil after the plain-old balloon angioplasty [1]. The first introduced stent was the bare metal stent (BMS), with a known risk of neointimal hyperplasia (NIH) which re-narrows of the vessel lumen [2]. The drug-eluting stent (DES) emerged as an alternative to the BMS. It can alleviate NIH significantly, but later, multiple risk factors became evident, such as late stent thrombosis and late acquired malapposition [3, 4]. As a result, a new concept of the temporary stent or scaffold was proposed. Such a device is designed to offer temporary radial strength to avoid the acute vessel closure as a consequence of the acute vessel recoil, and at a later stage, it will be fully absorbed, leading to restoration of lumen patency and vascular flow [5, 6]. A series of temporary vascular stents, termed "Bioresorbable Vascular Scaffold (BVS)", have been developed and undergone extensive clinical evaluation in the past ten years [4, 7-10]. ABSORB BVS (Abbott Vascular, Santa Clara, California, US) is one of first developed temporary scaffolds which have been used for clinical treatment. It consists of a backbone of poly-L-lactide coated with poly-D,L-lactide which contains and controls the release of the antiproliferative drug everolimus (Novartis, Basel, Switzerland) [11]. The thickness of backbone with coated drug layer is 158 µm. ABSORB BVS will be fully absorbed approximately two years after implantation and has exhibited strong positive clinical and angiographic results [12].

Chapter

3
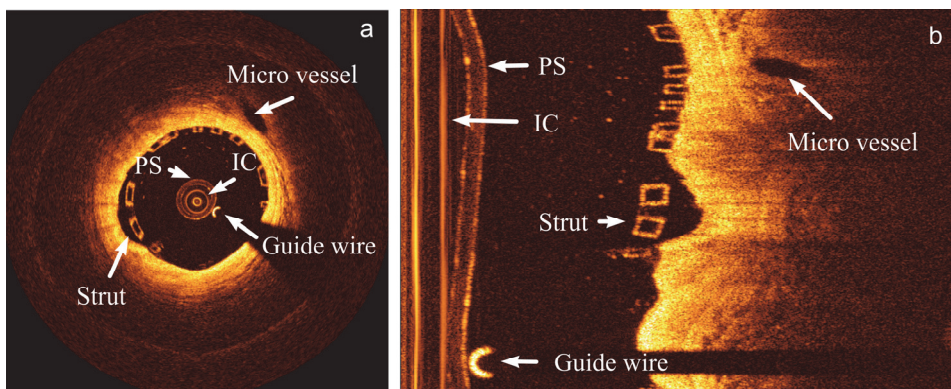
Figure 3-1. A baseline IVOCT image in (a) the Cartesian coordinate system and (b) the polar coordinate system. In both images, the imaging catheter (IC), the protective sheath (PS), the guide wire, a micro vessel and a BVS strut are marked.

Intravascular optical coherence tomography (IVOCT) is being increasingly used during BVS studies and clinical trials for accurate BVS analysis to assess the rate of bioresorption and to inspect the response of vessel walls [13]. As a relatively new optical signal acquisition technique, IVOCT imaging has a radial resolution of about 10 µm which is ten times higher than its comparable technique: intravascular ultrasound

(IVUS). IVOCT has a limited penetration of 3 mm, but it provides a better signal-to-noise ratio than IVUS within the limitation. Furthermore, IVOCT imaging is particularly suitable for BVS struts as they are made of translucent polymers [12]. The transmitted light can readily pass through them and backscattering originates from the difference in refractive index between a strut and its environment (flush fluid or tissue), which results in bright boundaries. Besides, if a strut contains a big fracture which appears as a scattering center, it looks similar to confluent struts [14]. An IVOCT image with newly implanted BVS struts in two different coordinate systems is shown in Fig. 1. There are different BVS strut shapes; however, struts having bright boundaries and box-shape black cores account for 100% of the shapes at baseline, more than 82% at 28 days and 80% at 24 months of all the struts [15]. Therefore in this paper we will focus on the box-shape type of BVS struts. The strut area is measured based on its black core. The bright boundary is not included since when a strut is covered by tissue, its boundary cannot be precisely defined, while for a newly implanted strut, its thickness will be overestimated by measuring the distance between the leading-edges of its adluminal wall and abluminal wall [12].

Many automated metallic stent strut detection methods [16-19] have been published. However, to the best of our knowledge, current BVS analyses in IVOCT images still rely on the labor intensive manual delineation of struts. Given the large number of struts in a pullback run, quantitative analysis is feasible only when struts can be detected automatically. In this paper, we present an automated method to detect BVS struts and to measure their black core areas in IVOCT pullback runs.

3.2 Method

To detect struts accurately, a-priori information of the input IVOCT data set type (baseline or follow-up) is requested, as the presented algorithm has two slightly different strategies for baseline and follow-up images with respect to some different parameters, false positive filters and the region of interest (ROI). However, in this section, the described procedures are implicitly used for both strategies, unless stated differently in context. As Fig. 2 shows, both strategies contain five main steps: **1**) Pre-processing. The bright components in the lumen including the imaging catheter, the guide wire and the protective sheath should be detected and masked; **2**) Image transformation. The lumen contour and center are detected so that we can transform Cartesian IVOCT images into new polar images based on the lumen center. In the new polar images, the shapes of BVS struts are usually more rectangular than these in the original polar images; **3**) Candidate strut detection. In the new polar images, short candidate segments describing black cores are detected and later clustered as candidate struts; **4**) False positive removal. These are removed using a series of false positive filters; **5**) Strut contour refining. The strut contours are refined to be smooth and accurate for area measurement and center calculation. In the following subsections, each step of the method is described in more detail.
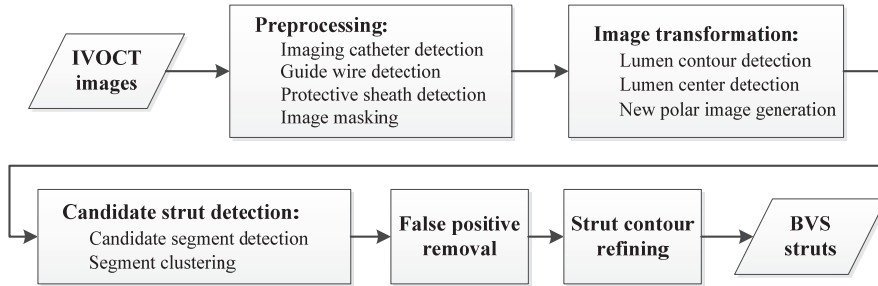
Figure 3-2. The flow chart of the BVS strut detection method.

3.2.1 Preprocessing

Bright components inside the lumen, including the imaging catheter, the guide wire and the protective sheath, were masked to improve the further processing. The imaging catheter center is the center of Cartesian images, and as Fig. 1(a) shows, the imaging catheter produces a series of very bright concentric circles, which appear as vertical lines in the polar images as presented in Fig. 1(b). After a proper Z-offset correction, the imaging catheter is located in the same position in the whole pullback run and hence can be detected in the minimum image of the entire pullback run by checking the intensity sum of every column [20]. If a guide wire is used during the image acquisition, it blocks the light signal and consequently generates a black shadow behind it. According to its intensity profile, the guide wire and its shadow were detected using a previously developed method [21].

The imaging catheter is always covered by a protective sheath which appears as a ring with a certain width dependent on the manufacturer and catheter type. During the image acquisition, the imaging catheter moves sideways inside the protective sheath, thus the protective sheath position varies during the pullback and therefore must be detected frame by frame. First, a ROI was defined for the detection. It started from the outer wall of the imaging catheter and was wide enough to cover the protective sheath. As the protective sheath diameter and the image resolution are known, a proper width of the ROI can be computed. Next, the Prewitt compass edge filter with a kernel sensitive to vertical edges [22] was applied to the image, so that the outer (bright-to-dark) edge of the protective sheath was represent by strong negative values. The gradient image was used as a cost matrix to which Dijkstra's algorithm [23] was applied to detect the minimum cost path dynamically. This path is the outer boundary of the protective sheath. An example of the detection results of the imaging catheter, the protective sheath and the guide wire shadow region is given in Fig. 3(a). To avoid creating new dark to bright edges that may influence the lumen contour detection, the image region inside the protective sheath was masked using the background intensity value. It was computed based on a fixed percentile of the histogram of the entire image sequence. An example of the preprocessed image is presented in Fig. 3(b).

Chapter

3
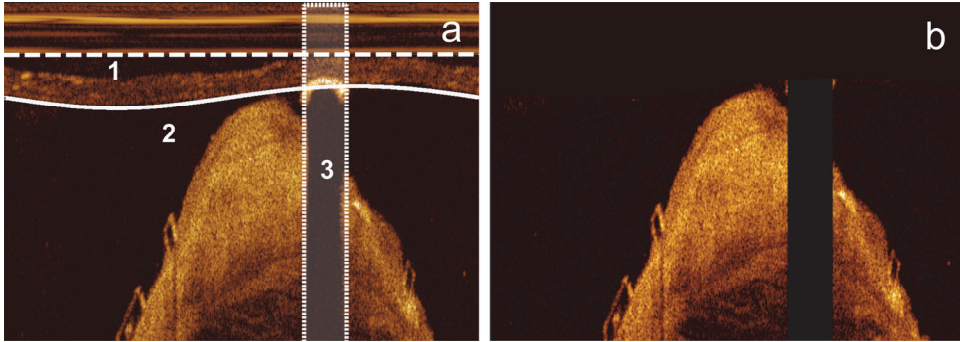
Figure 3-3. The detected imaging catheter (dashed straight line "1"), protective sheath (solid curve "2") and guide wire shadow region (area "3") are given in figure (a). The masked image is given in figure (b). Inside the protective sheath, it is masked with the background intensity value, while the guide wire shadow region is masked as 0.

3.2.2 Image transformation

Our BVS strut detection is applied to polar images. However, the box-shape BVS struts are usually distorted like parallelograms in the original polar images, since they are converted from Cartesian images based on the catheter center instead of the stent contour center. To improve the BVS strut appearance, new polar images should be created from Cartesian images based on the stent contour center. As lumen contour is similar to the stent contour in most of the cases, its center was used as an approximation of the stent contour center.
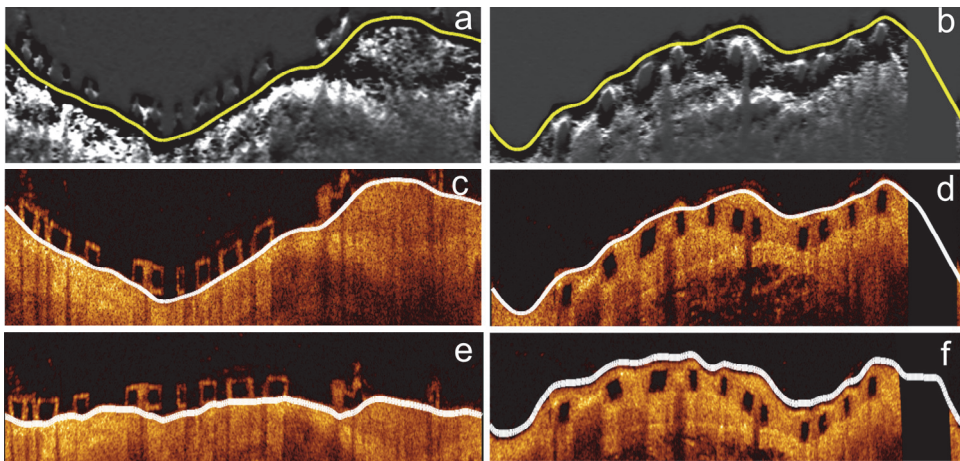
Figure 3-4. The gradient images of a baseline image and a follow-up image are given in figures (a) and (b). They are used for lumen detection. Yellow curves indicate the detected minimal cost paths. In figures (c) and (d), the original polar images are presented with lumen contours (white curves). The new polar images transformed based on the lumen center are shown in figures (e) and (f) in which most of the BVS struts are more rectangular than in original polar images.

The lumen boundary was detected in the original polar images. First, the images were denoised using a median filter [24] to smooth the lumen boundary. Next, a gradient image was generated by applying the Prewitt compass edge filter with the kernel for vertical edges to the smoothed image. Two examples are given in Figs. 4(a) and 4(b). In the gradient image, the lumen boundary is represented by strong negative values and hence Dijkstra's minimum cost path detected in it was treated as the lumen boundary as Figs. 4(c) and 4(d) demonstrate. The detected lumen boundary was converted into the Cartesian coordinates system and its center was detected using a distance transformation method presented in [25]. Based on the lumen center, a Cartesian image can be transformed into a new polar image like Fig. 4 (e). Compared with the original polar images, the shapes of most BVS strut are more rectangular. However, in some cases, the lumen contour is highly irregular, so that BVS struts are still not rectangular after the image transformation as Fig. 4(f) shows. They have irregular shapes and different thickness in the vertical direction. The proposed method contains procedures to detect these irregular struts in the further steps, but in the worst situation, these struts cannot be detected.

3.2.3 Candidate strut detection

In the new transformed polar images, candidate BVS struts were detected. As mentioned in the beginning, the presented method has two different strategies to detect baseline and follow-up struts, separately. There are three main differences between them:

1. Different ROI for strut detection. For baseline data sets, the struts are usually aligned with the lumen boundary or malapposed, which means most of the struts are inside the lumen contour as Fig. 4(e) demonstrates. However, the lumen detection may be affected by confluent struts or struts placed inside the tissue, so that the detected lumen contour may follow the front wall of these struts instead of the back wall. To cover all the baseline struts, the detected lumen contour needs to be extended with an offset equal to BVS strut thickness. The ROI of baseline strut detection is between this extended contour and the previously detected protective sheath contour. In contrast, in the follow-up data sets, most of the BVS struts are outside the lumen contour as Fig. 4(f) shows, but when some struts are not covered by tissue, the detected lumen contour could pass behind them mistakenly. To include all the follow-up struts, we need to shrink the lumen contour to the lumen center direction with an offset equal to BVS strut thickness. Therefore, the ROI for follow-up strut detection is between the shrunken lumen contour and the image boundary.

2. Different thickness threshold. After implantation, BVS struts start to be degenerated and covered by healing tissue. Hence, the boundaries of the follow-up struts are less sharp than newly implanted struts. Consequently, the method uses a slightly bigger thickness threshold to detect follow-up struts than the newly implanted struts. This parameter is set based on the image resolution and will be described later in this section.

3. Different degree of the boundary completeness. The boundary of a newly implanted strut usually contains many small gaps as Fig. 4(c) shows. Because a baseline strut is not covered by tissue, its box-shape boundary is mostly created by the backscattering at the strut surfaces which could be affected by the strut position and orientation. Parts of the boundary could be blurred or even missing. Moreover, the residual blood and other artifacts also can affect the completeness of the box-

structure. At follow-up stage, struts are usually covered by tissue which helps to generate bright boundaries as Fig. 4(d) shows. Compared with the newly implanted struts, the follow-up struts have a more complete box-shape boundary and hence the method is stricter with regard to their boundary shape and completeness.
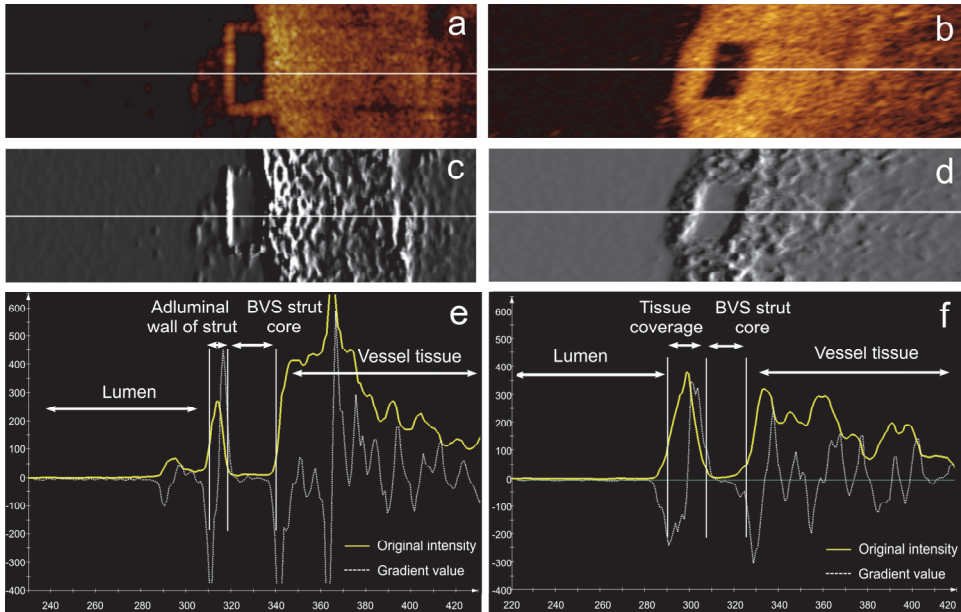
Figure 3-5. Figures (a) and (b) show a scan-line (white line) passing through a BVS strut in a baseline image and a follow up image, respectively. The corresponding gradient images are presented in figures (c) and (d). The intensity profile (yellow curve) and the gradient profile (white curve) are given in figures (e) and (f). A BVS strut always has low intensity values in the black core region and strong gradient values along the boundary.

In the ROI, we first detected the candidate line segments between the front and back walls of BVS struts scan-line by scan-line and later clustered these segments into candidate struts. To detect candidate segments, both original and gradient images were used. Again, the Prewitt compass edge filter for vertical edges was applied to generate gradient images in which dark-to-bright edges are represented by negative values and bright-tot-dark edges are positive values. The intensity profile and the gradient profile of a scan-line that passes through a BVS strut are given in Fig. 5. According to these profiles, one can state that the BVS region starts with a relatively high intensity (front wall) followed by a certain low intensity region (black core) and it ends with another relatively high intensity (back wall). As a result, candidate segments constituting BVS struts were detected with four main rules:

1. It has low intensity black core region. In this method, the low black core intensity threshold was calculated based on a fixed percentile of the histogram of the pullback run.

2. It has a strong positive gradient value in the beginning and a strong negative gradient value in the end. Both the gradient value thresholds were computed according to fixed percentiles of the histogram of the gradient images.

Chapter

3
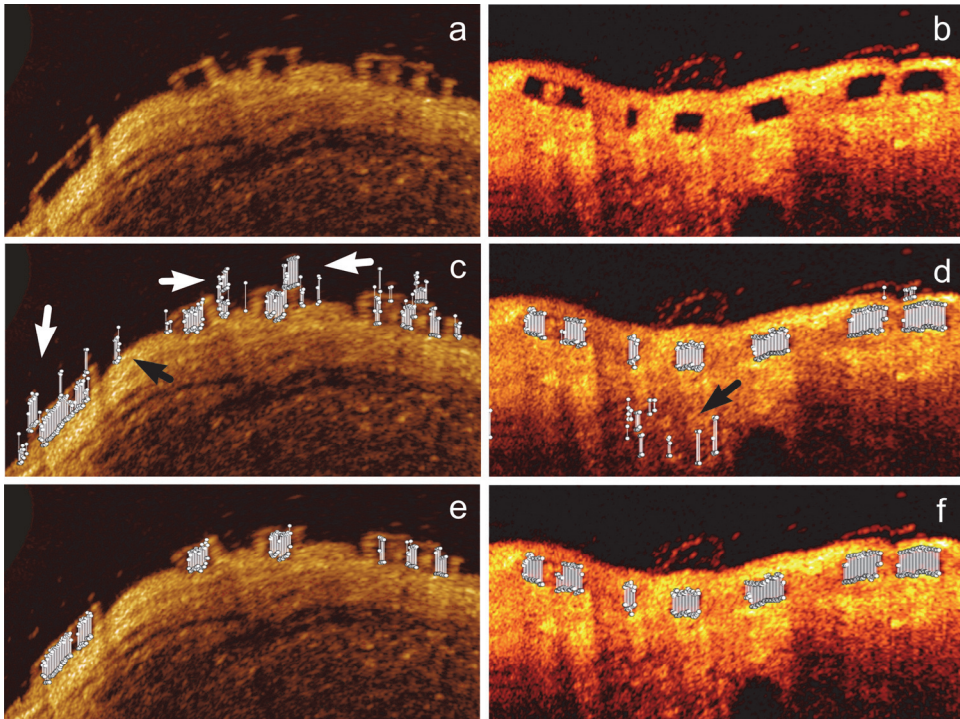
Figure 3-6. Figure (a) shows a new polar baseline image that is transformed based on the center of Figure (a) shows a new polar baseline image that is transformed based on the center of a highly irregular lumen contour. The BVS struts in figure (a) still appear distorted and their thickness in the vertical direction is very different. Figure (b) demonstrates a follow-up image transformed based on the center of a circular lumen contour. The BVS struts are less distorted than these in figure (a). The detected candidate line segments (short white lines) are presented in both figures (c) and (d). Both white and black arrows point out the candidate segments caused by residual blood or noise in tissue. These candidates will be clustered as false candidate strut during the clustering. After the false positive removal, only real struts are left as figures (e) and (f) shows.

3. It has a reasonable length. Segment length represents the strut thickness in scan-line direction. Ideally, the thickness of BVS struts in a pullback run should be the same in each scan-line. However, BVS struts could still appear distorted after the image transformation in section 2.2, since the lumen is not always circular. Moreover, the strut boundary thickness can be influenced by the distance and orientation of the struts. Struts close to the imaging catheter or uncovered by tissue usually are characterized by a wider boundary. Therefore, the thickness of the strut cores in a single pullback run can be different from the standard thickness. In our approach, a

range of acceptable thicknesses of BVS strut cores was set based on the standard thickness.

4. Candidate segments should not be overlaid in the same scan-line. In case the noise has stronger edge than real struts, the algorithm allows more than one candidate segment in the same scan-line. However, when two candidate segments were found overlaid in the same scan-line, only the one having the highest intensity sum of the front and back walls was selected. If they both had the same intensity sum, the longest one was saved.

For example, the candidate segment results for Figs. 6(a) and 6(b) are presented in Figs. 6(c) and 6(d), which still contain some false candidate segments. They are generated due to the residual blood, micro-vessels, plaques and weak signal region deep in the tissue.

After having obtained the BVS candidate segments, a clustering method was applied to merge these segments into candidate struts. As Figs. 6(c) and 6(d) show, the candidate segments belonging to the same BVS strut are connected, while the false positives are usually randomly distributed. In this method, the segments were clustered according to their position. It started from the first un-clustered candidate segment and searched for the next segment close to it. A candidate segment can be added to the cluster if it is connected with the last segment in the cluster. The searching continues until no more segments can be attached. Next, we checked if a cluster has top and bottom boundaries as BVS struts should have box-shape boundaries. The follow-up BVS strut boundary is usually complete due to the tissue coverage so that only clusters having both top and bottom edges were saved. In baseline data sets, the BVS strut could have an incomplete box-structure, so that the method allows a cluster to miss its top or bottom boundaries.

3.2.4 False positive removal

During the clustering, many false candidate struts were generated from false candidate segments as presented in Figs. 6 (c) and 6(d). Therefore, a series of false positive filters were applied to the clustering results to remove them. First, the strut size was used for filtering. A BVS strut should contain a certain number of candidate segments. Small clusters are usually caused by random noise or artifacts in the images. In our research, clusters containing less than 3 candidate segments were removed as false positives. A second filter was applied to search for overlaid struts in each scan-line, because there should be at most one strut in any radial direction, but some false positives can share parts of the boundary with real struts. As a result, when two clusters were overlaid in the radial direction, only the one with complete box-structure was saved. If both clusters had complete box-structures, the bigger cluster was kept.

The third filter is only applicable for follow-up data sets. After the first two filters, a few false positives may still exist in the deep tissue region which contains much random noise due to the weak signal. Compared with the true positives, these false positives were commonly located deeper in the tissue; therefore, a filter was applied to remove outliers based on the thickness of tissue coverage (the distance between struts and the lumen boundary) for each candidate strut, so that a candidate strut having a very different thickness of tissue coverage with the majority was considered as a false positive, since the thickness of tissue coverage changes smoothly in the follow-up data sets. After the previous filtering, the majority of current results should be true

positives. Therefore, the median coverage thickness was computed for outlier detection. To be accurate, the clusters in the neighboring frames were used to estimate the median coverage thickness as well. This filter also removed most of the false positives caused by micro vessels and plaques. However, it is not applicable for baseline data sets, as the malapposed struts could have very different distances to the lumen boundary. Examples of the false positive removal results are given in Figs. 6 (e) and 6(f).

3.2.5 Strut contour refining

After false positive removal, the main bodies of the strut black cores were detected. As the candidate segments were always selected with the strongest boundary intensity, the detected adluminal and abluminal walls of BVS struts were usually rough. Besides, the original boundary could be fluctuating because of the noise, inside fractures and low image quality. Examples of the unsmoothed BVS strut contours are shown in Fig. 7(a). Therefore, the front wall and back wall of each detected strut were smoothed using a median filter. Any outliers were replaced by the interpolated point between the nearest neighboring points. The smoothing results are show in Fig. 7(b).
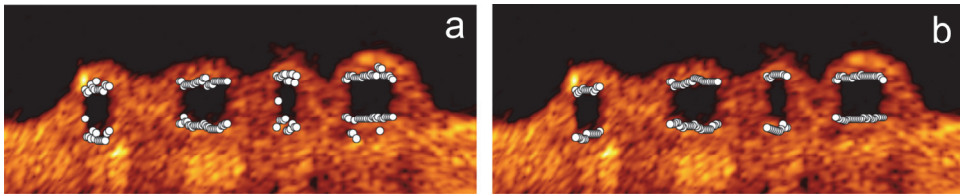
Figure 3-7. The original boundaries of clusters formed by white points in figure (a) and the smoothed boundaries in figure (b).
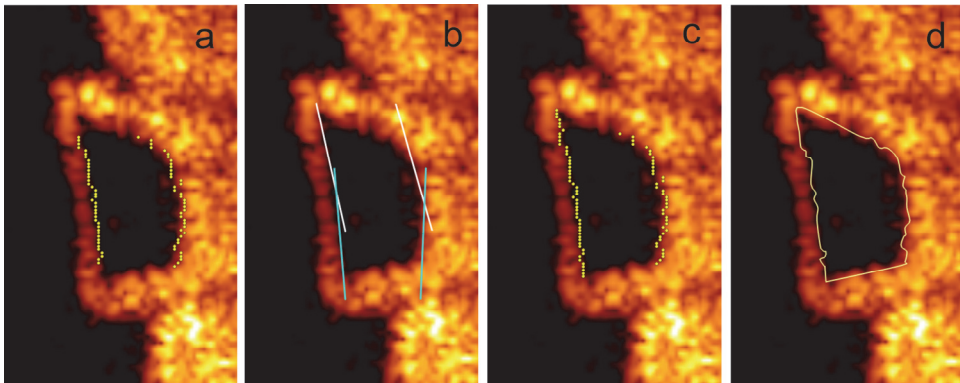
Figure 3-8. Figure (a) shows the smoothed boundaries of a cluster in yellow dots. In figure (b), two white lines are fitted to the top part of the strut boundary and two light blue lines are fitted to the bottom part of the strut boundary. Along the fitted lines, the missed boundaries in the sharp tip regions are recovered as figure (c) demonstrated and the final refined strut contour is generated as (d) presents.

The main bodies of the strut cores were formed by line segments with a range of acceptable thickness. However, an irregular shape strut could contain sharp tips in

one or both ends as Fig. 8(a) shows. The core regions in the sharp tips have smaller thickness than the acceptable thickness and usually contain more noise than the main body. As a result, the sharp tip regions might be missed during the detection. To recover these tip regions, a post-processing was applied. First, the adluminal and abluminal boundaries were fitted into lines using the least-square error method and the fitted lines specify the ROI for tip refining. Due to the irregular lumen contour, a long BVS strut could be curved, so its front and back walls cannot be fitted into one single line. To be accurate, we fitted two separated lines for the top and bottom boundary of the struts containing more than 20 candidate segments as Fig. 8(b) presents. Next, along the fitted lines, the adluminal and abluminal walls for the missed sharp tip regions were recovered by searching continuous boundaries in the Prewitt edge filtered polar images. The searching ended when the fitted line met the top or bottom edges. The recovered boundary can be seen in Fig. 8(c). In the end, a spline contour was generated for each BVS strut based on the refined boundary as Fig. 8(d) shows. At the same time, the center of each BVS strut was calculated.

3.3 Validation and results

The automatic BVS strut detection and measurement method was developed using the MeVisLab toolbox (Fraunhofer MeVis, Bremen, Germany) together with in-house developed C++ modules. For validation purposes, 6 pullback runs were used which were acquired using a C7-XR FD-OCT intravascular imaging system together with a C7 Imaging catheter (St. Jude Medical Inc., St. Paul, MN, USA). The automated pullback speed was 20 mm/s with a data frame rate of 100 frames per second. All the pullback runs are in the original 16-bit polar format and each contains 271 frames. Three pullback runs were acquired at baseline, while the other three at 6 to 24 months, respectively. In both baseline and follow-up groups, one pullback run contains no guide wire and the other two contain a standard 0.014 inch steerable guide wire. Temporary blood flushing was performed with a contrast infusion. All the stents are the ABSORB 1.1 bioresorbable vascular scaffold (Abbott Vascular, Santa Clara, CA, USA). Overtime struts are absorbed. According to the trails for the ABSROB BVS [15], there is about 9% reduction of struts in IVOCT images over 6 months and 35% reduction over 24 months. Already due to the difference in position of the IVOCT catheter for the same scaffold at the same time point, there could be a difference in the number of struts. In our study, the baseline and follow up data sets are from different patients and therefore the number of struts is different. Part of the BVS struts could become undetectable after 24 months, but every visible strut in the 6 in-vivo IVOCT pullback runs were used for validation purposes, including struts without box-shape and the struts partly blocked by guide wire shadows.

To generate the ground truth, one observer manually drew all 4691 black cores of BVS struts in the 6 pullback runs, 2183 cores from the baseline group and 2508 from the follow-up group. A second independent observer manually drew all the struts in a subset containing one baseline data set and one follow-up data set. The second observer drew one contour for a strut with big fractures. These struts contain more than one black core, and have similar appearance as confluent struts. Therefore, the ground truth from the second observer contains some bright regions between black cores compared with that from the first observer as Figs. 9(a) and 9(b) shows. For incomplete struts, both observers marked the contour based on experience. In total, 726 newly implanted struts and 795 follow-up struts were marked by the second

observer. In the same subset, the first observer marked 783 baseline cores and 819 follow-up strut cores. The agreements for BVS strut were given in Sensitivity and the core area agreements were computed using the Dice's coefficient. The inter-observer agreement of the BVS struts was 98.8% for baseline struts and 99.6% for follow-up struts. The strut area similarity was both 0.83 in the baseline group and the follow-up group. The area difference is mainly because the first observer did not include the bright region caused by big fractures.
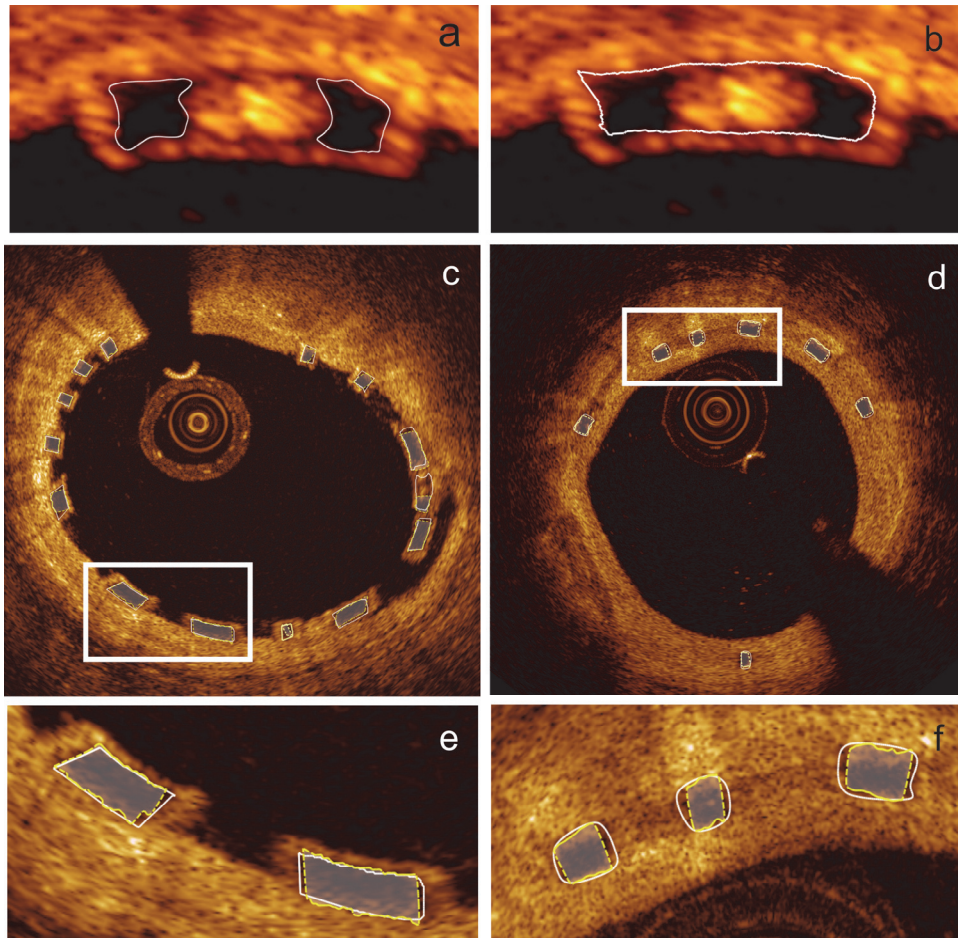
Figure 3-9. Figure (a) shows two black cores marked by the first observer and they were marked as a big strut by the second observer as figure (b) presents. A comparison of the ground truth (solid white contours) from the second observer and the algorithmic results (dashed yellow contour with white translucent mask) in a baseline image is presented in figure (c) and another comparison of the ground truth from the first observer and the algorithmic results in a follow-up image is given in figure (d). The enlarged images of the white rectangle regions are given in figures (e) and (f).

During the evaluation, if a detected strut overlays the area of a ground truth, it was counted as a true positive. Otherwise, it is a false positive. The accuracy of black core

area was measured by Dice's coefficient as well. According to the first observer, on average, the method correctly detected 90.0 ± 3.2% struts with 3.1 ± 0.7% false positives in every baseline data set and the Precision was 97.0 ± 0.1%. The Dice's coefficient for the BVS strut area was 0.83 ± 0.02. If we measure only the area of the correctly detected struts, the Dice's coefficient was 0.86 ± 0.01. For the follow-up group, the method detected 96.6 ± 2.0% struts correctly with only 0.8 ± 0.8% false positives and the Precision was 99.2 ± 0.1%. The Dice's coefficient for the strut area was 0.85 ± 0.02. For only the true positive struts, the number was 0.86 ± 0.01. According to the second observer, the method successfully detected 90.8% of baseline struts with 4.3% false positives and the Precision was 95.9%. 92.6% of follow-up struts were detected with 2.2% false positives and the Precision was 97.7%. The Dice's coefficient for baseline and follow-up strut areas was 0.76 and 0.75, separately. Counting only true positive areas, the Dice's coefficient was 0.79 and 0.77. Some examples of the ground truth from both observers and algorithmic results are given in Figs. 9(c)–9(f). The strut detection and the area measurement performance for each individual pullback run are presented in Table 1 and Table 2, separately.

The center position error of the correctly detected strut was computed as well. The average distance error of the strut centers was 17.0 ± 22.5 μm for newly implanted struts, 13.9 ± 11.1 μm for follow-up struts and 15.3 ± 21.0 μm for all struts. The median distance errors for two groups were both 11.1 μm.

Table 1. The strut detection results of the presented method for each validation data set. For each data set, the number of frames containing struts (Frame No.), the numbers of struts in the ground truth (GT), the percentages of true positive (TP) and false positive (FP) are given

Strut status	Data set	Frame No. (with struts)	No. of GT	TP (%)	FP (%)
Baseline	1	89	630	85.5	3.8
	2	94	770	92.2	3.3
	3	93	783	92.5	2.0
Follow-up	4	97	868	93.7	0.0
	5	91	819	98.0	0.6
	6	97	821	90.4	1.8
Total	-	561	4691	93.7	1.8

Table 2. The strut area measurement performance of the present method in each validation data set. The area of the ground truth (GT) and the Dice's coefficient between the ground truth and the algorithmic results are given for all struts and only successfully detected struts

Strut status	Data set	Area of all struts		Area of only true positives	
		GT area (mm^2)	Dice	GT area (mm^2)	Dice
Baseline	1	16.4	0.81	15.0	0.86
	2	14.3	0.82	13.7	0.85
	3	15.9	0.85	15.4	0.87
Follow-up	4	20.1	0.87	19.9	0.88
	5	19.8	0.83	19.0	0.85
	6	18.3	0.84	18.0	0.85
Total	-	104.8	0.84	101.0	0.86

3.4 Discussion

According to the validation results, the algorithm successfully detected 96.6 ± 2.0% follow-up struts with only 0.8 ± 0.8% false positives and 90.0 ± 3.2% newly implanted struts with 3.1 ± 0.7% false positives. The strut center error was 15.3 ± 21.0 μm. Generally, the presented method is accurate and robust under different image circumstances. The performance for the follow-up group is slightly better than the baseline group, because follow-up BVS struts have more complete box-shape boundaries due to the tissue coverage. Backscattering on the interface between struts and tissue creates strong bright boundaries. By checking the boundary completeness during the clustering, the algorithm can easily remove most of the false positive from the follow-up pullback runs. In contrast, the contour of newly implanted struts can be influenced by noise in the lumen, such as residual blood, and hence contains many gaps. The algorithm keeps the clusters that have mild incomplete boundaries to avoid removing too many true positives, but fails to keep the real struts having severe incomplete boundaries. On the other hand, it also leaves more false positives in the results than the follow-up data set. Most of these false positives can be later removed by the filters, but still a few could leave as they are difficult to distinguish. Actually, most of the final false positives are from the baseline group. Similarly, the strut area performance in the follow-up pullback runs (0.85 ± 0.02) is also better than in the baseline pullback runs (0.83 ± 0.02).

When a BVS strut fractures, it generates bright scattering regions that separate the strut into several black cores as Fig. 9(a) shows. In this case, the first observer marked each cores separately, while the second observer drew one big contour for all the cores including the bright fractures as Fig. 9(b) presents. Hence, the manual results from the second observer contain fewer struts but more strut areas than those from the first observer, and the false positive rate according the second observer is 3.2% and the Dice's coefficient for the strut area is 0.75. However, if we count only the agreed areas between two observers, 95.1% and 96.9% of these areas were correctly detected for baseline and follow-up groups, separately. It suggests that the algorithmic results have a good agreement with the black core regions from both observers. The area errors in

the baseline data sets are largely caused by incomplete boundaries, because the strut areas may be overestimated or underestimated. The area errors for follow-up struts are mainly due to the blurred boundary edges, because struts are slowly bioresorbed after implantation. Tissue coverage also weakens the sharpness of strut boundaries. As this method prefers strong edges when detecting struts, the final follow-up strut contours could be distorted.

The strut detection also replies on the proper preprocessing. The imaging catheter, the guide wire and the protective sheath should be removed to facilitate the lumen detection. Besides, these bright components also can negatively impact the baseline strut detection. The lumen center is used as an approximation of the stent contour center. After transforming the Cartesian image to a new polar image based on the lumen center, we could get more rectangular strut contours. However, when the lumen contour is highly irregular, the BVS strut in the transformed polar image could be still distorted like a parallelogram and in many cases, the strut edges are not straight. Therefore, the thickness and the shape of these struts could vary a lot during in the pullback run. To handle this situation, the presented method allows a range of acceptable thickness instead of only the standard thickness to detect as many candidate segments as possible, and in the end, refines irregular strut contours to be more accurate. In a rare case, a strut can be highly distorted in the new polar image and therefore, cannot be detected by this method.

Most of the parameters used in the presented method are related to the image size and image resolution, while the remaining three parameters were set based on the histogram of the original images or the gradient images. These parameters are the minimum intensity threshold for strut boundary, the minimum absolute gradient threshold for edges and the maximum intensity threshold for black core regions. One data set from each group was used for parameter tuning. The same parameter setting was applied to all the pullback runs during the validation.

The presented method also has limitations. The BVS struts can have four different appearances: preserved box, open box, dissolved black box and dissolved bright box [15]. This method can only detect the majority of the cases, being the preserved box, which has a closed high intensity boundary and a low intensity core. All other three types cannot be detected. It also has limitations to handle struts with an incomplete boundary. Moreover, in a few cases, BVS struts can be overlaid after the implantation, but our method cannot detect the overlapping BVS struts, because a false positive filter checks all the overlapping results in radial direction. Only one of these struts could be left in the results. This research is based on the ABSORB 1.1 BVS struts; hence our results cannot be directly generalized to other type of BVS struts which may have different appearance with ABSORB 1.1 BVS after implantation and during the follow up.

3.5 Conclusion and future work

In conclusion, with the ongoing development of BVS technology, automated BVS strut detection methods become important as they can simplify and speed the quantitative analysis for both clinical research and medical care. In this paper, we implemented an automatic method to detect and measure BVS struts based on the black core region in both baseline and follow-up IVOCT image sequences. The validation results suggest that the proposed algorithm is very accurate and robust,

which could be a helpful tool for tissue coverage thickness measurement, strut distribution analysis, 3D visualization, BVS bioresorption validation and vascular response research. In future, we plan to improve the current detection method and to detect BVS struts without box-shape contours.

3.6 References

1.   A. Grüntzig, "Transluminal dilatation of coronary-artery stenosis," Lancet 311, 263 (1978).

2.   J. E. Sousa, P. W. Serruys, and M. A. Costa, "New frontiers in cardiology: drug-eluting stents: Part I," Circulation 107, 2274-2279 (2003).

3.   B. Kalesan, T. Pilgrim, K. Heinimann, L. Raber, G. G. Stefanini, M. Valgimigli, B. R. da Costa, F. Mach, T. F. Luscher, B. Meier, S. Windecker, and P. Juni, "Comparison of drug-eluting stents with bare metal stents in patients with ST-segment elevation myocardial infarction," Eur Heart J 33, 977-987 (2012).

4.   P. W. Serruys, A. T. Ong, J. J. Piek, F. J. Neumann, W. J. van der Giessen, M. Wiemer, A. Zeiher, E. Grube, J. Haase, L. Thuesen, C. Hamm, and P. C. Otto-Terlouw, "A randomized comparison of a durable polymer Everolimus-eluting stent with a bare metal coronary stent: The SPIRIT first trial," EuroIntervention. 1, 58-65 (2005).

5.   S. Brugaletta, H. M. Garcia-Garcia, Y. Onuma, and P. W. Serruys, "Everolimus-eluting ABSORB bioresorbable vascular scaffold: present and future perspectives," Expert.Rev.Med.Devices 9, 327-338 (2012).

6.   C. I. Stefanadis, "Stents for coronary artery disease: from covered to drug-eluting to bioabsorbable," Hellenic J Cardiol 53, 89-90 (2012).

7.   D. Dudek, Y. Onuma, J. A. Ormiston, L. Thuesen, K. Miquel-Hebert, and P. W. Serruys, "Four-year clinical follow-up of the ABSORB everolimus-eluting bioresorbable vascular scaffold in patients with de novo coronary artery disease: the ABSORB trial," EuroIntervention 7, 1060-1061 (2012).

8.   J. Gomez-Lara, S. Brugaletta, R. Diletti, S. Garg, Y. Onuma, B. D. Gogas, R. J. van Geuns, C. Dorange, S. Veldhof, R. Rapoza, R. Whitbourn, S. Windecker, H. M. Garcia-Garcia, E. Regar, and P. W. Serruys, "A comparative assessment by optical coherence tomography of the performance of the first and second generation of the everolimus-eluting bioresorbable vascular scaffolds," Eur Heart J 32, 294-304 (2011).

9.   A. Karanasos, C. Simsek, P. Serruys, J. Ligthart, K. Witberg, R. J. van Geuns, G. Sianos, F. Zijlstra, and E. Regar, "Five-year optical coherence tomography follow-up of an everolimus-eluting bioresorbable vascular scaffold: changing the paradigm of coronary stenting?," Circulation 126, e89-e91 (2012).

10. P. W. Serruys, J. A. Ormiston, Y. Onuma, E. Regar, N. Gonzalo, H. M. Garcia-Garcia, K. Nieman, N. Bruining, C. Dorange, K. Miquel-Hebert, S. Veldhof, M. Webster, L. Thuesen, and D. Dudek, "A bioabsorbable everolimus-eluting coronary stent system (ABSORB): 2-year outcomes and results from multiple imaging methods," Lancet 373, 897-910 (2009).

Chapter

3

11. P. W. Serruys, Y. Onuma, J. A. Ormiston, B. B. de, E. Regar, D. Dudek, L. Thuesen, P. C. Smits, B. Chevalier, D. McClean, J. Koolen, S. Windecker, R. Whitbourn, I. Meredith, C. Dorange, S. Veldhof, K. Miquel-Hebert, R. Rapoza, and H. M. Garcia-Garcia, "Evaluation of the second generation of a bioresorbable everolimus drug-eluting vascular scaffold for treatment of de novo coronary artery stenosis: six-month clinical and imaging outcomes," Circulation 122, 2301-2312 (2010).

12. A. Sheehy, J. L. Gutierrez-Chico, R. Diletti, J. P. Oberhauser, T. Glauser, J. Harrington, M. B. Kossuth, R. J. Rapoza, Y. Onuma, and P. W. Serruys, "In vivo characterisation of bioresorbable vascular scaffold strut interfaces using optical coherence tomography with Gaussian line spread function analysis," Eurointervention 7, 1227-1235 (2012).

13. N. Gonzalo, P. W. Serruys, N. Piazza, and E. Regar, "Optical coherence tomography (OCT) in secondary revascularisation: stent and graft assessment," EuroIntervention. 5 Suppl D, D93-D100 (2009).

14. J. L. Gutierrez-Chico, M. D. Radu, R. Diletti, A. Sheehy, M. B. Kossuth, J. P. Oberhauser, T. Glauser, J. Harrington, R. J. Rapoza, Y. Onuma, and P. W. Serruys, "Spatial distribution and temporal evolution of scattering centers by optical coherence tomography in the poly(L-lactide) backbone of a bioresorbable vascular scaffold," Circ J 76, 342-350 (2012).

15. B. D. Gogas, V. Farooq, Y. Onuma, and P. W. Serruys, "The ABSORB bioresorbable vascular scaffold: an evolution or revolution in interventional cardiology?," Hellenic J Cardiol 53, 301-309 (2012).

16. S. Gurmeric, G. G. Isguder, S. Carlier, and G. Unal, "A new 3-D automated computational method to evaluate in-stent neointimal hyperplasia in in-vivo intravascular optical coherence tomography pullbacks," Med.Image Comput.Comput.Assist.Interv. 12, 776-785 (2009).

17. G. Unal, S. Gurmeric, and S. G. Carlier, "Stent implant follow-up in intravascular optical coherence tomography images," Int.J.Cardiovasc.Imaging 26, 809-816 (2010).

18. C. Xu, J. M. Schmitt, T. Akasaka, T. Kubo, and K. Huang, "Automatic detection of stent struts with thick neointimal growth in intravascular optical coherence tomography image sequences," Physics in medicine and biology 56, 6665-6675 (2011).

19. A. Wang, J. Eggermont, N. Dekker, H. M. Garcia-Garcia, R. Pawar, J. H. C. Reiber, and J. Dijkstra, "A robust automated method to detect stent struts in 3D intravascular optical coherence tomographic image sequences," Proc. SPIE 8315, 83150L (2012).

20. G. Unal, S. Bucher, S. Carlier, G. Slabaugh, T. Fang, and K. Tanaka, "Shape-driven segmentation of the arterial wall in intravascular ultrasound images," IEEE Trans Inf Technol Biomed 12, 335-347 (2008).

21. A. Wang, J. Eggermont, N. Dekker, H. M. Garcia-Garcia, R. Pawar, J. H. Reiber, and J. Dijkstra, "Automatic stent strut detection in intravascular optical coherence tomographic pullback runs," Int J Cardiovasc Imaging 29, 29-38 (2013).

22. J. M. S. Prewitt, "Object enhancement and extraction," in *Picture Processing and Psychopictorics*, B. S. Lipkin, ed. (Academic Press, New York, 1970), pp. 75-149.

23. E. W. Dijkstra, "A note on two problems in connexion with graphs," Numer. Math. 1, 269-271 (1959).

24. W. K. Pratt, *Digital image processing* (John Wiley & Sons, Inc., 1978), p. 750.

25. A. Wang, J. Eggermont, N. Dekker, P. J. de Koning, J. H. Reiber, and J. Dijkstra, "3D assessment of stent cell size and side branch access in intravascular optical coherence tomographic pullback runs," Comput Med Imaging Graph 38, 113-122 (2014).

Chapter

3

CHAPTER

4

3D assessment of stent cell size and side branch access in intravascular optical coherence tomographic pullback runs

ABSTRACT

We present a semi-automatic approach to assess the maximum circular unsupported surface area (MCUSA) of selected stent cells and the side branch access through stent cells in intravascular optical coherence tomography (IVOCT) pullback runs. Such 3D information may influence coronary interventions, stent design, blood flow analysis or prognostic evaluation. First, the stent struts are detected automatically and stent cells are reconstructed with users' assistance. Using cylinder fitting, a 2D approximation of the stent cell is generated for MCUSA detection and measurement. Next, a stent surface is reconstructed and stent-covered side branches are detected. Both the stent cell contours and side branch lumen contours are projected onto the stent surface to indicate their areas, and the overlapping regions are measured as the side branch access through these stent cells. The method was evaluated on phantom data sets and the accuracy of the MCUSA and side branch access was found to be 95% and 91% respectively. The usability of this approach for clinical research was proved on 12 in vivo IVOCT pullback runs.

4.1 Introduction

Over Coronary stents are widely used in the treatment of coronary artery disease. During a percutaneous coronary intervention (PCI), a stent is delivered to a stenosis and extended by inflating a balloon to keep it open. Clinical research has demonstrated that the support of an implanted stent to the vessel wall positively influences the outcome of the PCI [1-3]. Given these positive results, there is an increasing demand from clinical researchers for detailed stent analysis. However, the past research on the stent support mainly focused on the 2D stent struts distribution in cross-sectional images, such as the stent contour area, the number of visible struts and the inter-strut angle in a single frame [4-6]. Recently, 3D assessment like the size of every stent cell [7-9] has become popular for stent analysis. Stent cell size assessment may be used to evaluate the actual stent designs with respect to the struts distribution [10-12] or even the mechanism of controlled drug release from drug-eluting stents [13]. As a new desired feature, the maximum circular unsupported surface area (MCUSA) of stent cells was proposed to describe the support to the vessel wall [14;15]. It was defined as the maximal circular area that can be fit inside a 2D approximation of a stent cell.

Stents with smaller cells usually provide better support to the vessel wall, but when a stent covers a side branch, small stent cells in front of the side branch may lead to restenosis or obstruction of the blood flow to the side branch due to bridging [16-18]. If necessary, a stent cell in front of the side branch can be expanded by a second balloon to enlarge its ostium, but it may lead to stent fracture [19;20]. For interventional cardiologists, assessing the side branch access through stent cells may assist the PCI treatment prognosis of stent-covered side branches and the stent design evaluation.

To measure stent cells accurately, a precise description of the stent position is necessary. As a relatively new 3D optical imaging technique, intravascular optical coherence tomography (IVOCT) is increasingly being used to evaluate in-vivo coronary lesions [21;22]. It provides very high resolution (about 10 μm) cross-sectional images of coronary arteries so that the stent measurement can benefit from it. In IVOCT pullback runs, the implanted stents are visible as individual bright spots (struts) with a black shadow behind them [23;24]. Fig. 1 presents two in-vivo IVOCT images in Cartesian coordinate system and polar coordinate system separately.

In this paper, we present a semi-automatic approach to assess the MCUSA of every selected stent cell and the side branch access through stent cells. The details of the method are presented in section 2, while the validation method and the empirical results from a phantom data set and twelve in-vivo IVOCT pullback runs are presented in section 3 and section 4. The analysis of the results is given in section 5 and the conclusions and future work in section 6.

Chapter

4
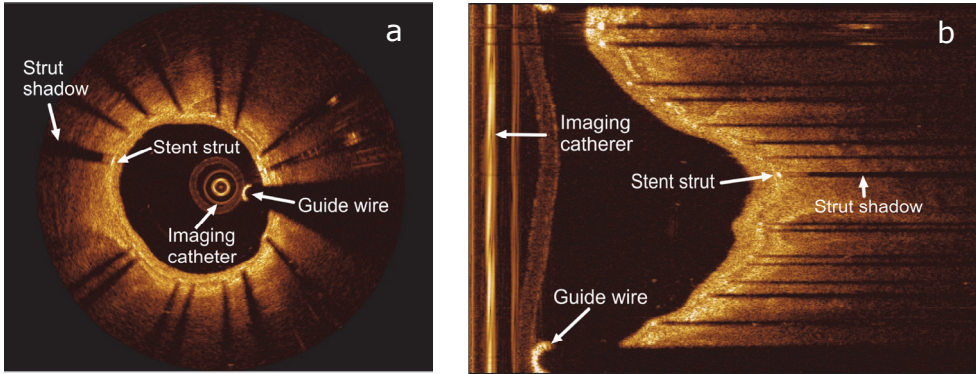
Figure 4-1. Two examples of in-vivo IVOCT images with an implanted stent. Figure (a) shows a Cartesian image, while figure (b) shows the corresponding polar image. In both images, a stent strut, the shadow behind this stent strut, the guide wire and the imaging catheter are annotated.

4.2 Methods

The presented methodology consists of six main steps: (1) automatic stent strut detection; (2) semi-automatic stent cell contour reconstruction; (3) 2D stent cell approximating and MCUSA assessment; (4) irregular stent surface reconstruction; (5) stent-covered side branch detection; (6) assessment of the side branch access through stent cells. A flow chart of the methodology is shown in Fig. 2. More details are given in the following sections.
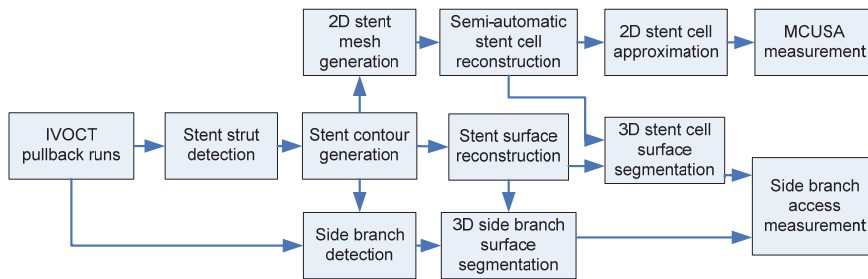
Figure 4-2. The flow chart of the presented method for MCUSA and side branch access measurement.

4.2.1 Stent strut detection

Before measuring the MCUSA and the side branch access, we need to reconstruct stent cells. The strut positions are needed because stents appear as struts in IVOCT pullback runs. Stent struts can be manually detected but it will be very time-consuming and lack of reproducibility. Several (semi-)automatic strut detection methods have been published [6;23-26]. In this manuscript, our recently published automatic stent strut detection method was used [23]. It segments the struts and the guide wire in polar IVOCT pullback runs automatically. This method was validated using almost 20000 struts under different conditions (malapposed, apposed and

covered) in 10 various quality in-vivo pullback runs, and the method has demonstrated that about 94% of the stent strut can be automatically detected.

4.2.2 Stent cell reconstruction

Without enough a-priori information, it is challenging to recognize a stent cell fully automatically, as different stents have different cell structures and their shapes can be distorted during the implantation. Additionally, if a stent cell in front of a side branch has been extended for better blood access, its shape and size will be greatly different from the other stent cells. Due to the irregular stent shapes and variable cell structures, automatic stent cell reconstruction methods may have limited performance. To come up with an accurate and maximally robust technique, we have decided for a semi-automatic stent cell reconstruction method, whereby users are requested to observe the stent cell pattern and confirm the struts belonging to a particular stent cell by manual interaction.

This means that the user needs to click on the struts belonging to a single stent cell in 2D space. Although users can observe stent cell structures in 3D space as Fig. 3(a) shows, these structures are not very clear due to the illusion of perspective projection. Besides, it is difficult for user to click struts in 3D space. To simplify the user observation and interaction, the stent is cut up along the longitudinal direction and opened as a 2D mesh. To do this, the stent contour center in each frame is required as the first step. As shown in Fig. 1 (a), the cross section of the implanted stent is elliptical, so it is reasonable to fit an ellipse to the stent struts as the approximation of the stent contour. Here, a least-square method [27] is chosen to fit the ellipse. In some frames, there are not enough struts for an accurate ellipse fitting result. Under such circumstances, struts from neighboring frames are projected to the current frame for ellipse fitting as well, because the stent contour position does not change much between two neighboring frames. In case there are still not enough stent struts available (typically < 6), the stent contour in this frame will be linearly interpolated from the neighboring stent contours. The fitted ellipses are first used to remove the outliers from the struts detected in section 2.1. All the struts are checked by computing their distance to the elliptic stent contour. If a strut is located too far away from the ellipse, it will not be used for the stent surface reconstruction.

After the elliptical stent contours are fitted, an imaginary cylinder is created along the centerline of the pullback run with the diameter being the average length of all ellipse axes. The struts in the individual frames are shifted until the stent center overlays the original Cartesian image center. Next, all the stent struts are projected onto this cylinder along a ray shot from the image center; Fig. 3 (b) shows an example of a projection result. This step guarantees that there will be no overlaid struts during the projection. When the cylinder is opened into 2D, the stent is converted to a 2D mesh (Fig. 3 (d)). This 2D mesh is only used to simplify the users' observation and interaction, but not for stent cell size measurement; for this reason, a mapping is kept between the 2D struts and the original 3D struts. Later in section 2.6, the detected side branch lumens are also projected onto this imaginary cylinder and opened together with the stent, so that the stent cells which may be in front of side branches could be detected easily as Fig. 3 (d) shows.

Users are requested to observe and recognize stent cells in the 2D mesh, and then click on the struts belonging to a stent cell in the proper order. When a strut is indicated in the 2D mesh, the corresponding original 3D strut position is found based

Chapter

4

on the known mapping between 2D and 3D struts. The time required for this interactive process depends on the stent structure complexity and the number of struts. Typically, it takes about 15 seconds to indicate all the struts belonging to a stent cell. Next, the stent cell contour is generated by linking the 3D struts in the proper order using a natural-spline. An example of a reconstructed stent cell contour is presented in Fig. 3(e).
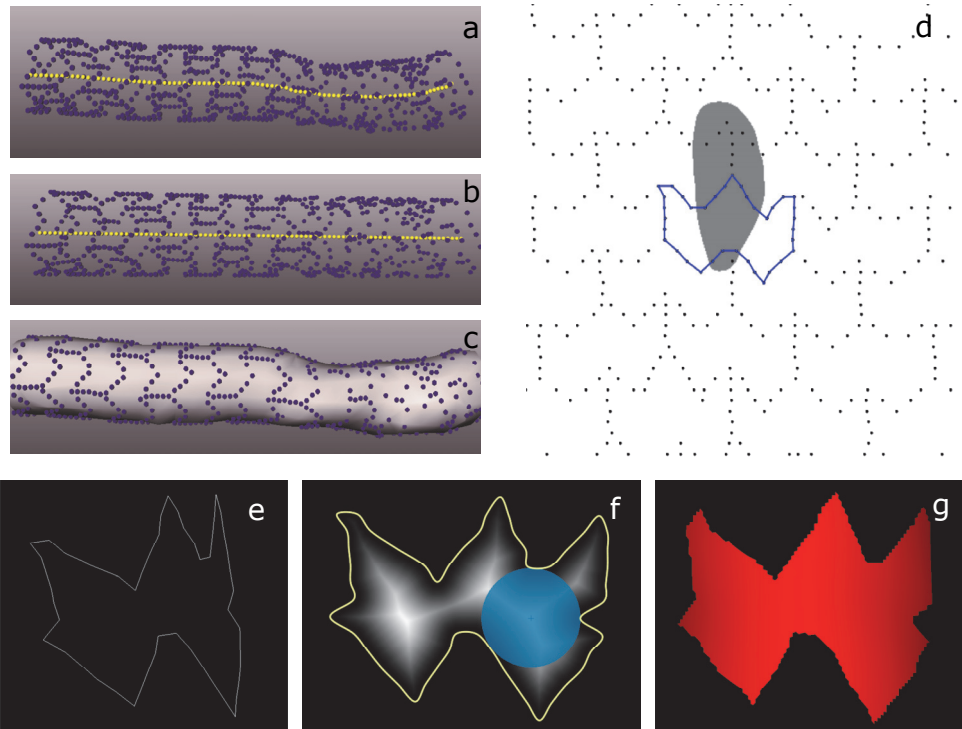
Figure 4-3. (a) Elliptic stent contours are fitted to the original stent struts (blue dots) from an in-vivo IVOCT pullback run. Based on the ellipse centers (yellow dots), (b) struts are shifted and projected onto a cylinder. (c) An irregular stent surface is reconstructed from the original struts. (d) The stent is opened into 2D and the struts are presented as black dots, while a user detected stent cell is presented in blue. Similarly, a side branch lumen (gray area) is also projected onto the cylinder and opened to show its relative location with respect to the stent cells. (e) A 3D stent cell is reconstructed according to the 2D/3D struts mapping. The cell contour is generated by linking struts with a natural spline. (f) A 2D approximation of the stent cell is given and the grey value inside the contour is the distance transform result. Its MCUSA (the blue circular area) is detected by searching for the highest intensity pixel in it. (g) The cell contour is projected onto the stent surface to determine the cell surface for the further side branch access assessment.

4.2.3 MCUSA estimation

The MCUSA of a stent cell is the maximum circular area inside this stent cell. As a 3D structure, every stent cell needs a 2D approximation to compute its MCUSA. This

approximation should preserve the main stent cell size and shape details. It can be generated by fitting a regular shape to the stent cell and opening into 2D. In the case of a stent, the logical choice for the regular shape is a cylinder. Fitting the whole stent to a single cylinder could introduce errors, because stents are bended and distorted during the implantation procedure e.g. at side branches (Fig. 3 (a)). In order to minimize the introduced errors, a cylinder side surface is fitted to only the struts belonging to a single stent cell instead of all the struts. The fitting is based on a least-squares cylinder fitting method [28], which minimizes the error between struts and the fitted cylinder side surface. The initial orientation of the cylinder is set as the longitudinal direction of the pullback run and the initial radius is the average length of the stent ellipse axes. After the cylinder fitting, the stent struts are projected onto the fitted cylinder and opened into 2D. Struts are linked by a natural spline as Fig. 3 (f) shows. Before opening, a connectivity check is applied to make sure that stent cell cannot be split into two halves. If a stent cell could be split, the opening position of the cylinder will be rotated to the outside of the stent cells.

The largest circle which can be found inside this 2D approximation is the MCUSA. The center of the MCUSA is the point which has the maximum shortest distance to its surrounding boundary. To detect this point, first a binary image is generated from the 2D approximation. Next, the distance transform algorithm [29] is applied to this binary image. In the resulting image, the pixel with the highest intensity defines the center of the MCUSA and its intensity value is the radius of the MCUSA. An example is given in Fig. 3 (f). Please note that although there may be more than one maximum circle, they all have the same size.

4.2.4 Stent surface reconstruction

As Fig. 5 (a) presents, the side branch access through a stent cell can be measured by computing the overlaid region between the side branch and the stent cell. To achieve the common region between them, we need to reconstruct a precise stent surface for the implanted stent. The stent cell surface and the side branch lumen surface will be segmented on the stent surface. During the stent extension, the balloon cannot evenly expand in all areas because the hardness of tissue and plaques is different. Therefore, the shape of the implanted stents is irregular in general. In our approach, a precise and piecewise smooth stent surface is reconstructed from the detected stent struts using Hoppe's method[30]. The surface consists of many tiny triangles. This method requires a group of relatively evenly distributed points and has two parameters: the neighborhood size and the sample spacing. The first parameter is the average neighbor number of each strut which is used to estimating the local surface orientation. Here, it depends on the average number of struts in each frame. The second parameter is used to specify the spacing of the 3D sampling grid. An example of the reconstructed stent surface is shown in Fig. 3 (c).

If a guide wire is used during the IVOCT image acquisition, it blocks all the information behind it including stent struts. Missing struts due to the guide wire shadow will cause breaches and distortion on the reconstructed stent surface. To solve this problem, imaginary struts are added behind the guide wire on the elliptical stent contours. Different locations of the imaging catheter and the guide wire result in different size of guide wire shadows. To estimate the possible number of blocked struts, we deduce the angle of the blocked arcs based on the guide wire shadow edges detected in section 2.1. On the covered ellipse arc, an imaginary strut is added every 30

degrees. A special mark is given to these imaginary struts, because they will be only used for the stent surface reconstruction, but not for stent cell reconstruction.

4.2.5 Side branch detection

To measure the side branch access through stent cells, the stent-covered side branches need to be detected. In IVOCT pullback runs, a side branch appears like a black lacuna on the main vessel lumen. Therefore, it can be detected by checking the distance changing from the lumen center to the lumen boundary. If the distance profile shows a sharp increase in a certain region, it could indicate the presence of a side branch. Because the centers of Cartesian IVOCT images represent the imaging catheter positions but not the lumen centers, the lumen centers have to be detected first. In the typical situation where a stent is well extended to support the vessel wall, the stent contour center can be treated as an approximation of the lumen center. In this research, only the side branches which are covered by apposed or covered stents are analyzed, therefore, the ellipse centers from section 2.2 were used.

As demonstrated in Fig. 4 (a), the image catheter and the guide wire are present between the lumen center and the lumen boundary. Before the distance is computed, these bright regions have to be masked out. During the IVOCT imaging acquisition, the imaging catheter generates bright vertical lines in the polar images. With a proper z-offset correction, the artifacts are located in the same position during the whole pullback run. Therefore, these are detected by applying a dynamic programing algorithm to the whole pullback run in the longitudinal direction and later masked out. The guide wire has been detected during the strut detection [23], so they are masked out as well. After masking, the polar IVOCT images are converted into Cartesian images and a median filtering is applied followed by a Gaussian smoothing to smooth the bright tissue region. To specify the lumen region, images are converted into binary images by thresholding the intensity values. The threshold is computed based on the histogram of the whole image. An example of a binary image is presented in Fig. 4 (b).

The distance from the center to the lumen boundary is measured every half degree and Fig. 4 (c) shows the distance profile of a single frame. The side branches and the guide wire result in the two peaks with sharp increasing and decreasing in the profile. As the automatic stent strut detection also detects guide wire besides the stent struts [23], peaks resulting from guide wire will be ignored. After removing the guide wire peaks, the highest peaks in the profile indicate the possible side branch positions. Four main rules are used to identify a side branch: 1) the distance is longer than the median value of all the distances in each frame; 2) this region starts and ends with significant distance changes; 3) the width of this region is at least 30 degrees; and 4) a candidate side branch should have a reasonable size in the longitudinal direction. If a candidate side branch is found, its start and end points will be detected by computing the biggest changes of the distance. Next, the start and the end of each side branch are marked out as Fig. 5 (b) shows. The side branch lumen contour is generated by linking these starts and ends with a natural spline. We also noticed that in a few cases, the struts in front of a side branch were covered by tissue composing a bridge over the side branch. In these cases, a manual correction could be needed.
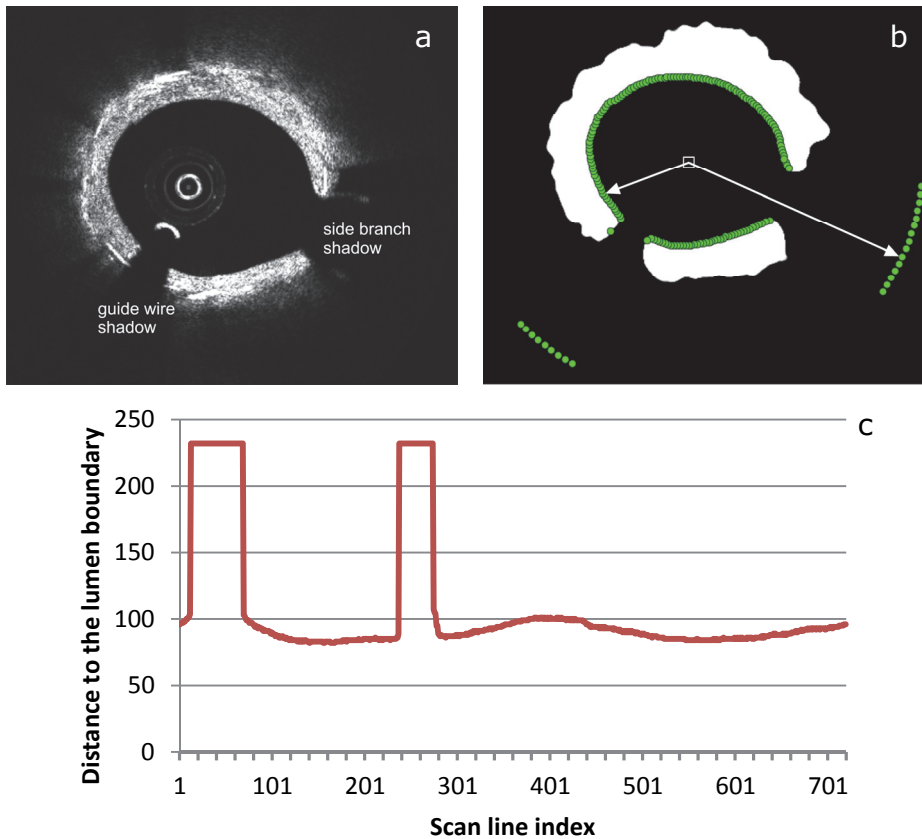
Figure 4-4. (a) presents an in-vivo IVOCT image with a side branch and a guide wire. After processing, the image result is shown in figure (b). From the fitted ellipse center (the small white square in the middle), the distance to the lumen contour is computer over all 360 degrees. The scan-line ends at the lumen contour or the image edge with green dots. The profile of this distance is presented in figure (c). There are two peaks in the profile which represent the side branch and the guide wire respectively.

4.2.6 Side branch access measurement

In this paper, the side branch access through a stent cell is defined by the ostium which is generated by the stent cell above the side branch. As Fig. 5 (a) presents, the side branch access through a stent cell is measured by computing the overlaid region between stent cells and side branches. Since the stent surface has been reconstructed, both stent cell areas and side branch areas can be segmented on it.

Here, the stent cell contour is used for this segmentation. Because the stent cell contour is generated by linking struts using a natural spline, the interpolated part may not be exactly located on the stent surface. For accuracy, the cell contours are projected onto the stent surface to segment the 3D stent cell surfaces. As the stent cell contours are almost located on the stent surface, a simple linear extrusion is used for performance issues. The cell contour is extruded toward to the stent center; thereby

generating a hollow object which intersects with the stent surface as Fig. 5 (d) shows. The contour extrusion direction and length is set by a vector which is orthogonal to the centerline of the stent and passes through the center of the bounding box of the stent cell. The collision part is segmented from the stent surface resulting in the 3D cell surface as Fig.3 (g) shows. This cell surface comprises many small triangles and its size is the sum of the areas of these triangles.
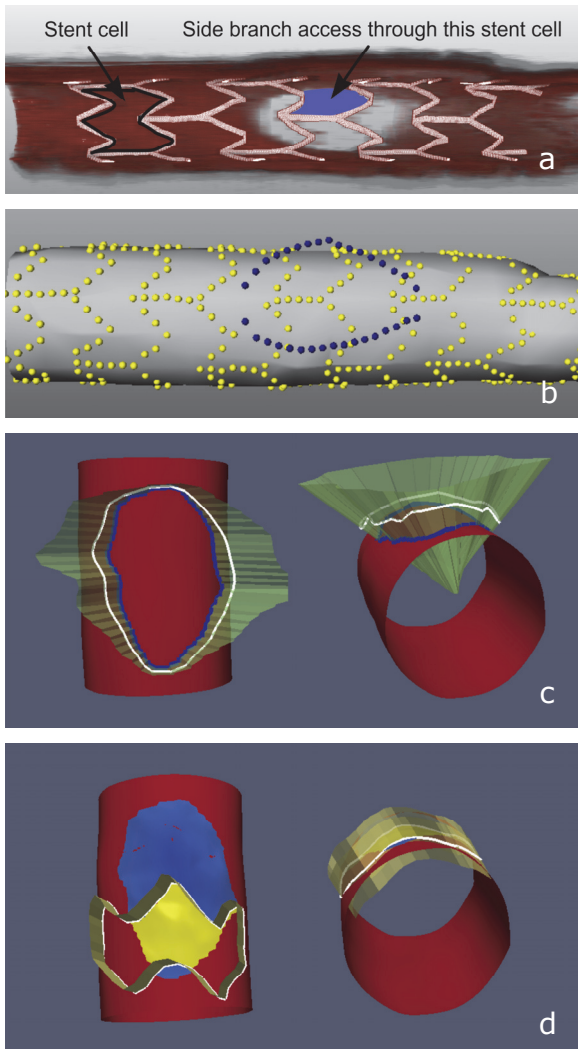
Figure 4-5. (a) A stent covers a side branch. The black contour indicates a stent cell. The side branch appears as a hole on the red vessel wall. The blue area shows the side branch access through a stent cell. (b) shows the struts (yellow dots), the side branch lumen contour (delineated by blue dots) and the fitted stent surface (light grey). (c) The 3D side branch lumen contour (white) is located far away from the stent surface (red), and the blue contour is the projection result. (d) The stent cell contour (white) is almost located on the stent surface. The linear extrusion of the contour (green) generates the contour projection (white) to segment the access area (yellow) on the side branch lumen surface (blue).

Stent cell structures are easily observed in the 2D stent mesh. If the stent-covered side branch lumen is shown together with the 2D mesh, the stent cells that may be in front of this side branch can easily be detected. This could speed up the manual interaction. To do this, the side branch contour is projected onto the same imaginary cylinder for stent cell contour detection in section 2.2 and opened into 2D as Fig. 3 (d) shows. The side branch lumen contour is projected onto the stent surface to segment the side branch lumen area. Unlike stent cell contour projection, side branch lumen

contours usually are located further away from the stent surface as Fig. 5 (b). If they are extruded linearly, the results will contain large errors. Therefore, an accurate projection method is used for side branches. Since the side branch contour surrounds the cylindrical stent surface, each point on the side branch contour should be projected toward to the lumen center. Practically, each point on the lumen contour shoots a ray to the lumen center in the same longitudinal position. The intersected points between the rays and the stent surface are linked using a natural spline to segment the side branch lumen surface. An example is shown in Fig. 5 (c). As the stent cell surfaces and the side branch lumen surfaces are all segmented from the stent surface, the overlaid part between a stent cell surface and a side branch lumen surface represents the side branch access through this stent cell. An example is given in Fig. 5 (d).

4.3 Validation method

For in-vivo stents, the ground truth of their stent cell size and the side branch access through stent cells are not available. Because first, the implanted stents cannot be removed from the patients, and second, the irregular stent surface is not suitable for validation, because it is almost impossible to achieve its ground truth. To validate the new presented methods, a phantom data set was created by scanning a 3.0 mm × 8.0 mm coronary stent using Micro CT. As Fig. 6 (a) shows, in the CT data set, the stent is visible as struts similar in IVOCT pullback runs. Besides, although Micro CT can scan only small objects, it provides a higher resolution than IVOCT (30 times higher than IVOCT in the longitudinal direction). The phantom size is 1024 pixels × 1024 pixels × 1240 frames with a voxel size of 5.86 μm × 5.86 μm × 6.62 μm. Therefore, Micro CT data sets were used for the presented method validation and the stent cell contours generated from the phantom data set are accurate enough to be treated as the ground truth, as Fig. 6 (b) presents. Without any resistance from the vessel wall, the stent was extended evenly and can thus be treated as a cylinder. Although this is not the situation for a real stent inside a patient, it allows us to validate the method itself without potential measuring errors resulting from an irregular stent surface. By projecting the stent cell contours onto the stent cylinder, the ground truth of the stent cell size can be estimated.

The extended stent was found to be 3.1 mm × 8.2 mm; therefore it was represented by a cylinder of the same size. All the struts in the phantom data set were detected and the stent cells were reconstructed. Next, every stent cell contour was projected onto the cylinder and opened into 2D. The size of these opened stent cell surfaces were recorded as the ground truth of the stent cell surface size. At the same time, the ground truth of the MCUSA of every stent cell was computed as well. Since the phantom data set contains no side branches, four ellipses were generated as virtual side branches outside the stent cylinder surface. Each ellipse has a different position and orientation. Side branch surfaces were segmented by projecting all the ellipses onto the stent cylinder and opened into 2D as Fig. 7 (a) shows. Compared with the stent cell surfaces, the ground truth of the side branch access through stent cells can be measured by the common areas (Fig. 7 (b)).

To evaluate the accuracy of the proposed method, the stent should be scanned in a phantom by an IVOCT system and a Micro CT system. However, we did not have a proper phantom which was both IVOCT and micro-CT compliant. Therefore, the CT data set was resampled to simulate the in-vivo IVOCT data set. In our in-vivo IVOCT

pullback runs, the voxel size is 6.85 μm × 6.85 μm × 200 μm. Therefore, the original phantom data set was re-sampled by selecting 1 frame out of every 30 frames, resulting in the similar resolution as IVOCT pullback runs (5.86 μm × 5.86 μm × 200 μm) as Fig. 6 (c) shows. The re-sampled phantom data set was processed by the presented approach and the results were compared with the ground truth for validation. Besides, the accuracies of 2D stent cell approximations and stent cell surfaces segmented from stent surface were also validated as essential pre-steps.
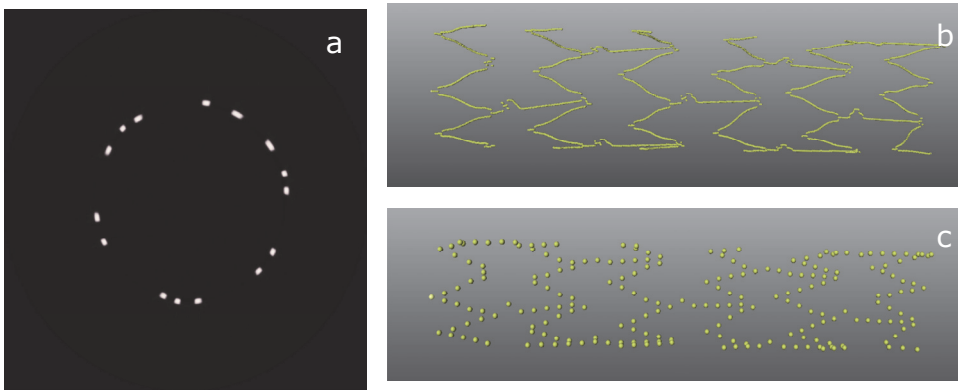
Figure 4-6. (a) a single Micro CT frame with stent struts (white points), which looks similar to clinical IVOCT images. In both figures, the stent struts appear as bright spots. (b) half of the struts detected in the original phantom data set and (c) half of the struts detected in the re-sampled phantom data set. There are much more struts in the original phantom data set than the re-sampled data set and its cell contour can be treated as the ground truth.
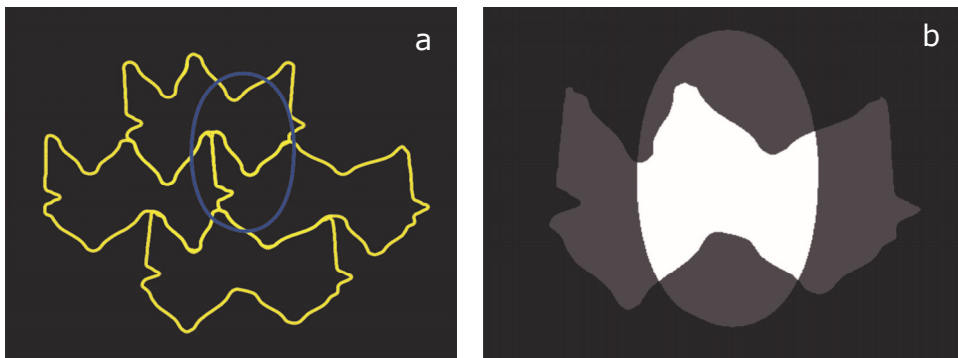
Figure 4-7. (a) The opened 2D stent cells (yellow) in the original phantom data set and an opened imaginary side branch lumen (blue). (b) An example of a side branch access through the stent cell from the original phantom data set. The brightest region in the image is the side branch access to the main vessel through this stent cell.

To examine the usability of this approach on clinical data sets, a total of 12 randomly selected IVOCT pullback runs from a one-year follow up study were used. They were acquired with a C7-XR OCT intravascular imaging system (LightLab, Westford, MA, USA). Their resolution is 6.85 μm × 6.85 μm × 200 μm. Ten pullback runs contained 271 frames using a pullback speed of 20 mm/s, while the other two contained 541 frames with speed of 10 mm/s. Nine data sets were acquired with a guide wire, while the others contain no guide wire. All the stents were drug-eluting stents, except for one bioresorbable vascular scaffold (BVS). They contained a total of 726 recognizable stent cells and 27 side branches were located in the stented regions. Because of the IVOCT image quality and guide wire shadows, not all of the stent cells and side branches could be measured. From the measureable stent cells, we randomly selected 105 stent cells for subsequent testing. The 3D stent cell surface and the corresponding 2D stent cell approximation should have similar size. Some of the stent cells in front of the side branch had been extended, so we also checked whether their full cell size and the MCUSA are reasonable bigger than the other stent cells. For stent-covered side branches, extended stent cells should offer a bigger access than unextended stent cells. Therefore, the average percentage of the biggest side branch access through stent cells was computed.

As Figure 3 (d) shows, the stent cells in the 2D mesh are very clearly visible, so we expected the stent cell results from different experts to be the same. Therefore, the assessment of the inter/intra-operator variability is not considered in this research. One trained expert selected and reconstructed all the stent cell contours and side branch lumen contours as the ground truth.

4.4 Results

Table 1 presents the full stent cell size and the MCUSA size results from both original and re-sampled phantom data sets. For 12 in-vivo IVOCT pullback runs, the results are given in Table 2. Comparisons of the 3D stent cell surface and the 2D stent cell approximation in both original and re-sampled phantom data sets are shown in Figure 8.

The side branch access measurement results in all original CT data set, re-sampled CT data set and in-vivo IVOCT data sets are given in Table 3. According to the results, the average size of side branches was 1.2 ± 0.8 mm^2, and each side branch was covered by 1.7 ± 0.8 stent cells. The average side branch access through each stent cell was 0.7 ± 0.5 mm^2. Fifteen of the side branches were covered by only one stent cell, so no stent wire would block their entrances. Eight of the side branches were covered by two stent cells. Three side branches were covered by three stent cells and one by six stent cells.

The automatic strut detection method was developed using the MeVisLab toolbox 2.2 (MeVis Medical Solutions AG, Bremen, Germany) and VTK toolkit 5.10 (www.vtk.org) together with in-house developed C++ modules. For processing, we used Windows 7 Professional x64 Edition with a 2.0 GHz CPU and 4 GB of memory. Generally, it takes less than 1 minute to detect all the stent struts in a pullback run of 271 frames. The semi-automatic stent cell reconstruction costs about 10 seconds for every stent cell, while the other processing usually takes about 1 minute. If implemented using pure C++ code, the computing time could be further shortened. The whole processing time depends on the length of the stent and how many stent cells need to be measured.

Chapter

4

Table 1. The maximum, minimum, mean value (with standard deviation) and the sum of the stent cell size from both original and re-sampled phantom data set. The stent cell size and MCUSA from the original phantom data set are treated as the ground truth, so that the errors for the 3D stent cell surface, 2D stent cell approximation and MCUSA from the re-sampled data set can be computed.

Data set	Feature	Max (mm²)	Min (mm²)	Mean ± SD (mm²)	Sum (mm²)	Error (%)
Original Phantom data set (ground truth)	Full stent cell size	5.74	3.96	4.75 ± 0.44	71.27	--
	MCUSA	1.70	0.95	1.29 ± 0.22	19.28	--
Re-sampled Phantom data set (algorithmic results)	Stent cell surface	5.64	3.97	4.72 ± 0.44	70.77	0.96 ± 0.64
	2D approximation	5.74	3.99	4.79 ± 0.45	71.90	0.98 ± 0.74
	MCUSA	1.70	0.87	1.25 ± 0.22	18.76	5.0 ± 5.2

Table 2. The maximum, minimum, mean value (with standard deviation) and the sum of the stent cell surface size, 2D stent cell approximation size and MCUSA size in 12 in-vivo IVOCT data sets.

Data set	Feature	Max (mm²)	Min (mm²)	Mean ± SD (mm²)	Sum (mm²)
In-vivo IVOCT pullback runs	Stent cell surface	10.04	1.00	3.01 ± 1.39	328.06
	2D approximation	9.55	1.07	3.10 ± 1.34	337.38
	MCUSA	1.40	0.25	0.96 ± 0.80	104.21

Table 3. The maximum, minimum and mean size (with standard deviation) of the side branch access from the original and re-sampled phantom data sets and in-vivo IVOCT data sets. The sum of the side branch access equal to the sum of side branch lumen areas. The amount of side branches and the stent cells in front of side branches and the percentage of the average maximum side branch access comparing to the average side branch lumen in every group are also given.

Data set	Max (mm²)	Min (mm²)	Mean (mm²)	Sum (mm²)	Side branch amount	Cell amount	Max access (%)
Original phantom	2.30	0.23	0.86 ± 0.86	12.83	4	21	53.69
Re-sampled phantom	2.39	0.26	0.89 ± 0.88	13.46	4	21	53.31
In-vivo IVOCT data sets	4.21	0.22	0.68 ± 0.49	31.06	27	46	77.59
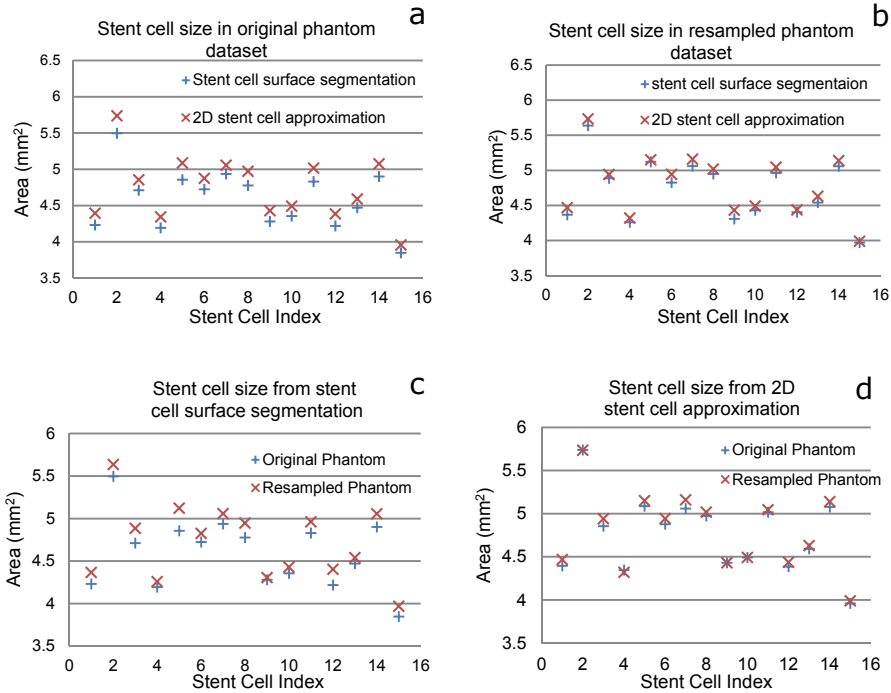
Figure 4-8. (a) shows the results of 3D stent cell surface and 2D stent cell approximation in the original phantom data set, while (b) shows these results from the re-sampled phantom data set. (c) indicates the results of 3D stent cell surface in both original and re-sampled phantom data sets, while chart (d) compares the corresponding size of 2D stent cell approximation in both original and re-sampled phantom data sets.

4.5 Discussion

To validate the accuracy of the presented approach, the relative errors of our algorithmic results were computed. The mean and the standard deviation of the relative errors were determined to demonstrate the performance. Table 1 shows that the ground truth of the whole stent surface area is 71.27 mm^2 and the sum of the MCUSA is 19.28 mm^2. In the re-sampled phantom data set, the estimated stent surface size is 70.77 mm^2 from the summation of 3D stent cell surfaces and 71.90 mm^2 from the summation of 2D stent cell approximations, while the summation of the MCUSA is 18.76 mm^2. Compared to the ground truth, the average error of the every 3D stent cell surface is 0.96 ± 0.64%, while that of the 2D stent cell approximation is 0.98 ± 0.74% and the MCUSA error is 5.0 ± 5.2%. In the re-sampled phantom data sets, the 3D stent cell surface and 2D stent cell approximation results are almost the same as the ground truth like Fig. 8 (a) and (b) show. It suggests that our approach is very accurate when measuring the stent cell size within the resolution of in-vivo IVOCT pullback runs. Fig. 8 (c) and (d) demonstrate that the stent cell surface size is usually a little bit smaller

than the 2D stent cell approximation size. A possible explanation is that the stent cell surface is segmented from the reconstructed stent surface that consists of thousands of small triangles, while the 2D stent cell approximation calculates the stent cell using the opened surface from the fitted cylinder. For a curved surface, the opened surface should be bigger than the surface that is approximated with triangle polygons.

Table 2 shows the quantitative analysis results of 105 stent cells from 12 clinical IVOCT pullback runs. The mean difference between the 3D stent cell surfaces and 2D approximations is 4.2 ± 2.3%. Since the distributed stent struts do not fit to any regular shape in 3D space, we could not obtain the ground truth of in-vivo stent cell areas. However, our methods provide an intuitive approximate measurement of the stent cell size in clinical data sets.

According to Table 3, the experimental results of the side branch access through stent cells in both original and re-sampled phantom data sets indicate that the average error of the algorithmic results is 8.9 ± 7.0%. For the in-vivo IVOCT pullback runs, more than 60% of the side branches have more than one stent cell ostia. On average, the largest ostium includes more than 77.6% of the side branch lumen area, and the sum of the largest two ostia includes 92.6% of the lumen area. By contrast, the numbers in the phantom data set with un-extended cells are smaller as 53.1% and 75.9%. The experimental results clearly show that, in most of our in-vivo cases, the stents cells in front of side branches have been extended so that side branches are less covered. The only exception is the BVS stent, because compared to bare metal and drug-eluting stents, BVS stents are less flexible and can break easier. Consequently, in the BVS data set, one side branch is covered by 6 stent cells while another side branch has 3 stent cells and none of the stent cells are extended.

IVOCT image sequences provide the longitude image data of the implanted stent along the imaging catheter. In practice, the imaging catheter may be curved. Without the 3D tracking of the imaging catheter, the cell area in IVOCT data may contain an error when the imaging catheter bends. However, in most cases, the trajectory of the imaging catheter has only very smooth curvatures so that the error for distortion is limited. Therefore, this method is expected to give a good approximation of the stent cell area. This method requires only stent strut positions for stent surface reconstruction and stent cell indication. Therefore, it is available for any type of bare metal stents, drug-eluting stents or BVS stents. With provided struts and side branches information, it can compute the MCUSA and side branch access for any stents.

If a side branch is fully or partly covered by the guide wire shadow or a bridge, this side branch will not be detected or measured, since its contour is incomplete. The same situation could happen for stent cells and these cells cannot be indicated or measured as well. Imaginary struts can be added to assist the stent surface reconstruction, but if more than half of the stent is covered or unclear, the reconstructed stent surface is less reliable for assessment. In most of our cases, guide wire shadow regions cover less than a quarter of the stent contour and the imaginary struts are concentrated only in the shadow region. Hence the reconstructed stent surface can be separated as real surface part and imaginary surface part. Imaginary part will not affect the shape of the real surface part and the measurement is applied only on the real surface part. The presented side branch detection method could fail if the lumen contour appears like a highly narrowed ellipse, because the distal lumen can be missed due to the limited penetration (< 2 mm) of IVOCT [23]. In these special cases, a manual correction is requested.

The side branch projection should follow the angle between the side branch and the main vessel. However, due to the limited penetration of IVOCT, the angle of the side branch cannot be measured. Therefore, in the presented method, the projection direction is always vertical to the center-line of the stent. For stent cell contours and side branch contours, we chose different projection methods. Theoretically, the projection method for side branches should be the optimal way. However, the projection of stent cells will introduce only tiny error but is much time efficient. The stent cell surface results are accurate enough and the computing is easy and fast.

During the IVOCT acquisition, some artifacts may arise as results of many different reasons. Some artifacts like residual blood noise [31] and the sun-flower artifact [23] were mostly removed during our processing, while many artifacts were not taken into account in this research, such as non-uniform rotational distortion (NURD) [32], because the new frequency-domain IVOCT system has a very fast speed to reduce these artifacts.

4.6 Conclusion and future work

With its high resolution, IVOCT allows a better understanding of the stent structures in the coronary arteries. We have presented an approach to measure the stent support degree and the side branch access in IVOCT pullback runs. It detects stent struts, reconstructs stent cells, generates 2D stent cell approximations, detects stent-covered side branches and reconstructs the irregular stent surface for MCUSA and side branch access assessment. A full resolution phantom data set and its re-sampled data set were used to evaluate the feasibility and the accuracy of this approach. Next, it was applied to twelve in-vivo IVOCT data sets. Quantitative evaluation reveals that the approach has achieved high accuracy for the MCUSA and side branch access measurement. The results suggest that this method can be a useful tool for the stent implantation improvement, stent design evaluation, blood flow analysis and computer-guided diagnosis. There are still artifacts that may affect the results of the presented method, and we will work on that in future.

Chapter

4

4.7 References

1. Bosiers M, de Donato G, Deloose K, Verbist J, Peeters P, Castriota F, et al. Does free cell area influence the outcome in carotid artery stenting? European Journal of Vascular and Endovascular Surgery 2007;33(2):135-141.

2. Tanigawa J, Barlis P, Dimopoulos K, Dalby M, Moore P, Di Mario C. The influence of strut thickness and cell design on immediate apposition of drug-eluting stents assessed by optical coherence tomography. International Journal of Cardiology 2009;134(2):180-188.

3. Takebayashi H, Mintz GS, Carlier SG, Kobayashi Y, Fujii K, Yasuda T, et al. Nonuniform strut distribution correlates with more neointimal hyperplasia after sirolimus-eluting stent implantation. Circulation 2004;110(22):3430-3434.

4. Mejia J, Ruzzeh B, Mongrain R, Leask R, Bertrand OF. Evaluation of the effect of stent strut profile on shear stress distribution using statistical moments. Biomedical Engineering Online 2009;8.

5. Trivisonno A, Musumeci G, Sirbu V, Lortkipanidze N, Matiashvili A, Mihalcsik L, et al. Strut Number and Distribution: Implications for Drug-Eluting Stent Coverage and Neointimal Growth. In-vivo Insight from Optical Coherence Tomography. American Journal of Cardiology 2008;102(8A):145I.

6. Unal G, Gurmeric S, Carlier SG. Stent implant follow-up in intravascular optical coherence tomography images. International Journal of Cardiovascular Imaging 2010;26(7):809-816.

7. Capelli C, Gervaso F, Petrini L, Dubini G, Migliavacca F. Assessment of tissue prolapse after balloon-expandable stenting: Influence of stent cell geometry. Medical Engineering & Physics 2009;31(4):441-447.

8. Conti M, Van Loo D, Auricchio F, De Beule M, De Santis G, Verhegghe B, et al. Impact of Carotid Stent Cell Design on Vessel Scaffolding: A Case Study Comparing Experimental Investigation and Numerical Simulations. Journal of Endovascular Therapy 2011;18(3):397-406.

9. Cremonesi A, Setacci C, Castriota F, Valgimigli M. Carotid stent cell design: Lack of benefit or lack of evidence? Stroke 2008;39(8):E130.

10. Okamura T, Garg S, Gutierrez-Chico JL, Shin ES, Onuma Y, Garcia-Garcia HM, et al. In vivo evaluation of stent strut distribution patterns in the bioabsorbable everolimus-eluting device: an OCT ad hoc analysis of the revision 1.0 and revision 1.1 stent design in the ABSORB clinical trial. Eurointervention 2010;5(8):932-938.

11. Lee JB, Kim KS, Kim SY, Lee YS, Ryu J, Choi JY, et al. Comparison of nonuniform strut distribution among three drug-eluting stent platforms. American Journal of Cardiology 2008;101(8B):72C.

12. Suzuki Y, Ikeno F, Yeung A. Drug-Eluting Stents strut distribution; A comparison of 3 stent designs by optical coherence tomography. American Journal of Cardiology 2005;96(7A):182H.

13. O'Brien CC, Finch CH, Barber TJ, Martens P, Simmons A. Analysis of Drug Distribution from a Simulated Drug-Eluting Stent Strut Using an In Vitro Framework. Annals of Biomedical Engineering 2012;40(12):2687-2696.

14. Onuma Y, Serruys PW. Bioresorbable Scaffold The Advent of a New Era in Percutaneous Coronary and Peripheral Revascularization? Circulation 2011;123(7):779-797.

15. Gomez-Lara J, Brugaletta S, Diletti R, Garg S, Onuma Y, Gogas BD, et al. A comparative assessment by optical coherence tomography of the performance of the first and second generation of the everolimus-eluting bioresorbable vascular scaffolds. European Heart Journal 2011;32(3):294-304.

16. Ruffino MA, Rabbia C. Endovascular Repair of Peripheral and Visceral Aneurysms With the Cardiatis Multilayer Flow Modulator: One-Year Results From the Italian Multicenter Registry. Journal of Endovascular Therapy 2012;19(5):599-610.

17. Mortier P, De Beule M, Van Loo D, Verhegghe B, Verdonck P. Finite element analysis of side branch access during bifurcation stenting. Medical Engineering & Physics 2009;31(4):434-440.

18. Rizik DG, Hermiller JB, Klassen KJ, Shah M. Xience Side Branch Access Stent for Treatment of Bifurcation Coronary Disease: A Review of Preclinical Data. Journal of Interventional Cardiology 2012;25(4):337-343.

19. Kurisu S, Mitsuba N, Kato Y, Ishibashi K, Dohi Y, Nishioka K, et al. External Side-Compression of Radial Artery: A Simple Technique for Successful Advancement of Guidewires through the Radial Approach. Journal of Interventional Cardiology 2011;24(5):397-400.

20. Burzotta F, De Vita M, Sgueglia G, Todaro D, Trani C. How to solve difficult side branch access? Eurointervention 2010;6:J72-J80.

21. Abtahian F, Jang IK. Optical coherence tomography: basics, current application and future potential. Current Opinion in Pharmacology 2012;12(5):583-591.

22. Hamdan R, Gonzalez RG, Ghostine S, Caussin C. Optical coherence tomography: From physical principles to clinical applications. Archives of Cardiovascular Diseases 2012;105(10):529-534.

23. Wang A, Eggermont J, Dekker N, Garcia-Garcia HM, Pawar R, Reiber JH, et al. Automatic stent strut detection in intravascular optical coherence tomographic pullback runs. Int J Cardiovasc Imaging 2013;29(1):29-38.

24. Tsantis S, Kagadis GC, Katsanos K, Karnabatidis D, Bourantas G, Nikiforidis GC. Automatic vessel lumen segmentation and stent strut detection in intravascular optical coherence tomography. Med Phys 2012;39(1):503-513.

25. Mandelias K, Tsantis S, Karnabatidis D, Katsakiori P, Mihailidis D, Nikiforidis G, et al. Fast and Robust Algorithm Towards Vessel Lumen and Stent Strut Detection in Optical Coherence Tomography. Medical Physics 2012;39(6):3645-3646.

26. Gurmeric S, Isguder GG, Carlier S, Unal G. A new 3-D automated computational method to evaluate in-stent neointimal hyperplasia in in-vivo intravascular optical coherence tomography pullbacks. Med Image Comput Comput Assist Interv 2009;12(Pt 2):776-785.

27. Fitzgibbon A, Pilu M, Fisher RB. Direct least square fitting of ellipses. Ieee Transactions on Pattern Analysis and Machine Intelligence 1999;21(5):476-480.

Chapter

4

CHAPTER

5

Fully automated side branch detection in intravascular optical coherence tomography pullback runs

ABSTRACT

Side branches in the atherosclerotic lesion region are important as they highly influence the treatment strategy selection and optimization. Moreover, they are reliable landmarks for image registration. By providing high resolution delineation of coronary morphology, intravascular optical coherence tomography (IVOCT) has been increasingly used for side branch analysis. This paper presents a fully automated method to detect side branches in IVOCT images, which relies on precise segmentation of the imaging catheter, the protective sheath, the guide wire and the lumen. 25 in-vivo data sets were used for validation. The intraclass correlation coefficient between the algorithmic results and manual delineations for the imaging catheter, the protective sheath and the lumen contour positions was 0.997, 0.949 and 0.974, respectively. All the guide wires were detected correctly and the Dice's coefficient of the shadow regions behind the guide wire was 0.97. 94.0% of 82 side branches were detected with 5.0% false positives and the Dice's coefficient of the side branch size was 0.85. In conclusion, the presented method has been demonstrated to be accurate and robust for side branch analysis.

5.1 Introduction

Despite decades of progress in understanding the development of coronary artery disease (CAD), it remains the most common cause of death in the world. Nowadays, percutaneous coronary intervention (PCI) with stenting is widely performed to open narrowed coronary arteries and to restore the oxygen-rich blood supply to the myocardium. Bifurcation lesions, accounting for about 20% of the PCI cases and expecting to further increase, are continuous one of the most complex anatomic structures and remain a challenge for interventionalists. Without a single preferred approach, a bifurcation lesion should be analyzed prior to the PCI to plan the interventional strategy, because bifurcation stenting often suffers from higher risks of acute and chronic complications such as acute thrombosis or late restenosis [1-3]. Furthermore, a stent placed in the main branch may partially obstruct the blood flow to small side branches and impact the PCI outcome [4-6]. Medical imaging, like coronary angiography (CA) and intravascular ultrasound (IVUS), has been used for side branch analysis [7-11]. Current approaches require the combination of multiple imaging modalities to assess lesion characteristics, analyze the blood flow and optimize stent placement with respect to optimal stent selection, deployment and expansion since every modality has its limitations. For image registration in the same or different modalities, side branches are reliable landmarks [12, 13].
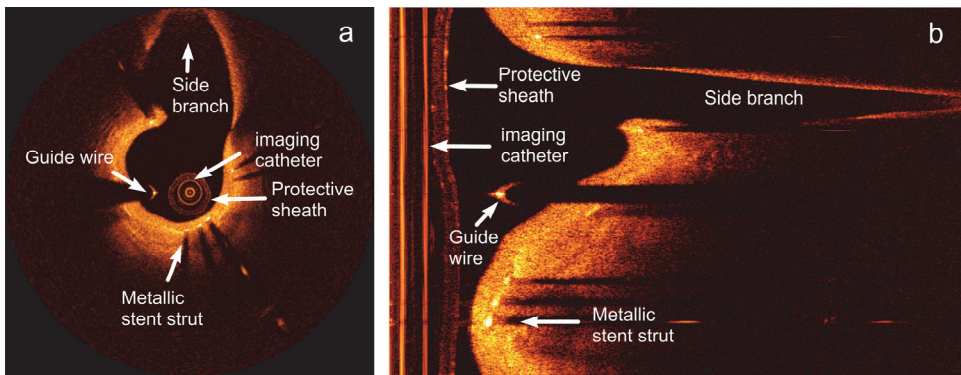
Figure 5-1. Two in-vivo IVOCT image examples. Figure (a) shows a Cartesian image, while figure (b) shows the corresponding polar image. In both images, a side branch, a guide wire, a metallic stent strut, the imaging catheter and the protective sheath are visible and annotated.

The continuous drive for optimal patient care demands precise delineation of the coronary vascular structures for accurate and reproducible quantifications. They can increase the understanding of CAD objectively and guide the intervention effectively, especially for patients with complex lesions. As a novel image modality, intravascular optical coherence tomography (IVOCT) has played a particular role in the setting of contemporary stenting by providing very high resolution (<20 µm) intracoronary images. It utilizes a fiber optic catheter to emit near-infrared light toward samples and receive the back scattered signal. A protective sheath covers the fiber catheter when it is rotating and being pulled back through the vessel and a guide wire is usually applied to facilitate the placement of the imaging catheter. Figure 1 presents two typical IVOCT

images. Compared with IVUS, the current golden standard for assessing lesion situation, IVOCT is more accurate and reproducible for quantitative analysis in many fields [14-19]. It is becoming a routine modality to guide PCI and quantify clinically interesting features including side branches and has be used in image fusion to provide detailed plaque composition and lesion extent [20-22].

Currently, most of the side branch identification in IVOCT images is done manually. In this paper, we present a fully automated method to detect side branches in IVOCT pullback runs based on accurate segmentations of all the common components of typical IVOCT images. The details of the method are described in section 2, while the validation method and the empirical results are presented in section 3 and section 4. The discussion and the conclusions of the proposed methods are given in section 5 and section 6, respectively.

5.2 Methods

As Fig. 1 shows, a side branch appears as a cavity in the vessel tissue so it can be detected by analyzing the distance variation between the lumen center and the leading-edge of the intimal layer. To accomplish this, all the bright components inside the lumen have to be removed and the guide wire shadow cavity in the vessel wall should be fixed in the beginning. Therefore, polar IVOCT images are pre-processed in four steps: (1) first, the imaging catheter is segmented and removed, so it will not affect the next step; (2) the guide wire is detected by analyzing the intensity profile of every scan-line; (3) after guide wire masking, the protective sheath is segmented for image correction and masking purposes; and in the end (4) the lumen contour is detected for lumen center calculation and guide wire shadow fixing. After the pre-processing, polar IVOCT images are converted into the Cartesian coordinate system, so that the distance between the lumen center and the leading-edge of the intimal layer can be computed and analyzed for side branch detection. In Fig. 2, a flow chart illustrates the main steps of this methodology. Details of each step are discussed in the follow paragraphs.
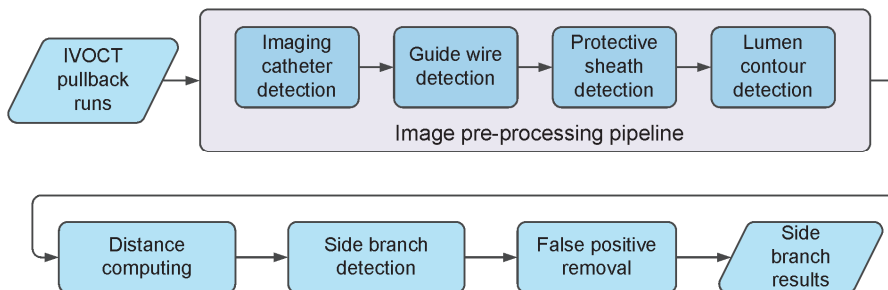
Figure 5-2. The flow chart of the presented side branch detection method.

5.2.1 Imaging catheter detection

As Fig. 1(b) shows, the imaging catheter appears as the rightmost bright vertical line in the polar IVOCT image and should be at a constant position in all frames in a pullback run. However, due to slight optical path length changes, the zero-point of a frame, also called Z-offset, can be different, which may lead to imaging catheter radius changes in a pullback run. As a result, the imaging catheter is segmented frame by frame. An extra complication is that the abluminal wall of the imaging catheter can be

blurred by the protective sheath attached to it or by bright (air bubble/blood) noise between the imaging catheter and the protective sheath. In contrast, the adluminal wall of the imaging catheter is always clear and can be used to define a region of interest (ROI) for the abluminal wall detection.

First, the image is converted into a binary image use a denoising threshold based on a percentile of its intensity histogram [23]. In this paper, it is the 80th percentile. Next, a vertical edge Prewitt compass operator is applied to generate a gradient image, followed by a normalizing operation on every scan-line. The normalized gradient in every column is multiplied by a coefficient based on the distance to the left boundary of the polar image, so that the imaging catheter has stronger weighted gradient value than other vertical lines. The coefficient equals to the column index divided by the image width. An example is presented in Fig. 3. To be more precise, the adluminal wall of the imaging catheter is first segmented and next, to its right, the abluminal wall is detected within a certain distance range. By analyzing their position variation in the pullback, outliers are replaced by interpolated results from neighboring frames. Finally, the imaging catheter and the image region to its left are masked so that the next processing will not be affected.
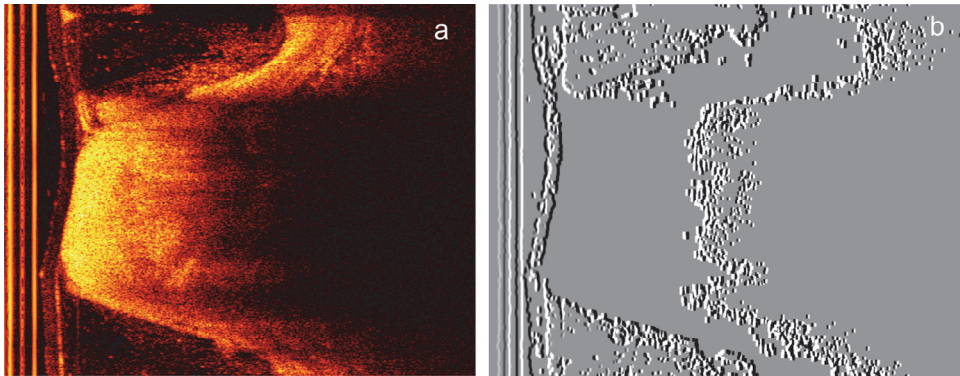
Figure 5-3. The imaging catheter and two other parallel vertical lines can be seen on the left of figure (a) and the corresponding distance weighted gradient image is given in figure (b). In figure (b), the adluminal wall of the imaging catheter is represented by negative values and the abluminal wall by positive values.

5.2.2 Guide wire detection

The guide wire appears as a bright crescent followed by a dark shadow because it reflects all the light during the IVOCT scanning. It needs to be segmented in this method as it can negatively affect the protective sheath and lumen contour detection. Moreover, cavities in the vessel wall caused by guide wire shadows should be fixed before the side branches can be effectively detected. Figure 4(a) demonstrates the intensity profile of a scan-line passing through a guide wire. The guide wire contains the highest intensity of this scan-line. After the peak point, the intensity value of the shadow region is close to zero. In contrast, in a scan-line passing through vessel tissue, the sum of intensities behind the peak point occupies a bigger proportion of the whole intensity sum like Fig. 4(b) shows. Hence, the guide wire can be detected by analyzing the intensity profiles.
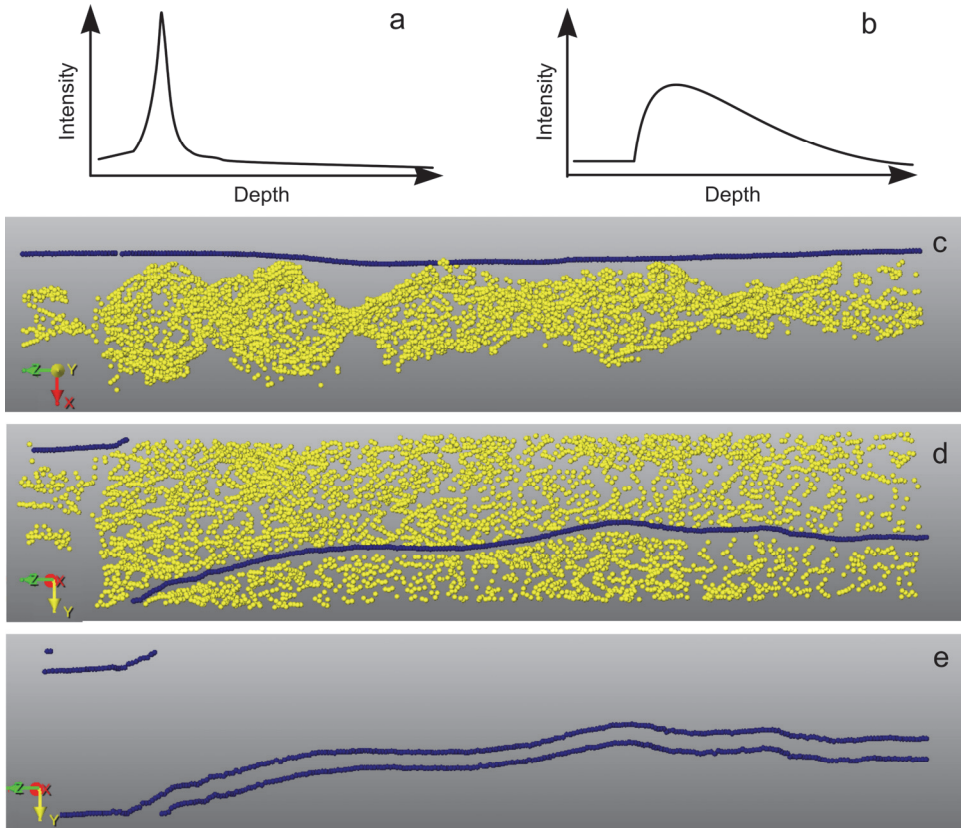
Figure 5-4. The Following imaging catheter removal, the intensity profile of a scan-line passing through a guide wire is given in figure (a) and passing through only tissue in figure (b). The candidate clusters (dots) detected in a polar pullback run are presented in two different viewpoints in figures (c) and (d). The yellow dots are noise like metallic struts and the blue dots indicate the guide wire which is continuous during the pullback run and located close to the imaging catheter. Figure (e) shows the shadow edges of the guide wire as blue dots.

The guide wire detection algorithm works as follows. First, for each scan-line, we detect its peak point (with maximum intensity value) and compute the proportion of the intensity sub-sum behind the peak point. If the proportion is lower than a threshold, this peak point may belong to a guide wire. In this research, this threshold is 0.75. These peak points are clustered into guide wire candidates frame by frame based on the distance as we have presented in [23]. As Figs. 4(c) and 4(d) present, the clustering results may contain false positives such as metallic stent struts, since they have a similar appearance as guide wires. In contrast to metallic struts and other noise, a guide wire is present in the all the frames of a pullback run. Moreover, its position does not change significantly between two adjacent frames and is usually close to the imaging catheter. To remove these, Dijkstra's algorithm [24] is used to detect the clusters which can be linked by the shortest path through the entire pullback. The cost function is the absolution position offset between two clusters from the adjacent frames. If multiple shortest paths were found, the one located closer to the imaging

catheter was selected. Based on the width of the cluster, the guide wire shadow edge positions can be detected as follow. First, a horizontal edge Prewitt compass operator is applied to the original polar image. Next, the guide wire shadow edges are detected by searching for the scan-line that has the strongest gradient sum within a certain distance from the initial top or bottom position of a guide wire cluster. The detected edges are given in Fig. 4(e).

5.2.3 Protective sheath detection

The protective sheath is a transparent tube-like cover which protects the imaging catheter from the vessel tissue. As Fig. 5(a) illustrates, the protective sheath usually appears as two bright parallel curved layers in the polar images because the image center is not the center of the protective sheath. Both the inner and outer layers have their own adluminal and abluminal wall. The protective sheath and the bright noise in it will be removed as they influence the lumen detection. Moreover, as the protective sheath has a fixed diameter, it is used for Z-offset correction [25]. The challenge lies in the complex image situations, as there could be bright noise between the imaging catheter and protective sheath, inside a protective sheath or between the protective sheath and vessel lumen as Figs. 5(b)–(d) show. Therefore, any of these four edges could be very unclear and should not be used alone for the segmentation.

First, a ROI is set in the polar image for protective sheath detection. It starts from the abluminal wall of the imaging catheter and should contain the whole protective sheath, and as little vessel tissue as possible. In this study, the ROI width was calculated based on the image resolution. Within the ROI, the polar images are down sampled by a factor of four to reduce the computation time and to smooth the final boundary. Next, a vertical edge Prewitt compass operator is applied to represent the dark-to-bright edges by positive values and bright-to-dark edges by negative values. To enhance the abluminal wall of the outer layer, its gradient value is combined with the gradient values of the other three edges [26]. As all four edges are generally paralleled, their relative distances are stable. According to the image resolution and protective sheath size, the distance between two layers is about 14 pixels and the layer thickness is about 6 pixels. More formally, the original gradient value at point (x, y) is denoted as $g(x, y)$. The combined gradient value $f(x, y)$ is related to the sum of four points:

$$f(x, y) = G(x, y) - 0.5E_1 + E_2 - 0.5E_3 \qquad (1)$$

with

$$G(x, y) = \begin{cases} g(x, y) & \text{in the ROI} \\ 0 & \text{others} \end{cases} \qquad (2)$$

$$E_1 = \max_{i \in [-6, -3)} \{G(x+i, y)\} \qquad (3)$$

$$E_2 = \min_{i \in [-20, -17)} \{G(x+i, y)\} \qquad (4)$$

$$E_3 = \max_{i \in [-26, -23)} \{G(x+i, y)\} \qquad (5)$$

Next, Dijkstra's algorithm is applied to detect the minimum cost path in the combined gradient image as the outer abluminal wall of the protective sheath. The cost function is $f(x, y)$. Examples are given in Figs. 5(a)–(d). Like Fig. 5(e), the detected contours are converted into the Cartesian coordinate system and then fitted

Chapter

5

to circles using a least-squares method [27]. Because the diameter and the center of the protective sheath should not change much between the neighboring frames, a median filter is applied to remove outliers and replace them by interpolation. Figure 5(f) presents the center shifting and size changing of the protective sheath along the pullback run. The Z-offset is corrected according to the protective sheath diameter in every frame. Finally, the protective sheath is masked out before lumen detection.
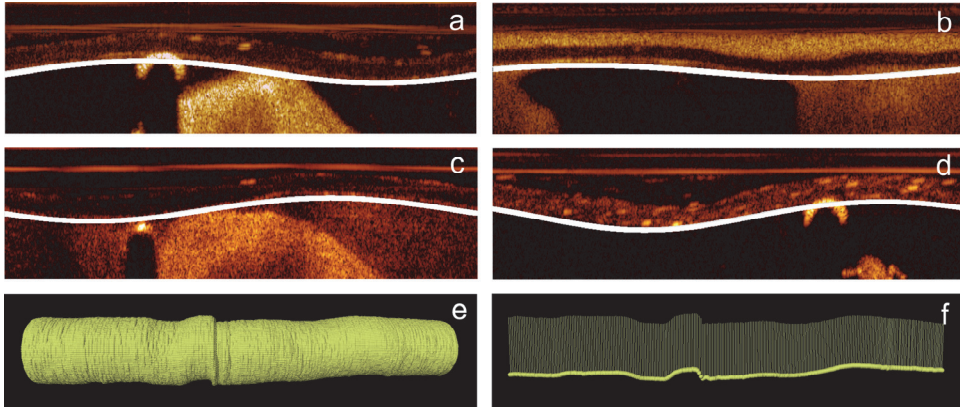
Figure 5-5. Figure (a) illustrates a normal protective sheath appearance. However, bright noise may exist between the imaging catheter and the protective sheath like figure (b), between the protective sheath and the lumen contour like figure (c) shows, or inside the protective sheath like figure (d). White curves indicate the detected protective sheath. A 3D visualization of the protective sheath contours in a Cartesian dataset is given in figure (e). The corresponding contour center (yellow dots) and the radii (yellow vectors) are presented in figure (f). In figures (e) and (f), the scale between the axial direction and longitudinal direction is about 1:10.
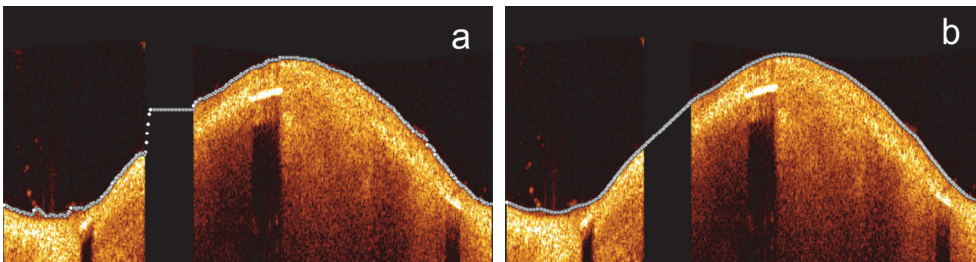
Figure 5-6. Figure (a) shows the originally detected lumen contour (white dots in each scan-line). The segment in front of the guide wire shadow does not fit the lumen trend. Using the guide wire width information, this part of the lumen contour is smoothly interpolated like figure (b) demonstrates.

5.2.4 Lumen contour detection

To compute the lumen center accurately, the lumen detection must follow the main vessel wall as much as possible, and pass over possible cavities like side branches or guide wire shadows. In this work, Dijkstra's algorithm is used with a side-step restriction. The cost matrix is the gradient image and the side step was limited to

10 pixels in accordance to the image size in this research to insure the minimum cost path passing over cavities. The side-step cost is 80. To avoid the strong gradient inside the tissue, first, all the intensity values above a given threshold are replaced by the constant value. The threshold is computed for each frame based on a fixed percentile of the intensity histogram, because even in the same pullback run, vessel tissue can have very different intensities in different frames. We have chosen the 85th percentile. After thresholding, the same Prewitt compass operator for vertical edges is applied to generate a gradient image as the cost matrix and the minimum cost path in this matrix is detected and defined as the lumen contour.

As the guide wire shadow in the lumen tissue region does not contain any edge information, the detected minimum cost path in this region could be wrong as shown in Fig. 6(a). This piece of lumen contour is located according to the guide wire width detected in section 2.2. It is replaced by linear interpolation in the polar coordinate system for smoothness as shown in Fig. 6(b), because the width of a guide wire usually is narrow when compared with that of the whole image. After converted into Cartesian coordinate system, the whole lumen contour looks natural. Along with the interpolated curve, the guide wire shadow cavity in the vessel tissue is fixed (filled) before the side branch detection.

5.2.5 Distance computing

A side branch can be detected by analyzing the distance variation between the lumen center and the leading edge of the intimal layer. A sharp increase in the distance indicates the possible existence of a side branch. Since very small side branches barely have clinical significance and cannot be used as reliable landmarks for image registration, we focus on side branches which are more than 8 degrees wide in the circumferential direction and continuous in at least 4 frames (about 0.8 mm). This is also the size restriction of the presented side branch detection method. First, the lumen center is determined. In case a detected main lumen area contains parts of a big side branch lumen as Fig. 7(a) shows, the center of the lumen contour would move to the side branch position, which results in a shorter distance than normal. To avoid this error, the main lumen region needs to be located. As the main vessel can be treated as a tube containing the imaging catheter, the maximum circle inside the lumen contour which contains the imaging catheter is defined as the main lumen region and its center is the lumen center. The lumen center is determined by using a distance transformation based method [5]. First, a binary image was generated from the detected lumen contour in which the lumen region was presented as 1 and the others as 0. Next, a distance transformation converted the binary image into another image where all nonzero pixels get a value which corresponds to the distance to the nearest lumen contour boundary. The center of the lumen is now identified by determining the maximum value in the distance transformation image. After detecting the lumen center, the distance to the intimal layer is computed every two degrees by looking for the first pixel having intensity value above the tissue threshold defined in section 2.4. If no tissue pixel is found, the search stops at the image border. Two examples are given in Figs. 7(b) and 7(c).

Chapter

5
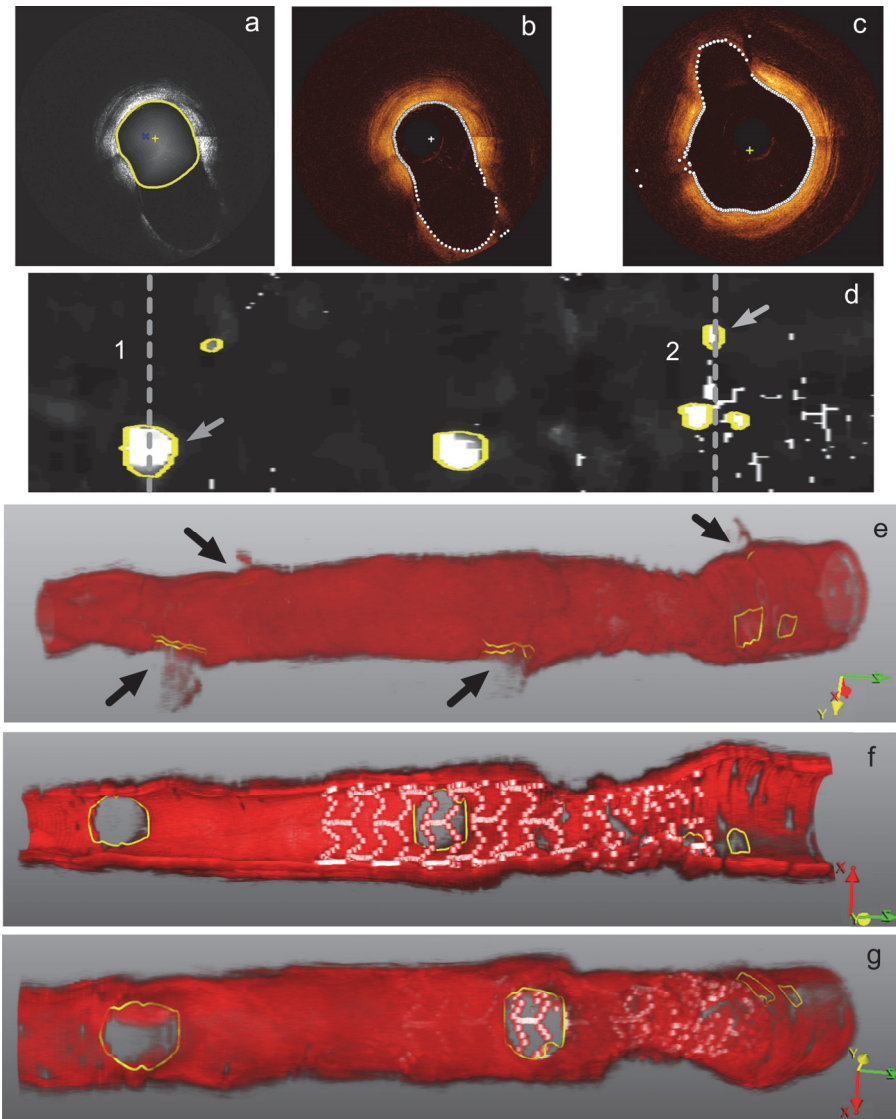
Figure 5-7. Figure (a) presents a detected lumen contour (yellow) containing part of a big side branch. The white overlay in the contour is the distance transformation result. The lumen center (yellow "+") and the image center (blue "×") are given as well. From the lumen center, the leading-edge of intimal layer is detected in all angles and the results are presented as white dots in figures (b) and (c). They show two cross-sections (vertical line 1 and 2) of figure (d). The distance matrix for this pullback run can be treated as a 2D image like figure (d) in which side branches are detected as yellow contours. Arrows indicate the side branches in figures (b) and (c). Figure (e) shows the corresponding 3D side branches (yellow contours). Arrows point to the opening of some side branches. Parts of side branch walls are visible. Figures (f) and (g) show the side branches in an opened vessel with the opposite view angles. To show side branches clearly, the viewing angles follow the side branch direction. The white dots are implanted bioresorbable stent struts.

5.2.6 Side branch detection

After the distance computation, we get a 2D matrix which contains the distance for all angles along the whole pullback run. The distances are normalized in each frame to unify different lumen sizes. While normalizing, the median distance in each frame is scaled to 1.0 and the other distances are scaled proportionally. By converting distances to intensities, the matrix can be treated as a 2D image as shown in Fig. 7(d) in which the side branches are represented by bright regions which have high intensity values and acceptable size. To detect these regions, the image is first smoothed and a 2D region growing method is applied to find all the connected pixels above a threshold. In this study, the threshold is set to 1.4. To filter out false positives caused by highly eccentric elliptical lumen contours, bright regions should contain at least one pixel whose intensity value is two times higher than the median value. Next, the regions which are too small according to the size restriction in section 2.5 are removed. The detection results are shown in Fig. 7(d). Finally, all these 2D results are transformed back to the original 3D IVOCT pullback runs based on the lumen centers and their distance to the lumen centers as Figs. 7(e)–(g) demonstrate.

5.2.7 False positive removal

The detected results could still contain false positives because black cavities in the vessel tissue are not always side branches. Because of the limited penetration capability of IVOCT, it may result in a cavity in the vessel wall when the imaging catheter touches the tissue as Fig. 8 illustrates. However, in this situation, the angle difference between the image center and the edges of this cavity is close to zero. Based on this feature, this type of false positives is easily removed.

Chapter

5
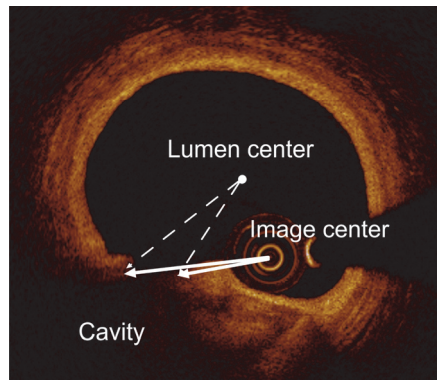
Figure 5-8. The false positive (based on the dashed lines) resulted from the tissue coverage over the imaging catheter. The angles from the image center to the side branch edges (between the solid lines) are almost the same.

If a pullback contains densely spaced incomplete apposed metallic stent struts, they could generate wide shadows in the vessel tissue and may lead to false positives. In a previous paper [23], we presented an automated method to detect metallic stent struts and their shadow regions. The stent strut and their shadow positions can be used for cross checking with the side branch candidates. A side branch candidate that is overlaid mainly with struts can be a false positive and should be removed.

5.3 Materials and validation method

The presented side branch detection method was developed using the MeVisLab toolbox 2.2.1 (MeVis Medical Solutions AG, Bremen, Germany) together with in-house developed C++ modules. A total of 25 random selected in-vivo IVOCT pullback runs were used to evaluate the presented method. All the images were acquired with a C7-XR OCT intravascular imaging system (St. Jude Medical, Westford, MA, USA) and the image resolution is 5.86 μm × 5.86 μm × 200 μm. The pullback runs include baseline datasets and follow-up datasets at different time points. For 23 out of 25 datasets, each contains 271 frames (using a pullback speed of 20 mm/sec) while for the other 2 datasets, each contains 541 frames (using a pullback speed of 10 mm/sec). 19 datasets contain guide wires. 14 pullback runs contain metallic stents; 6 pullback runs have bioresorbable vascular scaffolds (BVS) and 5 others contain no stent or scaffold.

One observer manually marked the imaging catheter, the guide wire region, the protective sheath contour and the lumen contour in one frame out of every 25 frames in each pullback. The boundaries of all side branches that are more than 8 degrees wide in the circumferential direction and continuous in at least 4 frames were marked. In total, 82 side branches were marked in 22 pullback runs and in the remaining 3 pullback runs, no visible side branches were found due to guide wire shadow blockage, massive residual blood noise or poor image quality. Therefore, they were excluded from the side branch detection validation. A second independent observer marked the ground truth in a subset containing 5 pullback runs. When marking the ground truth, in case a side branch was partly blocked by a guide wire shadow or residual blood, its boundary was estimated based on the 3D information and personal experience.

5.4 Results

The inter-observer agreements were measured using the intraclass correlation coefficient (ICC) and the Dice's coefficient. The ICC of the imaging catheter radius, the protective sheath radius and the lumen contour position between two observers were 0.983, 0.942 and 0.999. Here, the lumen contour positions were compared in radial direction from the image center in every 2 degrees. The distance between the protective sheath centers was 1.21 ± 0.57 pixels. The average Dice's coefficient between the corresponding guide wire shadow regions was 0.97 ± 0.02. Both two observers agreed on all 15 side branches in the subset and the average Dice's coefficient of their angle regions were 0.92 ± 0.07.

During the validation, the performance of the presented methods was measured using the ICC and the Dice's coefficient. Moreover, the radius error of the imaging catheter and protective sheath, the distance error of the protective sheath center and lumen contour were computed as well. Compared with the ground truth from the first and the second observer, the detected imaging catheter radii had an average error of -0.63 ± 1.13 and -0.93 ± 1.40 pixels. The corresponding ICC was 0.998 and 0.977. The detected protective sheath radii had an average error of 0.90 ± 0.67 and 1.05 ± 0.61 pixels while the corresponding ICC was 0.986 and 0.949. The average distance error of the protective sheath centers was 1.25 ± 0.79 and 1.15 ± 0.61 pixels. The average Dice's coefficient for guide wire region was 0.97 ± 0.03 and 0.97 ± 0.02. The lumen contour distance error was computed in radial direction from the image center for every 2 degrees and the average error was -2.56 ± 12.21 and 1.49 ± 7.27 pixels. The ICC of the

lumen contour position was 0.940 and 0.974. Overall, 94.0% of 82 side branches were correctly detected with 4.9% of false positives, while in the subset, 93.3% of 15 side branches were detected with 6.7% false positives. The average Dice's coefficient of the angle region between the detected side branches and the ground truth from two observers was 0.85 ± 0.06 and 0.77 ± 0.07, separately. Overall, 31 side branches were at least 1.0 mm in the longitudinal direction and had a maximum angle region of at least 60 degrees. These big side branches are more important than small side branches as they are solid bio-landmarks for image registration and essential for bifurcation lesion treatment. In the validation, 100% of these big side branches were successfully detected. A summary of the detailed inter-observer agreements and validation results are presented in Table 1.

Table 1. The similarity and difference among the ground truth (GT1) from the first observer, the ground truth (GT2) from the second observer and the algorithmic result (AR). For the imaging catheter radius (ICR), protective sheath radius (PSR) and lumen contour position (LM), the similarity is given as the intraclass correlation coefficient (ICC) and the difference is given as the average size difference (Diff) in pixels. The protective sheath center (PSC) position error is also measured by the average distance difference in pixels. The true positive rate (TP) and false positive rate (FP) are used for side branch (SB) detection performance. The overlaid region for the guide wire (GW) and SB is measured by the average Dice's coefficient (Dice)

Groups	ICR		GW region	PSR		PSC	Lumen		SB (%)		SB region
	ICC	Diff	Dice's	ICC	Diff	Diff	ICC	Diff	TP	FP	Dice's
GT1/GT2	0.983	-1.40	0.97	0.942	0.18	1.21	0.999	-0.13	100	0.0	0.92
GT1/AR	0.998	-0.63	0.97	0.986	0.90	1.25	0.940	-2.56	94.0	5.0	0.85
GT2/AR	0.977	0.93	0.97	0.949	1.05	1.05	0.974	1.49	94.0	5.1	0.77

Chapter

5

5.5 Discussion

The performance of the presented side branch detection method depends heavily on the accuracy of the image segmentation in the pre-processing step. Moreover, segmentations of all the common components in IVOCT images are also important for many image processing and quantitative analyses. For example, imaging catheter detection is commonly required for lumen detection [28, 29] and metallic strut detection [23], because its high intensity is a negative influence. A guide wire could be mistakenly detected as a metallic strut due to its appearance [30, 31]. The protective sheath diameter can be used for Z-offset correction [25] as 1% change in the magnitude of the ideal Z-offset can result in a 12% to 14% error in area measurements, which may lead to misinterpretation [32]. Currently, only 38% of the peer-reviewed papers present correctly calibrated images [29]. Lumen contour detection is one of most common image segmentation steps and the published methods include Markov random field and wavelet transform analysis [28], fuzzy C means clustering and

wavelet transform [33], deformable spline models [34] and dynamic programming [35]. However, in many cases, only a light-weight and fast lumen contour estimation like our method is needed.

As the adluminal wall of an imaging catheter is clearer and more reliable than the abluminal wall, the firstly detected adluminal wall indicated an accurate ROI for the following abluminal wall detection. According to the validation results, the detected imaging catheter radii had an average error of less than 1 pixel. The error was mainly caused by the bright air bubble, blood noise or attached protective sheath which blurred the abluminal wall. The errors caused by these artifacts were mostly corrected by the median filter because they normally did not affect the majority of a pullback run.

All the guide wires were detected with no false positions. The Dice's index between the detected guide wire region and the ground truth was 0.97. The presented method searched for guide wire shadow edges for lumen fixing but a guide wire shadow edge could be blocked by metallic struts, so that the guide wire width may be overestimated. A similar situation was when a guide wire shadow region is overlaid with side branches. However, the searching depth limitation prevents the overestimation goes too far. A limitation is that only one guide wire can be detected automatically in a pullback run. A-priori knowledge of guide wire number is needs to detect additional guide wires.

The radius error and the center position error of the detected protective sheath are both about 1 pixel, which ensures accurate Z-offset correction in IVOCT images. Combining all four edges of the protective sheath greatly prevents the segmentation from being affected by complex noise around the protective sheath. Furthermore, circle fitting overcomes local distortions and the radius filter can remove outliers in the whole pullback.

In the radial direction, the detected lumen contour had an average distance error about 3 pixels. Most of the large differences between the algorithmic results and the ground truth occurs when side branches or part of a large lumen were invisible due to the limited penetration depth of IVOCT. Since we set a side-step limitation for the dynamic programming method, it returned a relatively smooth lumen contour which skipped sharp peaks and cavities. The ground truth was drawn based on personal experience which could be different. Some errors also resulted from the bright noise inside the lumen such as thrombi and malapposed struts, especially when they were located close to the real lumen boundary. In these cases, the detected lumen contour followed the leading edge of the bright noise instead of the lumen.

With the foregoing precise pre-processing steps, our method successfully detected 94.0% of 82 side branches including all the big side branches with less than 5% false positives. The Dice's index of the side branch angle size is 0.85. The side branch boundary was detected based on the distance change which is highly reproducible. The biggest side branch size errors were caused by the guide wire shadows. When a side branch was partly blocked by a guide wire, the detected side branch would be incomplete due to the guide wire shadow fixing. In contrast, the observers included these areas when they draw the side branch boundaries, so that the ground truth contained the shadow blocked region which resulted in a difference with the algorithmic results. However, these guide wire blocked side branches can still be used as landmarks or awareness of the existence of side branches, but their size is no

reliable for assessment. The other side branch results could be used for precise measurement.

In case the detection result is inaccurate, our prototype system provides a user interface for correction. All the detected side branches are indexed so the user can select or delete any side branch contour. As the 3D contour is generated from side branch edge points in each cross-sectional frame, the corresponding adjustment will be done in the 2D images. After modifying or adding the 2D side branch edge points, a new 3D side branch contour can be generated.

The presented side branch method also has limitations. It depends on the cavity detection in the tissue, but the guide wire, residual blood, plaque rupture, thrombus and calcified nodule also cause cavities and only the guide wire shadows were fixed. In the algorithmic results, we found 60% of the false positives were caused by the residual blood shadow. The remaining 40% of the false positives resulted from the shadows due to air bubbles in the protective sheath. Furthermore, using only distance based detection could also fail to detect some side branches, especially when a stent was present, because the malapposed struts and the tissue coverage may seal side branches. Two of five false negatives in the validation results were almost sealed by dense malapposed struts and very thick tissue coverage. The third false negative was caused by the guide wire shadow which covered the majority of this side branch. Another missed side branch was narrow and almost perpendicular to the scan line from the lumen center, so that the distance between lumen center and the leading-edge of intimal layer did not reveal the existence of this side branch. The last false positive was a tiny side branch on a very big main vessel lumen. Only in one frame, it was 8 degrees wide in circumferential direction. After the normalization, this side branch area shrank and later was removed mistakenly. Poor image quality including residual blood or other artifacts in the side branch area could affect the detection performance as well.

5.6 Conclusion and future work

As IVOCT contributes to clinical researchers and cardiologists by providing a better understanding of the in-vivo artery situation, there are increasing demands of side branch analysis in IVOCT images. In this paper, we presented a fully automated side branch detection method in IVOCT pullback runs based on an image segmentation pipeline including the imaging catheter, the protective sheath, the guide wire and the lumen. The validation showed a good agreement between the algorithmic results and the ground truth which suggested that this method could be used to indicate side branches and assist image registration. The accuracy of the image segmentation for pre-processing also implied that the segmentation results of all the common components in IVOCT images may contribute to accurate IVOCT Z-offset correction, stent strut detection, 3D visualization and many other quantitative analysis applications.

In future, we would like to improve the detection method by adding new false positive filters, using pullback runs acquired with a higher frame rate and utilizing extra information including longitudinal cross-sectional IVOCT images.

Chapter

5

5.7 References

1. J. Hermiller and A. Rizvi, "Commentary: Bifurcations: the problem is the side branch," J Invasive Cardiol 18, 461 (2006).

2. G. Karavolias, P. Karyofillis, P. Georgiadou, and V. Voudris, "Unprotected left main distal bifurcation lesion," Hellenic J Cardiol 53, 480-484 (2012).

3. W. F. Shen, "Technical refinement for treatment of coronary bifurcation lesion is still demanding," Chin Med J (Engl) 122, 2083-2085 (2009).

4. B. Hong, K. Z. Wang, Q. H. Huang, Y. Xu, X. G. Fang, Z. Li, and J. M. Liu, "Effects of metal coverage rate of flow diversion device on neointimal growth at side branch ostium and stented artery: an animal experiment in rabbit abdominal aorta," Neuroradiology 54, 849-855 (2012).

5. A. Wang, J. Eggermont, N. Dekker, P. J. de Koning, J. H. Reiber, and J. Dijkstra, "3D assessment of stent cell size and side branch access in intravascular optical coherence tomographic pullback runs," Comput Med Imaging Graph 38, 113-122 (2014).

6. A. Y. Her, J. S. Kim, Y. H. Kim, D. H. Shin, B. K. Kim, Y. G. Ko, D. Choi, Y. Jang, and M. K. Hong, "Histopathologic validation of optical coherence tomography findings of non-apposed side-branch struts in porcine arteries," J Invasive Cardiol 25, 364-366 (2013).

7. W. J. Jang, Y. B. Song, J. Y. Hahn, S. H. Choi, H. S. Kim, C. W. Yu, S. W. Rha, Y. Jang, K. B. Seung, and H. C. Gwon, "Impact of bifurcation stent technique on clinical outcomes in patients with a Medina 0,0,1 coronary bifurcation lesion: Results from the COBIS (COronary BIfurcation Stenting) II registry," Catheter Cardiovasc Interv (2014).

8. D. Dudek, R. Mehran, A. Dziewierz, S. J. Brener, T. Rakowski, M. Brzezinski, B. R. Brodie, K. Xu, M. Fahy, A. J. Lansky, K. Zmudka, and G. W. Stone, "Impact of bifurcation target lesion on angiographic, electrocardiographic, and clinical outcomes of patients undergoing primary percutaneous coronary intervention (from the Harmonizing Outcomes With Revascularization and Stents in Acute Myocardial Infarction [HORIZONS-AMI] trial)," EuroIntervention 9, 817-823 (2013).

9. M. J. Kern, "Bifurcation angiographic lesion assessment," Catheter Cardiovasc Interv 82, 422-423 (2013).

10. R. A. Costa, M. A. Costa, and I. D. Moussa, "Bifurcation lesion morphology and intravascular ultrasound assessment," Int J Cardiovasc Imaging 27, 189-196 (2011).

11. N. Gonzalo, H. M. Garcia-Garcia, E. Regar, P. Barlis, J. Wentzel, Y. Onuma, J. Ligthart, and P. W. Serruys, "In vivo assessment of high-risk coronary plaques at bifurcations with combined intravascular ultrasound and optical coherence tomography," JACC Cardiovasc Imaging 2, 473-482 (2009).

12. S. Tu, L. Xu, J. Ligthart, B. Xu, K. Witberg, Z. Sun, G. Koning, J. H. Reiber, and E. Regar, "In vivo comparison of arterial lumen dimensions assessed by co-registered three-dimensional (3D) quantitative coronary angiography,

intravascular ultrasound and optical coherence tomography," Int J Cardiovasc Imaging 28, 1315-1327 (2012).

13. J. H. Reiber, S. Tu, J. C. Tuinenburg, G. Koning, J. P. Janssen, and J. Dijkstra, "QCA, IVUS and OCT in interventional cardiology in 2011," Cardiovasc Diagn Ther 1, 57-70 (2011).

14. S. Fedele, G. Biondi-Zoccai, P. Kwiatkowski, L. Di Vito, M. Occhipinti, A. Cremonesi, M. Albertucci, L. Materia, G. Paoletti, and F. Prati, "Reproducibility of coronary optical coherence tomography for lumen and length measurements in humans (The CLI-VAR [Centro per la Lotta contro l'Infarto-VARiability] study)," Am J Cardiol 110, 1106-1112 (2012).

15. T. Kubo, T. Akasaka, J. Shite, T. Suzuki, S. Uemura, B. Yu, K. Kozuma, H. Kitabata, T. Shinke, M. Habara, Y. Saito, J. Hou, N. Suzuki, and S. Zhang, "OCT compared with IVUS in a coronary lesion assessment: the OPUS-CLASS study," JACC Cardiovasc Imaging 6, 1095-1104 (2013).

16. R. Du, R. Y. Zhang, Q. Zhang, Y. H. Shi, J. Hu, Z. K. Yang, F. H. Ding, J. S. Zhang, and W. F. Shen, "Assessment of the relation between IVUS measurements and clinical outcome in elderly patients after sirolimus-eluting stent implantation for de novo coronary lesions," Int J Cardiovasc Imaging 28, 1653-1662 (2012).

17. S. J. Kim, H. Lee, K. Kato, T. Yonetsu, and I. K. Jang, "In vivo comparison of lumen dimensions measured by time domain-, and frequency domain-optical coherence tomography, and intravascular ultrasound," Int J Cardiovasc Imaging 29, 967-975 (2013).

18. N. Gonzalo, P. W. Serruys, H. M. Garcia-Garcia, G. van Soest, T. Okamura, J. Ligthart, M. Knaapen, S. Verheye, N. Bruining, and E. Regar, "Quantitative ex vivo and in vivo comparison of lumen dimensions measured by optical coherence tomography and intravascular ultrasound in human coronary arteries," Rev Esp Cardiol 62, 615-624 (2009).

19. A. Maehara, G. S. Mintz, and G. W. Stone, "OCT versus IVUS: accuracy versus clinical utility," JACC Cardiovasc Imaging 6, 1105-1107 (2013).

20. C. Costopoulos, T. Naganuma, A. Latib, and A. Colombo, "Optical coherence tomography of a bifurcation lesion treated with bioresorbable vascular scaffolds with the "mini-crush" technique," JACC Cardiovasc Interv 6, 1326-1327 (2013).

21. M. J. Grundeken, R. P. Kraak, D. M. de Bruin, and J. J. Wykrzykowska, "Three-dimensional optical coherence tomography evaluation of a left main bifurcation lesion treated with ABSORB(R) bioresorbable vascular scaffold including fenestration and dilatation of the side branch," Int J Cardiol 168, e107-108 (2013).

22. C. Di Mario, I. Iakovou, W. J. van der Giessen, N. Foin, T. Adrianssens, P. Tyczynski, L. Ghilencea, N. Viceconte, and A. C. Lindsay, "Optical coherence tomography for guidance in bifurcation lesion treatment," EuroIntervention 6 Suppl J, J99-J106 (2010).

23. A. Wang, J. Eggermont, N. Dekker, H. M. Garcia-Garcia, R. Pawar, J. H. Reiber, and J. Dijkstra, "Automatic stent strut detection in intravascular optical coherence tomographic pullback runs," Int J Cardiovasc Imaging 29, 29-38 (2013).

Chapter

5

24. E. W. Dijkstra, "A note on two problems in connexion with graphs," Numer. Math. 1, 269-271 (1959).

25. H. G. Bezerra, M. A. Costa, G. Guagliumi, A. M. Rollins, and D. I. Simon, "Intracoronary optical coherence tomography: a comprehensive review clinical and research applications," JACC Cardiovasc Interv 2, 1035-1046 (2009).

26. M. Sonka, X. Zhang, M. Siebes, M. S. Bissing, S. C. Dejong, S. M. Collins, and C. R. McKay, "Segmentation of intravascular ultrasound images: a knowledge-based approach," IEEE Trans Med Imaging 14, 719-732 (1995).

27. D. Umbach and K. N. Jones, "A few methods for fitting circles to data," Ieee T Instrum Meas 52, 1881-1885 (2003).

28. S. Tsantis, G. C. Kagadis, K. Katsanos, D. Karnabatidis, G. Bourantas, and G. C. Nikiforidis, "Automatic vessel lumen segmentation and stent strut detection in intravascular optical coherence tomography," Med.Phys. 39, 503-513 (2012).

29. L. Hebsgaard, E. H. Christiansen, and N. R. Holm, "Calibration of intravascular optical coherence tomography as presented in peer reviewed publications," Int J Cardiol 171, 92-93 (2014).

30. G. Unal, S. Gurmeric, and S. G. Carlier, "Stent implant follow-up in intravascular optical coherence tomography images," Int.J.Cardiovasc.Imaging 26, 809-816 (2010).

31. G. J. Ughi, T. Adriaenssens, K. Onsea, P. Kayaert, C. Dubois, P. Sinnaeve, M. Coosemans, W. Desmet, and J. D'Hooge, "Automatic segmentation of in-vivo intra-coronary optical coherence tomography images to assess stent strut apposition and coverage," Int J Cardiovasc Imaging 28, 229-241 (2012).

32. S. Tahara, H. G. Bezerra, M. Baibars, H. Kyono, W. Wang, S. Pokras, E. Mehanna, C. L. Petersen, and M. A. Costa, "In vitro validation of new Fourier-domain optical coherence tomography," EuroIntervention 6, 875-882 (2011).

33. K. Mandelias, S. Tsantis, D. Karnabatidis, P. Katsakiori, D. Mihailidis, G. Nikiforidis, and G. C. Kagadis, "Fast and Robust Algorithm Towards Vessel Lumen and Stent Strut Detection in Optical Coherence Tomography," Med.Phys. 39, 3645-3646 (2012).

34. S. Gurmeric, G. G. Isguder, S. Carlier, and G. Unal, "A new 3-D automated computational method to evaluate in-stent neointimal hyperplasia in in-vivo intravascular optical coherence tomography pullbacks," Med.Image Comput.Comput.Assist.Interv. 12, 776-785 (2009).

CHAPTER

6

Summary and conclusions

6.1 Summary and conclusions

For decades, coronary artery disease (CAD) has remained one of the leading causes of death worldwide despite the enormous progress in modern medical knowledge of diagnosing and treating. Atherosclerosis development in coronary arteries is the major pathophysiology of CAD which narrows the lumen volume and results in restricted oxygen-rich blood supply to myocardium. The CAD treatment includes lifestyle changes, medications and medical procedures. In 1977, the invention of balloon angioplasty by Andreas Grüntzig struck a prelude to the revolution of percutaneous coronary intervention (PCI) as a new revascularization method for CAD treatment. Undergone an evolution over the past few decades, PCI has been proven to be an effective and less costly medical procedure compared with surgeries such as coronary artery bypass grafting and regarded as one of the primary choices to treat the ischemic heart disease. Nowadays, stenting operation has been applied in most of the PCI procedures as one of the most remarkable improvements. Stent is a small medical device to support vessel wall after the angioplasty to overcome the risk of acute vessel closure. The first available stent was a bare metal stent (BMS) and later the drug-eluting stent (DES) was invented to overcome the risks of BMS such as in-stent neointimal hyperplasia. Both BMS and DES are permanent so that the stented vessel is caged by metal and late advanced vascular remodeling could no longer be applied. Therefore, bioresorbable vascular scaffold (BVS) was invented as a temporary device which can support the vessel after the implantation and slowly be absorbed by tissue during the follow up.

Continuous demand for optimal CAD diagnosis and treatment drives the evolution of medical imaging technologies. Before the invention of intravascular optical coherence tomography (IVOCT), many image modalities, including non-invasive ones like computed tomography (CT) and invasive ones like coronary angiography and intravascular ultrasound (IVUS), have been conventionally used during the research and clinical routine for CAD treatment. However, none of them have sufficient resolution to delineate fine structures such as thin fiber caps of vulnerable plaques or thin tissue coverage of stent struts. IVOCT is a new near-infrared light source based imaging technology which can acquire three-dimensional (3D) in-vivo images of vessels with a resolution of about 10 micrometers. The latest frequency-domain IVOCT imaging system has already dramatically improved the imaging speed and signal to noise ratio. Its unparalleled resolution makes it currently the only image modality for accurate stent analysis. The goal of this thesis was therefore to develop efficient and accurate algorithms to process IVOCT images for stent analysis and stenting optimization.

Stent analysis, for example the strut distribution, strut number, strut position and intra-strut angle, is highly interested as it has assisted the continuous improvements in stent manufacturing for such as better support to vessel well, flexibility for implantation and dosing of drug from DES. Furthermore, stent analysis is also increasingly used to improve the efficacy of stenting in PCI procedures by suggesting optimal stent size and proper stent expansion. Undersized stent or insufficient expansion can result in stent malapposition while stent deployment failure can cause incomplete lesion coverage. The risks include late neointimal hyperplasia and late stent malapposition. As a result, an accurate stent strut detection method in IVOCT could significantly reduce the risks of vessel revascularization. However, given the large number of the struts visible in a pullback run covering an entire stent length,

quantitative analysis is only feasible when the strut detection is carried out automatically. In **Chapter 2**, we presented a novel automated method to detect metallic stent struts in IVOCT pullback runs. As the metallic stent strut appears as a bright spot with a long, dark shadow behind it, the proposed algorithm analyzed the intensity distribution in every scan line to detect the candidate pixels that may belong to metallic struts. Next, strut shadow edges were detected and innovatively used as restrictions to remove the false candidate pixels and cluster the rest into candidate struts. Even if candidate pixel detection fails for a strut due to the thick tissue coverage or artifacts, this strut could be retrieved only based on its shadow edges. In the end, guide wires were removed and the strut center positions were computed. Validated with all 18001 struts in 10 in-vivo pullback runs with different image quality (high, median and low), 91% of malapposed struts, 93% of apposed struts and 94% of tissue-covered struts were detected with only 4% of false positives. With the validation results, the presented detection method demonstrated its possibility to be used for quantitative stent analysis.

Unlike metallic stents, BVS is commonly made of various polymers and has different appearance in IVOCT images. For accurate BVS strut analysis, IVOCT is currently the most suitable imaging technique due to its high resolution and the translucency of polymeric BVS struts. The internal composition of a BVS strut is homogeneous so that transmitted light can pass through it and backscattering originates from the difference in refractive index between the strut and its environment such as flush fluid or tissue. Therefore, BVS struts appear as bright boxes with black cores. Similar as metallic strut detection, BVS strut detection also could be used for stent analysis. Moreover, to track the bioresorption process of BVS, the strut area is also interested. Therefore, in **Chapter 3**, we presented an automated BVS strut detection method in IVOCT pullback runs to segment the black cores of BVS struts. Based on the strut location difference between baseline and follow-up datasets, the lumen contour was used to indicate different reliable regions of interest (ROI) for strut detection. This method detected short line segments belonging to black cores and then clustered them to generate smoothed black core contours. Validated with 6 in-vivo IVOCT pullback runs, including 3 baseline datasets and 3 follow-up datasets, this algorithm correctly detected 90.4% of 2183 baseline BVS struts and 96.6% of 2508 follow-up BVS struts with 3.0% and 0.8% false positives, respectively. BVS strut area was measured by the black core region and the performance was validated using Dice's coefficient. For baseline datasets, the Dice's coefficient between the ground truth and algorithmic results was 0.83 while in follow-up datasets, the Dice's coefficient is 0.85. The validation study showed that the new method can accurately detect BVS struts and measure their core areas which could be a useful tool for 3D reconstruction, tissue coverage thickness measurement, malapposition analysis, strut distribution and bioresorption assessment.

In addition to the stent type evolution, the impact of the stent design to the treatment outcome has gained increasing attentions. Existing stent design analysis mainly focuses on the two-dimensional (2D) information such as strut number, distribution or inter-angle in a single frame. However, it has been proved that stent cell structure could influence the stent support ability, expansion ability, flexibility, conformability, dosing distribution and side branch access. As it is naturally a 3D structure, the stent cell should be measured in 3D space. Both full stent cell size and maximum circular unsupported surface area (MCUSA) are currently used to evaluate stent influence to the vessel wall. In **Chapter 4**, we presented a semi-automated

Chapter

6

method to measure the stent cell size, MCUSA and side branch access through stent cells. First, the 3D stent surface and stent cell contour were reconstructed from the detected struts for the stent cell surface segmentation and measurement. A 2D approximation of the stent cell surface was generated to detect and measure its MCUSA. In the end, the side branch access through a stent cell was computed based on the side branch surface and stent cell surface. This method was implemented using VTK toolkit with in-house developed modules and validated with a phantom dataset. The error of the algorithmic results for the 3D stent cell surface, 2D stent cell surface approximation, MCUSA and side branch access was 0.96 ± 0.64%, 0.98 ± 0.74%, 5.0 ± 5.2% and 8.9 ± 7.0%, respectively. The usability of this approach in clinical datasets was tested with 12 in-vivo IVOCT datasets from a one-year follow-up study. With the presented results, we concluded that the proposed method could be used to analyze the efficacy and performance of different stent designs to improve the outcome of PCI treatments.

In **Chapter 4,** stent covered side branches were detected for stent analysis. However, demands for uncovered side branch detection in the lesion region of a coronary artery have increased in the past decades, because the side branch location and size can suggest the optimal stent type, length, diameter, deployment position and operation plan before implanting a stent or during the diagnosis. This essential information can greatly impact the outcome of PCI treatment. Moreover, the side branch is also one of the most reliable landmarks used for image registration between baseline and follow-up datasets or multi-modality image fusion. Therefore, in **Chapter 5**, we presented a fully automated detection algorithm for both covered and uncovered side branches in IVOCT pullback runs. As side branches appear as cavities in the vessel tissue, they were detected by computing and analyzing the distance between the lumen center and the leading-edge of the intimal layer. To compute this distance, we need to remove all the bright components inside the lumen, fix the cavity caused by guide wire shadow and detect the lumen center. As a result, an image segmentation pipeline to segment the imaging catheter, protective sheath, guide wire and lumen was implemented. To validate the image segmentation pipeline and side branch detection method, 25 in-vivo IVOCT pullback runs from a two-year follow-up study were used. The image datasets were acquired with different pullback speed in different time periods and contain different types of stents or no stent at all. The intraclass correlation coefficient (ICC) of the imaging catheter radius, protective sheath radius and lumen contour position between the algorithmic results and ground truth was 0.997, 0.949 and 0.974, respectively. 100% of the guide wires were detected and the Dice's coefficient of the guide wire shadow region between the algorithmic results and ground truth was 0.97. In this chapter, only the side branches which are at least 0.8 mm in longitudinal direction and 8 degrees in the circumferential direction were included. The validation results show that 94.0% of 82 side branches were detected with less than 5.0% false positives. The Dice's coefficient of the angle region in circumferential direction between the ground truth and algorithmic results was 0.85. With the presented results, it is concluded that our image segmentation pipeline is accurate and robust enough for many advanced image processing algorithms that require the segmentations of these common components in IVOCT images. For example, it could be used to improve the robustness and accuracy of our strut detection methods. In **Chapter 2**, the metallic strut detection method should skip the bright imaging catheter because its high intensity value can influence the intensity profile analysis. In case there is bright air bubble noise in the protective sheath, it

should be skipped as well. In **Chapter 3**, the performance of the BVS strut detection method is influenced by the accuracy of lumen contours which indicate the ROIs. The automated side branch detection method offers a new option for accurate 3D side branch analysis in IVOCT pullback runs to optimize the CAD treatment or for image registration.

6.2 Future works

According to the validation results demonstrated in this thesis, we can conclude that our goals in each chapter have been achieved to a certain degree. However, there is still plenty of room for further improvement of this work.

6.2.1 3D stent model

In **Chapter 2** and **3**, the stent strut detection relies on only 2D information in individual frames. Actually, a stent is usually formed by repeated structures called stent cells and can be presented as a 3D model. This pattern should globally match the stent strut distribution. The complexity, when using the stent model, is that different stents have different models and a stent structure could be distorted during the expansion because the hardness of tissue and plaques is different. Due to these reasons, stent pattern model is not used in this thesis. In future, stent pattern model could be used to supervise the stent strut detection. It can be fitted to the detected stent struts, and help to remove the false positives that locate in the wrong position or retrieve the false negative struts by checking the trend of each stent wire. For a new type of stent without existing model, a model could be manually defined based on the detected struts and later used to supervise future strut detection for the same type of stents. The stent pattern model can also help the 3D stent cell contour reconstruction in **Chapter 4** and improve the efficiency of the 3D stent cell analysis. Furthermore, the spiral information of the stent wire could be used to reconstruct the whole implanted stent skeleton automatically for visualization and further measurement.

6.2.2 IVOCT image improvements

Ideally, in IVOCT images, different tissue should be represented by different intensity values so that segmentations can be easily applied. However, we noticed that homogeneous tissue also has very different gray-scale in the same pullback run or even in the same frame. The main reasons for the non-uniform gray-scale include the distance between the imaging catheter and scanned sample, tissue coverage of the sample or the angle of incidence. Once an image correction model is set up, the intensity of IVOCT images can be unified and the segmentation and detection performance in **Chapter 2, 3** and **5** should be greatly improved. Better strut detection results also positively influence the stent cell analysis in **Chapter 4**.

Relative low longitudinal resolution of frequency-domain IVOCT images could hamper the quantitative analysis in IVOCT images. Both time-domain IVOCT and new super-high speed OCT catheter can increase the longitudinal resolution by reducing the slice distance which makes small side branch detection and side branch lumen smoothness possible in **Chapter 5**. Furthermore, the strut detection methods in **Chapter 2** and **3** also can benefit from the additional slices, because smaller slice distance suggests that when analyzing one frame, its neighboring frames could be

used as reliable references. All above can consequently help to generate more accurate stent surface and stent cell contours in **Chapter 4**.

6.2.3 Image registration

Despite IVOCT is one of the best image modality for intuitive visualization of fine coronary vascular structures as well as accurate and reproducible quantifications, every single modality has its drawbacks and is insufficient to provide all necessary information. The modern approach requires the combination of multiple imaging modalities to be able to assess the CAD situation. The main shortcoming of IVOCT is its limited penetration which cannot delineate deep structures such as plaques with thick coverage or side branch lumen wall. Eccentrically located imaging catheter in a big lumen could also cause image blurring or even missing in the region far away from the catheter. Besides, the longitudinal image acquired by IVOCT system does not contain the sensor travelling trajectory so that could not outline the original tortuosity of the artery. Multi-modality image registration could be a solution for this challenge. Compare with IVOCT, IVUS has lower resolution but much deeper penetration. If both IVUS and IVOCT images are acquired for the same vessel, these images can be co-registered based on the side branches detected in **Chapter 5**, and the IVUS image could provide the deep region information of the vessel. Moreover, the detected side branches can assist the registration between IVOCT and coronary angiography, CT or other image modalities, which will help us to reconstruct the real 3D tortuosity of vessels for IVOCT images. Image registration can lead to a comprehensive and objective understanding of coronary disease and guide the intervention effectively, especially for patients with complex lesions.

CHAPTER

7

Samenvatting en Conclusies

7.1 Samenvatting en conclusies

Sinds tientallen jaren zijn aandoeningen aan het hart de nummer één doodsoorzaak wereldwijd ondanks de enorme vooruitgang van de moderne medische kennis op het gebied van diagnose en behandeling. De vorming van atherosclerose in de coronair vaten is een belangrijke aandoening bij hartziekten dat een vernauwing van het vat veroorzaakt wat weer de bloedtoevoer van zuurstofrijk bloed naar de hartspier verminderd. De behandeling van hartzieken bestaat uit; verandering in leefstijl, medicijnen en medische ingrepen. De uitvinding van de ballon angioplasty (PCI) in 1977 door Andreas Gruntizig was een grote revolutie in de kransslagader interventies in de vorm van een nieuwe methode bij de behandeling van hartziekten. De PCI technieken zijn de afgelopen jaren verder geëvalueerd en zijn bewezen een kosteneffectieve behandelmethode vergeleken met het plaatsen van een bypass en wordt beschouwd als eerste optie bij het behandelen van ziekten in de kransslagader. Tegenwoordig is het plaatsen van een stent de beste verbetering van de ingreep. Een stent is een klein medisch object dat ondersteuning geeft aan de vaatwand na het oprekken van het vat door een ballon om te voorkomen dat het vat zich weer sluit. De eerste stents waren metalen stents en later werd de drug verspreidende stents geïntroduceerd om het risico van instent restenosis zoals bij de kale metalen stents te verminderen. Zowel de metalen stent als de medicijn verspreidende stent zijn permanent waardoor een vat met een stent eigenlijk ingekooid is door metaal en het normale vasculaire remodeling proces verder niet kan doorgaan. Daarom zijn oplosbare scaffold ontwikkeld als een tijdelijk device die de vaatwand ondersteund direct na het inbrengen en daarna langzaam wordt afgebroken.

De constante vraag voor de optimale diagnose en behandeling technieken van hartziekten stimuleert de ontwikkeling van medische beeldverwerkingstechnieken. Voor de introductie van intravasculaire optical coherence tomography (IVOCT), werden reeds veel ander beeldmodaliteiten, inclusief niet-invasieve technieken zoals computed tomography (CT) en invasieve technieken zoals coronaire angiografie en intravasculaire ultrasound (IVUS) gebruikt voor onderzoek en klinische routine bij de behandeling van vaatziekten. Echter geen van deze technieken bezit een resolutie die hoog genoeg is om de kleine structuren zoals dunne fibreuze afdekkingen van kwetsbare plaque of de dunne laag cellen die de stent struts bedekken zichtbaar te maken. IVOCT is een nieuwe beeldvormende techniek gebaseerd op nabije infrarood licht dat in staat is om driedimensionale (3D) opnames in-vivo van bloedvaten te maken met een resolutie van ongeveer 10 micrometer. De nieuwe frequentie domein IVOCT systemen hebben een sterk verbeterde acquisitie snelheid en signaal – ruis verhouding. De niet geëvenaarde resolutie maakt het op dit moment de enige beeld modaliteit voor de nauwkeurige analyse van de stent. Het doel van dit proefschrift is daarom om efficiënte en nauwkeurige beeldverwerkingsalgoritmes te ontwikkelen voor de stent analyse en stent plaatsing optimalisatie in IVOCT beelden.

Stent analyse, bijvoorbeeld de strut distributie, aantal struts, strut positie en de hoeken tussen de struts is erg belangrijk aangezien het helpt bij de voortdurende verbetering van de stent fabricage om; een beter ondersteuning van de vaatwand te verkrijgen, meer flexibiliteit te geven voor het inbrengen van de stent en een betere dosering van de drugs voor de drug verspreidende stents. Verder wordt stent analyse ook steeds meer gebruikt voor het verbeteren van PCI door een betere inschatting van de benodigde stent lengte en diameter. Te kleine stents of stents die niet voldoende zijn uitgezet, kunnen resulteren in stent malappositie, terwijl verkeerde stent plaatsing

tot een onvolledige bedekking van een vernauwing kan leiden. Het risico is onder meer late neointima hyperplasia en late stent malappositie. Een nauwkeurige stent strut detectie methode in IVOCT kan daarom significant het risico op een vervolg procedure verminderen.

Gegeven het groot aantal zichtbare struts in een pullback run van een volledige stent is een kwantitatieve analyse alleen maar mogelijk wanneer de strut detectie automatisch wordt uitgevoerd. **Hoofdstuk 2** presenteert daarom een nieuwe methode om metalen stent struts automatisch te detecteren in IVOCT pullback runs. Omdat metalen stent struts te zien zijn als heldere punten met daarachter een lange donkere schaduw, analyseert het voorgestelde algoritme de intensiteitsverdeling van elke scan lijn om kandidaat pixels te vinden die mogelijke bij een strut horen. Vervolgens worden de schaduw randen opgezocht en op een innovatieve manier gebruikt als kenmerk om foute kandidaat pixels te verwijderen en de resterende pixels te groeperen in kandidaat struts. In het geval dat struts bedekt zijn met een dikke laag weefsel waardoor de kandidaat pixel detectie faalt, kunnen deze struts alsnog gevonden worden op basis van hun schaduw randen. Als laatste worden de voerdraden weg gefilterd en de centra van de strut punten berekend. Bij de validatie met 18001 struts in 10 in-vivo pullbacks van wisselende beeldkwaliteit (goed, matig en slecht) werden 91% van de malapposed struts, 93% van de apposed struts en 94% van de bedekte struts gevonden met slecht 4% foute positieven. De validatie resultaten laten zien dat de voorgestelde methode kan worden gebruikt voor de kwantitatieve stent analyse.

In tegenstelling tot metalen stens zijn biologisch oplosbare stents (BVS) gemaakt van diverse polymeren en zien er anders uit in IVOCT beelden. Om een nauwkeurige BVS strut analyse uit te voeren is IVOCT op dit moment de beste afbeeldingstechniek vanwege de hoge resolutie en de doorzichtigheid van de polymere BVS struts. De interne samenstelling van een BVS strut is homogeen waardoor het licht erdoor heen kan gaan en het teruggekaatste signaal veroorzaakt wordt door het verschil in brekingsindex tussen de strut en zijn omgeving zoals spoelvloeistof en weefsel. Daarom zien BVS struts eruit als heldere rechthoekjes met een donkere kern. Vergelijkbaar met de metalen stent analyse, kan BVS strut detectie worden gebruikt voor stent analyse. Om het oplosproces van BVS struts te volgen, is de strut oppervlakte ook interessant. **Hoofdstuk 3** beschrijft daarom een automatische BVS stent strut detectie methode in IVOCT pullback runs om de donkere kernen van BVS struts te vinden. Om het zoekgebied voor de struts detectie aan te geven, wordt voor de post interventie en de follow-up data sets verschillend omgegaan met de lumen contour aangezien de strut locaties verschillend zijn. De methode maakt gebruik van kleine lijnstukjes die bij een donkere kern behoren en deze worden vervolgens gegroepeerd om een egale donkere kern te vormen. Bij de validatie met 6 in-vivo pullback runs met 3 baseline en 3 follow-up data sets detecteerde dit algoritme 90.4% van de 2183 baseline BVS struts en 96.6% van de 2508 follow-up BVS struts met 3.0% en 0.8% foute positieven respectievelijk. De oppervlakte van de BVS strut werd bepaald aan de hand van de donkere kern en de prestatie werd gevalideerd door gebruik te maken van de Dice index. Voor de baseline dataset, de Dice index tussen de gouden standaard en de resultaten van het algoritme was 0.83, voor follow-up datasets, was deze Dice index 0.85. De validatie studie laat zien dat de nieuwe methode nauwkeurig BVS struts kan detecteren en de kern oppervlaktes kan meten. Dit kan behulpzaam zijn voor 3D reconstructie, bepalen van de hoeveelheid weefsel op de struts, malappositie analyse, de strut verdeling, en het volgen van het oplos proces.

Chapter

7

Naast de ontwikkeling van nieuw stent types, heeft de invloed van het stent ontwerp op het effect van de behandeling veel meer aandacht gekregen. De bestaande stent analyse is voornamelijk gericht op tweedimensionale informatie zoals; aantal struts en de verdeling of de hoek tussen de struts in een enkel beeld. Echter is het aangetoond dat de stent cel structuur invloed heeft op het vermogen om te ondersteunen, vermogen om uit te zetten, flexibiliteit, aanligeigenschappen, dosisdistributie en de toegang tot de zijtakken. Aangezien een stent een 3D structuur is, moet een stent cel ook in de 3D ruimte worden geanalyseerd. Zowel de volledige stent cel grootte als de maximale circulaire niet-ondersteunde wand oppervlakte (MCUSA) worden gebruikt om de invloed van een stent op te vaatwand te evalueren. **Hoofdstuk 4** beschrijft een halfautomatische methode om de stent cel grootte (MCUSA) en de toegang tot de zijtak door de stent cel te meten. Eerst wordt de 3D stent wand en de stent cel contour gereconstrueerd aan de hand van de gedetecteerde struts en gebruikt voor de stent cel oppervlakte segmentatie en de metingen. Een 2D benadering van de stent cel oppervlakte wordt gebruikt om de MCUSA te bepalen en te meten. Als laatste werd de zijtaktoegankelijkheid door een stent cel bepaald op basis van de zijtakoppervlakte en de stent cel oppervlakte. Deze methode is geïmplementeerd met behulp van de VTK toolkit met zelf ontwikkelde modules en gevalideerd met een fantoom data set. De fout in het algoritme uitkomsten voor de 3D stent cel oppervlakte, 2D stent cel oppervlakte benadering, MCUSA en de zijtaktoegankelijkheid was $0.96 \pm 0.64\%$, $0.98 \pm 0.74\%$, $5.0 \pm 5.2\%$ en $8.9 \pm 7.0\%$, respectievelijk. De bruikbaarheid van deze benadering is getest in klinische datasets van 12 in-vivo IVOCT datasets uit een één jaar follow-up studie. Aan de hand van de gepresenteerde resultaten konden we concluderen dat de voorgestelde methode gebruikt kan worden om het effect van verschillende stent ontwerpen te analyseren om de uitkomst van katheterisatie procedures te verbeteren.

In **hoofdstuk 4** werden de zijtakken die met struts zijn bedekt gedetecteerd. Echter de interesse voor het detecteren van niet bedekte zijtakken neemt de laatste jaren toe omdat de positie en grootte van de zijtakken gebruikt kunnen worden voor de selectie van de optimale stent type, lengte, diameter, positie van de stent en het plan van aanpak voor dat een stent geplaatst wordt of tijdens de diagnose. Deze essentiële informatie heeft grote invloed op de uitkomst van een katheterisatie behandeling. Verder zijn zijtakken ook één van de meest betrouwbare anatomische markeerpunten die gebruikt kunnen worden voor beeld registratie tussen baseline en follow-up studies of voor multimodale beeldfusie. Daarom beschrijft **hoofdstuk 5** een volledig automatisch algoritme voor het detecteren van bedekte en niet bedekte zijtakken in IVOCT pullback datasets. Aangezien zijtakken er uit zien als gaten in de vaatwand, worden zij gedetecteerd door de afstand tussen het lumen centrum en de startpunten van de intima laag te berekenen en te analyseren. Om deze afstand te kunnen berekenen, moesten alle heldere onderdelen in het lumen worden verwijderd en de gaten die worden verzaakt door de voerdraad schaduw hersteld worden en het detecteren van de het lumen centrum. Om dit te bereiken werd een beeld segmentatie pijplijn geïmplementeerd voor het segmenteren van de beeldkatheter, beschermende hoes, voerdraad en het lumen. Om deze beeld segmentatie pijplijn te valideren zijn 25 in-vivo IVOCT pullback runs gebruikt. De datasets waren opgenomen met verschillende terugtreksnelheden op verschillende tijdstippen en bevatten verschillende types stents of geen stent. De interclass correlatie coëfficiënt (ICC) van de straal van de beeldkatheter, de straal van de beschermende hoes, en de positie van het lumen contour tussen de uitkomsten van de algoritmes en de gouden standaard

was 0.997, 0.949 en 0.974 respectievelijk. 100% van de voerdraden waren gedetecteerd en de Dice index van de voerdraad schaduw gebied bepaald door het algoritme en de gouden standaard was 0.97. In dit hoofdstuk waren alleen zijtakken met een lengte van minimaal 0.8 mm in de lengterichting en 8 graden in de omtrek meegenomen. De validatie gaf aan dat 94.0% van de 82 zijtakken werden gevonden met minder dan 5.0% foute positieven. De Dice coëfficiënt van de hoek gebieden in de omtrek richting tussen de resultaten van het algoritme en de gouden standaard was 0.85. Gegeven de gepresenteerde resultaten is geconcludeerd dat de beeldverwerkingspijplijn nauwkeurig en robuust genoeg is voor de vele geavanceerde beeldverwerkingsalgoritmes die de segmentatie van de algemene structuren in de IVOCT beelden vereisen als voorbewerking. Bijvoorbeeld zou het de robuustheid en nauwkeurigheid van de stent strut detectie methode kunnen verbeteren. De metalen stent strut detectie methode uit **hoofdstuk 2** zou de heldere beeldkatheter moeten overslaan omdat de hoge intensiteit het intensiteitsprofiel analyse kan verstoren. In het geval dat er luchtbelletjes in the beschermende hoes zitten moeten deze ook overgeslagen worden. De prestatie van de BVS detectie in **hoofdstuk 3** wordt beïnvloed door de nauwkeurigheid van de lumen contour detectie die de ROI bepaald. Deze automatische zijtakdetectie biedt een nieuw mogelijkheid voor nauwkeurige 3D zijtakanalyse in IVOCT pullback runs om de hartziekte behandeling te optimaliseren of voor beeld registratie.

7.2 Toekomstig werk

Zoals de validatie resultaten in dit proefschrift laten zien, kunnen we concluderen dat de doelstellingen in elk hoofdstuk zijn bereikt tot een zekere hoogte. Echter is er nog veel ruimte voor verbetering.

7.2.1 3D stent model

In **hoofdstuk 2 en 3** maakt de strut detectie methode alleen gebruik van 2D informatie in afzonderlijke beelden. Eigenlijk bestaat een stent uit repeterende patronen; de zogenaamde stent cellen en kunnen als een 3D model worden gepresenteerd. Dit patroon zou globaal terug moeten komen in de stent strut distributie. De beperkende factor bij het gebruik van een stent model is het feit dat er verschillende stent modellen zijn en de structuur van de stent verstoord kan zijn tijdens het opblazen door de stijfheid van de plaque en het verschil in plaque. Daarom zijn er in dit proefschrift geen stent patroon modellen gebruikt. In de toekomst zouden deze stent patroon modellen kunnen worden gebruikt om de strut detectie te sturen. Het kan gefit worden aan de gedetecteerde stent struts om verkeerd gedetecteerde struts te verwijderen door de trend bij elke stent draad te controleren. Voor nieuwe type stents zonder een bestaand model, kan het model handmatig gedefinieerd worden op basis van de gedetecteerde struts en later kan dit model weer gebruikt worden om de strut detectie van dezelfde type stent te sturen. Dit stent patroon model kan ook helpen bij de 3D stent cel contour reconstructie in **Hoofdstuk 4** om de efficiency van de 3D stent cel analyse te verhogen. Verder kan de spiraal informatie van de stent draad worden gebruikt om de gehele geïmplanteerde stent skelet automatisch te reconstrueren voor visualisatie en verder metingen.

7.2.2 IVOCT beeldverbetering

Onder ideale omstandigheden zouden de verschillende weefsel types door verschillende intensiteiten worden weergegeven zodat segmentatie eenvoudig is. Echter hebben we waargenomen dat homogeen weefsel reeds ook verschillende grijswaardes heeft binnen dezelfde pullback dataset en zelf binnen het zelfde frame. De algemene reden voor deze non-uniforme grijswaarde verdeling binnen een beeld is het verschil in afstand tussen de beeldkatheter en het stukje weefsel, weefsel bedekking van het stukje of de hoek van inval van het licht. Als eenmaal een correctie model is ontwikkeld, kan de intensiteit binnen IVOCT beelden meer uniform worden gemaakt waardoor de segmentatie en de detectie uitkomsten in **hoofdstukken 2, 3 en 5** sterk verbeterd zullen worden. Een betere strut detectie zal ook tot een betere stent cel analyse in **hoofdstuk 4** leiden.

De relatieve laag resolutie in de lengterichting van frequentie domein IVOCT beelden heeft invloed op de kwantitatieve analyse van de IVOCT beelden. Zowel tijddomein IVOCT en nieuw zeer hoge snelheid OCT katheters kunnen de resolutie in de lengte richting verbeteren door de afstand tussen de individuele beelden te verminderen wat de detectie van kleine zijtakken mogelijk maakt en de zijtak lumen ruwheid verminderd zoals in **hoofdstuk 5**. Verder zullen de strut detectie methoden in **hoofdstuk 2 en 3** ook voordeel hebben van extra beelden aangezien een kleinere afstand inhoud dat informatie uit aanliggende frames kan worden gebruikt als betrouwbare referentie. Alles hierboven kan daarom helpen bij het genereren van betrouwbaarder stent oppervlakten en stent cel contouren in **hoofdstuk 4**.

7.2.3 Beeldregistratie

Ondanks het feit dat IVOCT de beste beeldmodaliteit is voor zowel een intuïtieve visualisatie van kleine coronaire vaatstructuren als voor een nauwkeurige en reproduceerbare kwantificatie, heeft elke modaliteit ook zijn nadelen en kan het niet alle benodigde informatie verschaffen. De moderne benadering vereist de combinatie van meerdere beeldmodaliteiten om de toestand van het hart goed te kunnen beoordelen. De grootste tekortkoming van IVOCT is de beperkte indringingsdiepte waardoor dieper gelegen structuren zoals plaques met een dikke bedekking of de lumen wand van een zijtak niet te zien zijn. Een sterk uit het midden gelegen beeldkatheter in een groot vat kan ook beeld vertroebeling veroorzaken of dat zelfs stukken beeld missen ver weg van de katheter. Verder bevat het longitudinale beeld zoals dat word opgenomen met IVOCT geen informatie over het traject dat de sensor aflegt en kan daarom niet de oorspronkelijke kronkeling van het vat weergeven. Het registreren van meerder beeldmodaliteiten kan een oplossing zijn voor deze uitdaging. Vergeleken met IVOCT heeft IVUS een lagere resolutie, maar een veel hogere diepte doordringing. Als zowel IVUS als IVOCT worden opgenomen van hetzelfde vat, dan kunnen deze beelden worden geregistreerd op basis van de zijtakken zoals gedetecteerd in **hoofdstuk 5** en de IVUS kan dan de informatie verschaffen over de diepere structuren in het vat. Verder kunnen de gedetecteerde zijtakken helpen bij het registreren tussen IVOCT en een coronair angiogram, CT of een andere modaliteit, die kan helpen om de echte 3D structuur van een vat te reconstrueren van de IVOCT beelden. Beeldregistratie kan leiden tot een inzichtelijke en objectieve beoordeling van aandoeningen aan de kransslagaderen en de ingrepen op een effectieve manier te ondersteunen, speciaal bij patiënten met complexe vernauwingen.

List of abbreviations

BMS	bare-metal stents
BVS	bioresorbable vascular scaffold
CABG	coronary artery bypass graft
CAD	coronary artery disease
CHD	coronary heart disease
CT	computer tomography
DES	drug-eluting stents
FP	false positive
GT	ground truth
GW	guide wire
HDL	high-density lipoprotein
ICC	intraclass correlation coefficient
IVOCT	intravascular optical coherence tomography
IVUS	intravascular ultrasound
LDL	low-density lipoprotein
MCUSA	maximum circular unsupported surface area
MRI	magnetic resonance imaging
OCT	optical coherence tomography
PCI	percutaneous coronary interventions
PS	protective sheath
ROI	region of interest
SB	side branch
TP	true positive

Publication list

Journal papers

A. Wang, J. Eggermont, N. Dekker, H. M. Garcia-Garcia, R. Pawar, J. H. Reiber, and J. Dijkstra, "Automatic stent strut detection in intravascular optical coherence tomographic pullback runs," Int J Cardiovasc Imaging **29**, 29-38 , 2013.

A. Wang, J. Eggermont, N. Dekker, P. J. de Koning, J. H. Reiber, and J. Dijkstra, "3D assessment of stent cell size and side branch access in intravascular optical coherence tomographic pullback runs," Comput Med Imaging Graph **38**, 113-122, 2014.

A. Wang, J. Eggermont, J. H. C. Reiber, and J. Dijkstra, "Fully automated side branch detection in intravascular optical coherence tomography pullback runs," Biomed Opt Express **5**, 3160-3173, 2014.

A. Wang, S. Nakatani, J. Eggermont, Y. Onuma, H. M. Garcia-Garcia, P. W. Serruys, J. H. C. Reiber, and J. Dijkstra, "Automatic detection of bioresorbable vascular scaffold struts in intravascular optical coherence tomography pullback runs," Biomed Opt Express **5**, 3589-3602, 2014.

Conference papers

A. Wang, J. Eggermont, N. Dekker, H. M. Garcia-Garcia, R. Pawar, J. H. C. Reiber, and J. Dijkstra, "A robust automated method to detect stent struts in 3D intravascular optical coherence tomographic image sequences," in *Medical Imaging*, 2012.

A. Wang, J. Eggermont, J. H. C. Reiber, N. Dekker, P. J. H. de Koning, and J. Dijkstra, "Assessment of implanted stent coverage of side-branches in intravascular optical coherence tomographic images," in *Medical Imaging,* 2013.

A. Wang, J. Eggermont, N. Dekker, J. H. Reiber, and J. Dijkstra, "Semi-automatic measurement of vessel wall support from implanted stents in IVOCT image sequences," in *MICCAI 2013 STENT,* 2013.

Abstracts

A. Wang, , J. Eggermont, N. Dekker, H. M. Garcia-Garcia, R. Pawar, J. H. C. Reiber, and J. Dijkstra. "An automatic method for stent strut detection in IVOCT images," *Proc. Optics in Cardiology*, Rotterdam, 2013.

A. Wang, J. Eggermont, J. H. C. Reiber, N. Dekker, P. J. H. de Koning, and J. Dijkstra. "Semi-automatic assessment of side-branch coverage from stents in IVOCT images," *Proc. Optics in Cardiology,* Rotterdam, 2013.

A. Wang, J. Eggermont, N. Dekker, J. H. Reiber, and J. Dijkstra. "Semi-automatic assessment of the stent cell size in IVOCT images," *Proc. Optics in Cardiology,* Rotterdam, 2013.

Acknowledgments

In the end of this thesis, I cannot help looking back on the days at the Division of Imaging Processing (LKEB), Department of Radiology, Leiden University Medical Center in the past five years. I would not be where I am today without the guidance, instruction, encouragement and other help from many people, so I want to take this opportunity to acknowledge my great debt to them.

To begin with, I would like to express my deepest appreciation to my promoters: Prof.dr.ir. Johan H.C. Reiber and Prof.dr.ir. Boudewijn P.F. Lelieveldt. Dear Hans, thank you for giving me the opportunity to pursue my Ph.D study in such an exciting field with truly outstanding researchers. I have always been inspired by your remarkable passion, dedication, wisdom and energy. Dear Boudewijn, you devoted considerable precious time and effort to helping me successfully complete the last and most difficult mile of my five years study. You also taught me how to be purposeful and active and led me through the fog to the goal.

I am especially grateful to Jouke, my co-promoter, for his immeasurable amount of support and daily guidance throughout this study. Your insights into and patient endurance throughout my project have been a true blessing. I owe you many, many thanks for all the help.

My sincere gratitude should also be given to my other colleagues in LKEB for their enthusiastic guidance, encouragement and very learned critiques of my research work. I am greatly thankful to Dr. Jeroen Eggermont for offering me valuable suggestions and sharing his Ph.D study experience with me during my study. I enjoyed working with you a lot. My grateful thanks are also extended to Mr. Niels Dekker for his persistent and selfless help in C++ programming and paper writing, to Ir. Patrick de Koning for helping me reconstruct the stent surface using VTK toolkit and to Ir. Pieter Kitslaar, Dr.ir. Alexander Broersen and Dr.ir. Jasper Janssen for their tremendous guidance on MeVisLab and all those very productive discussions. Furthermore, thank you for sharing the sweet smiles on the faces of your little angels at our office. I also benefited a lot from the regular meetings with Dr. Qian Tao and Dr. Oleh Dzyubachyk, who inspired me a lot in the research. I appreciate your valuable time and contribution. I cannot forget those short talking with Dr.ir. Martijn van de Giessen, Ir. Michèle Huijberts, Mr. Mohammed S. ElBaz and Mr. Leo Wolf after 6 PM. I must extend my appreciations to the other members of LKEB. No listing all the names here does not mean that I would forget what you have done for me. I feel so blessed to be able to pursue my dream with you all.

During my PhD study, I worked closely together with the brilliant researchers from Cardialysis BV and Erasmus Medical Center in Rotterdam. Dr. Hector M. Garcia-Garcia, Dr. Yoshinobu Onuma, Dr. Shimpei Nakatani and Prof. Patrick W. Serruys shared their clinical knowledge and provided most of the intravascular optical coherence tomography data sets and the ground truth for the validations of my research. Their contribution is essential to this thesis. Our cooperation turned out to be a great success.

Moreover, I would like to express my deepest gratitude to my family. I am truly grateful that I am surrounded by the love from my parents throughout my study. All the support they have offered me over the years was the greatest gift anyone has ever given me. Thank you, Mom and Dad, for raising me, encouraging me when I face challenges and teaching me the value of hard work. The expectation and love from you are the strongest motivation of my continuous work and the constant source of confidence. 亲爱的爸爸妈妈，谢谢你们养育了我。在我十多年求学路上，你们热情的鼓励、殷切的期盼和无私的爱，是我持续前进的最大动力，更是我永不言弃的信心来源。Meanwhile, I need to thank my dear uncle, Dr. Aimin Liu, who set a shining example to me during my long way of education. My sincere thanks are also extended to my other relatives, for their years love and support. 感谢尊敬的刘爱民叔叔及其一家，一直以来对我的关心和帮助。您一直都是我的学习榜样和楷模。也要感谢各位亲人和朋友对我学业的支持，在我留学的日子里，代我照顾我的父母，令我永志不忘。Especially, I need to thank Jinghua. I am so lucky to meet you in the Netherlands. The time we spent together and the shared joys and sorrows were the most valuable part in my life.

I also would like to express my delight to have so many fantastic friends during the study period in the Netherlands. The friendship has been linking us so tightly no matter where we are and will be. In the end but not the least, I would like to offer my appreciation to the China Scholarship Council and the Education Minster of China for financially supporting me to pursue my PhD study in the Netherlands.

Curriculum vitae

Ancong Wang was born in Dongying, Shandong, China in 1982. In 2001, he started his bachelor study on Computer Science and Technology at Shandong University, Jinan, China. He received the bachelor degree in July 2005. In the same year, he was offered a position in one of his teachers' company, Dareway Software Company, working as a software engineer. One year later, he enrolled in the Department of Information Engineering at Northwest A&F University, Xi'an, China, as a master student, under the supervision of Prof. Dongjian He. His master project is "Study on Key Techniques for Volleyball Tracking and Trajectory Analysis". In July 2009, he graduated with honors (Cum Laude). In September 2009, he joined the Vascular and Molecular Imaging Group at the Division of Image Processing (LKEB), Department of Radiology, Leiden University Medical Center, Leiden, the Netherlands, to pursue the PhD degree. His promoters and co-promoter are Prof. dr. ir. Johan H.C. Reiber, Prof. dr. ir. Boudewijn P.F. Lelieveldt and Dr. ir. Jouke Dijkstra. He has been working on the automatic quantification in intravascular optical coherence tomography (IVOCT), including strut detection, stent analysis and side branch analysis. The works are presented in this thesis and most of the algorithms have been integrated into both scientific research and commercial software packages that were validated and used in a number of medical research centers around the world.